Università di Roma *"Sapienza"*

DOTTORATO DI RICERCA IN

MATEMATICA

XXVII CICLO

2D-Vorticity genesis and dynamics studied through particle methods.

Emanuele Rossi

Docente Guida:
Dr. Andrea Colagrossi

Tutor:
Prof. Mario Pulvirenti

15 Dicembre 2014

ABSTRACT

Vortex Methods are a class of particle approximation of the Euler and the Navier-Stokes equation written in vorticity formalism. Their main advantages are the discretization of only the rotational part of the fluid, the use of an integral representation of the velocity field to exactly enforce the boundary condition at infinity. The use of a Lagrangian formulation also makes these methods not influenced by the discretization used.

The weak point of Lagrangian Vortex Methods is the excessive clustering or rarefaction of the vortex particles during their evolution, caused by Lagrangian distortion. To compensate this problem several methods have been introduced in order to redistribute particles over a regular distribution of points.

This work presents a new vortex method called Diffused Vortex Hydrodynamic (DVH). The DVH is a two dimensional particle vortex method in which is not necessary the use of any remeshing method tanks to the introduction of "Regular Point Distribution" (RPD) in the diffusion process. The velocity of the vortex particles is evaluated using a Fast Multipole Method.

The DVH can be applied to perform high Reynolds simulations of flows around bodies with arbitrary shapes thanks to the use of RPDs and to the introduction of a so called visibility mask to perform diffusion in presence of bodies with edges such as squared cylinders or airfoils.

A RPD is a set of equispaced points without any topological connection. During the diffusion process each vortex gives its diffusive contribution to RPDs nodes using the fundamental solution of the heat equation, after the diffusion of all vortices a new set of regularly spaced particles is generated at the RPDs nodes location, substituting the former one. This procedure avoids the formation of holes and accumulations in the vorticity distribution without the use of any remeshing method.

In the region close to solid bodies RPDs are generated using the packing algorithm described in Colagrossi et al. (2012), this algorithm adapt the distribution of points to the body contour allowing to treat flows around bodies with complex geometry. Far from the solid surfaces simple Cartesian lattices, with different size according to the distance from the body, can be used with the same function of RPDs. In the DVH model, all the different RPDs can overlap each other and can be characterized by different spatial resolutions. In this way it is possible to reduce the number of vortices generated during the evolution while maintaining high resolution where necessary.

The DVH method is tested on a series of different problems ranging from the evolution of vorticity distribution in free space to flows in presence of bluff bodies with different shapes.

The evolution of vorticity distribution in free space is simulated to better control the errors made in the diffusive and in the advective step respectively. Two classical problems are considered: the Lamb-Oseen problem and the merger of a pair of co-rotating vortices. The results are compared with that obtained with a SPH solver.

A large series of flows around bluff bodies is simulated, ranging from circular and elliptical cylinders to body with edges such as airfoils. The results obtained will be compared with the ones present in the literature.

An example of the ability of DVH to perform high Reynolds simulations is given by the simulations of he flow past an impulsively started cylinder up to $Re = 50000$ and $Re = 100000$. These last results are, to our knowledge, the cylinder wakes with the highest Reynolds number simulated without using any turbulence models.

As an example of the use of the packing algorithm to generate RPDs around bodies with complex geometry, the flow around a smooth body with a cavity is also simulated for various angles of attack, in such a way to study the effect of the cavity on the lift and drag coefficient of the body and on the wake formation.

The DVH is suitable to simulate fluid flows around non-smooth bodies. In this case flow around squares, rectangles and airfoils with various angles of attack is simulated and the results are compared with those found in literature.

RINGRAZIAMENTI

Ringrazio Andrea Colagrossi per avermi insegnato tutto ciò che adesso conosco di programmazione e per la pazienza dimostratami in questi due intensi anni di lavoro, nei quali di sicuro la frase più ricorrente è stata “Rossi te voglio ammazza!!!” senza nulla togliere a “Rossi quanto me fai penà!”.

Ringrazio Benjamin Bouscasse per il prezioso aiuto nei più difficili di questo lavoro e per il suo imparagonabile lavoro di motivational coach: “Rossi non sento battere i tasti... clak clak clak!!!”.

Ringrazio Mario Pulvirenti per essere stato la mia guida ed avermi indirizzato e sostenuto con preziosi consigli e insegnamenti nel percorso intrapreso, dagli ultimi anni della laurea specialistica fino alla conclusione di un interessante dottorato.

Ringrazio Giorgio Graziani per il prezioso lavoro svolto e da cui sono partito per lo studio e lo sviluppo di tutto il progetto di dottorato.

Ringrazio Emilio Fortunato Campana, direttore del CNR-INSEAN, per aver reso possibile la mia permanenza presso il CNR-INSEAN e aver potuto conoscere ed imparare da esperti ricercatori.

Ringrazio i ricercatori INSEAN per il loro sostegno e supporto e per aver condiviso tanti bei momenti negli ultimi due anni. Un ringraziamento particolare va a Matteo, Salvatore, Danilo, Giuseppina e Marilena.

Ringrazio la mia famiglia per la pazienza e il supporto incondizionato nei momenti difficili di tutti questi anni.

Ringrazio Valentina per tutto il supporto, la pazienza e l’affetto che mi ha donato in questi ultimi mesi e per tutte le sere passate davanti ad una birra ad ascoltarmi parlare del mio lavoro.

CONTENTS

1 INTRODUCTION

1.1 MOTIVATIONS AND BACKGROUNDS

Particle models is a generic term for the class of simulation models based on a discrete representation of a physical system involving the use of interacting particles. Each particle carries its own physical attributes such as position, mass, charge, velocity and/or vorticity. The state of the physical system is defined by the attributes of a finite ensemble of particles and the evolution of the whole system is determined by the laws of interactions of the particles. These methods can be applied to a wide range of physical problems, from astrophysics to naval engineering, from the physics of plasma to chemistry.

One of the major fields of application of the particle models is the study of hydrodynamical problems. The Lagrangian form of the Navier-Stokes equation allows the use of particle methods, replacing differential operators with integral one discretized over the particle locations.

Over the years two particle methods have become popular to simulate fluid flows: the Vortex Methods (VMs) and the Smoothed Particle Hydrodynamics (SPH).

The Smoothed Particle Hydrodynamics is a particle method that has been introduced by Lucy (1977) to simulate astronomical problems and then developed by Monaghan (see *e.g* Monaghan (1992)) whom first applied it to fluid mechanics to simulate free-surface inviscid flows (Monaghan (1994)).

The basic idea of the method is to discretize the whole fluid domain into (smooth) particles where each particle is associated to a symmetric, regular, non-negative function that emulate its mass distribution. This method simulates the motion of the considered fluid and can solve problems related to free surfaces or multi-phase flows, such as breaking and fragmentation phenomena.

VM is a particle approximation of the Euler and the Navier-Stokes equation written in vorticity formalism. First used by Rosenhead (1931) in his study of vortex sheet motion in a constant density inviscid fluid, was then developed by researchers such as Chorin (1978), Leonard (1980), Liu and Doorly (2000), Mas-Gallic (1987), Shankar and Dommelen (1996).

The main advantages of VM are:

- discretizing only the rotational part of the fluid, reserving computational resources where $\omega \neq 0$;

- using an integral representation of the velocity field to exactly enforce the boundary condition at infinity;
- using a Lagrangian formulation, the method is not influenced by the discretization used.

The weak point of Lagrangian Vortex Methods is the excessive clustering or rarefaction of the vortex particles during their evolution, caused by Lagrangian distortion. To compensate this problem several methods have been introduced in order to redistribute particles over a regular distribution of points, such as interpolating the vorticity distribution over a regular mesh. All these methods introduced an artificial viscosity into the fluid.

This work presents a new vortex method called Diffused Vortex Hydrodynamic (DVH). The DVH is a two dimensional particle vortex method in which is not necessary the use of any remeshing method tanks to the introduction of "Regular Point Distribution" (RPD) in the diffusion process. The DVH can be applied to perform high Reynolds simulations of flows around bodies with arbitrary shapes thanks to the use of RPDs and to the introduction of a so called visibility mask to perform diffusion in presence of bodies with edges such as squared cylinders or airfoils.

A RPD is a set of equispaced points without any topological connection. During the diffusion process each vortex gives its diffusive contribution to RPDs nodes using the fundamental solution of the heat equation, after the diffusion of all vortices a new set of regularly spaced particles is generated at the RPDs nodes location, substituting the former one. This procedure avoids the formation of holes and accumulations in the vorticity distribution without the use of any remeshing method.

In the region close to solid bodies RPDs are generated using the packing algorithm described in Colagrossi et al. (2012), this algorithm adapt the distribution of points to the body contour allowing to treat flows around bodies with complex geometry. This algorithm is very fast and efficient, and, since it is based on particle-dynamic interactions, it can be directly embedded in the same code.

Far from the solid surfaces simple Cartesian lattices, with different size according to the distance from the body, can be used with the same function of RPDs. In the DVH model, all the different RPDs can overlap each other and can be characterized by different spatial resolutions, starting from the highest resolution one placed in the boundary layer region, to the coarser one placed far away from the body. In this way it is possible to reduce the number of vortices generated during the evolution while maintaining high resolution where necessary allowing for the simulations of long complex wakes at high Reynolds number.

An example of the ability of DVH to perform high Reynolds simulations is given by the simulations of he flow past an impulsively started cylinder up to

$Re = 50000$ and $Re = 100000$. These last results are, to our knowledge, the cylinder wakes with the highest Reynolds number simulated without using any turbulence models.

As an example of the use of the packing algorithm to generate RPDs around bodies with complex geometry, the flow around a smooth body with a cavity is also simulated for various angles of attack, in such a way to study the effect of the cavity on the lift and drag coefficient of the body and on the wake formation.

The DVH is suitable to simulate fluid flows around non-smooth bodies. In this case flow around squares, rectangles and airfoils with various angles of attack is simulated and the results are compared with those found in literature.

The evolution of vorticity distribution in free space is also simulated to better control the errors made in the diffusive and in the advective step respectively. Two classical problems are considered: the Lamb-Oseen problem and the merger of a pair of co-rotating vortices and the results are compared with that obtained with a SPH solver.

1.2 STRUCTURE OF THE THESIS

The thesis is formally divided into three parts. In the first one a comprehensive state-of-the art regarding Vortex Methods in terms of the vorticity discretization and the methods used to evaluate advection and diffusion of the vortices is presented (chapter 2), toghether with a brief description of the Diffused Vortex Hydrodynamics (chapter 3).

In the second part a detailed description of the computational methods used in the present work is given. In chapter 4 a detailed description of the DVH method is given, starting from the governing equation to the discretized one. Because also SPH is used in some simulations, chapter 5 is devoted to the description of the theory of this method. Because a wide use of RPDs is made through all the simualtions presented, a description of the generation of these ensemble of points is given in chapter 6.

The last part of the thesis contains all the numerical results obtained and is divided into three sections. In the first part (section 7) are presented the simulations of vorticity distribution in free space with the comparison with the SPH solver. Section 8 contains the results obtained simulating the flow past smooth bodies with various geometries at various Reynolds numbers, while in section 9 the simulations of flow past bodies with edges are presented.

1.3 MAJOR FINDINGS

In this work the Diffused Vortex Method is tested against various problem and compared with SPH simulations and results present in literature. The problems can be divided in two categories: the evolution of vorticity distributions in free space and the flow past bluff bodies. The latter category is divided into two main parts: the study of the flow past regular bluff bodies (circular, elliptic and C-shaped cylinders) and the study of the flow past bodies with edges (squares, rectangles and airfoils).

Vorticity distribution in free space: Lamb-Oseen problem

The evolution of a Gaussian distribution of vorticity is studied, the results are compared with the exact solution available for the problem and the error on the vorticity and velocity distribution are evaluated.

A first series of simulations without advection is performed so to better control the error coming from the solution of the diffusive step, this test corresponds to the limit $Re \to 0$. The errors on the vorticity distributions shows that varying the spatial resolution is possible to find two distinct regimes: a first one for low spatial resolutions where the error reduces and a second one, for higher resolutions, where the error remains constant. This behaviour is typical of meshless methods.

A second series of simulations is performed for various Reynolds number considering also advection. The error on the vorticity field increases with the Reynolds number, as expected, while the error on the velocity field shows an almost constant convergence ratio.

The same simulations were also performed with a SPH solver and the results were compared.

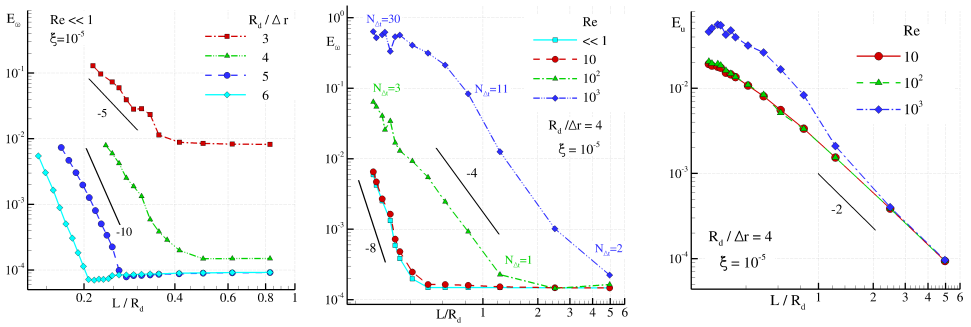

Figure 1.1: Left: Maximum relative maximum error over vorticity as function of L/R_d for various ratio $R_d/\Delta r$ and $\xi = 10^{-5}$. Center: Maximum relative error over vorticity as function of L/R_d for various Reynolds numbers and fixed ratio $R_d/\Delta r$. Right: Relative maximum error over velocity as function of L/R_d for various Reynolds numbers and fixed ratio $R_d/\Delta r$.

Vorticity distribution in free space: Merger of a pair of co-rotating vortices

The evolution of a pair of co-rotating vortices is studied for various Reynolds numbers. A convergence result is shown for $Re = 18850$ evaluating errors on the second momentum of the vorticity field and the excess energy showing an almost constant rate of convergence. The same simulations were also performed with a SPH solver and the results were compared.

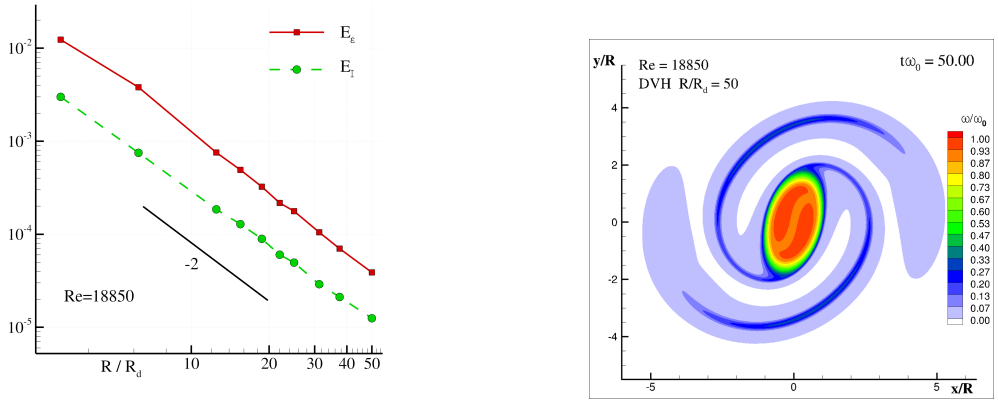

Figure 1.2: Merging of a pair of co-rotating vorticity patches. Left: Errors on the second momentum of vorticity field and the excess energy. Right: Vorticity field at time $t\omega_0 = 50.0$.

Regular bluff bodies: circular cylinders

The flow past circular cylinder at $Re = 9500$ is simulated and the results obtained (drag coefficients) are compared with Koumoutsakos and Leonard (1995) showing good agreement. Due to the computational resources now available we are able to simulate a much longer evolution respect to Koumoutsakos and Leonard (1995). The evolution of the flow at higher Reynolds numbers, up to $Re = 100000$, is also simulated. We were not able to find in the literature numerical solutions at the two highest Reynolds numbers presented here (without using any turbulence models). Therefore we think that the presented results can be useful also for other readers who need to test numerical solvers at these viscosity levels. Covering a such wide range of Reynolds numbers a plot of the time averaged drag coefficient at various Re is possible showing good agreement with the results in Singh and Mittal (2005).

Regular bluff bodies: elliptic cylinders up to $Re = 10000$

The flow past an inclined elliptic thin cylinder (axis ratio 0.1) is simulated for Reynolds numbers up to 3000 to show the variations in the wake formation. For $Re = 3000$ a comparison with results present in literature is also possible

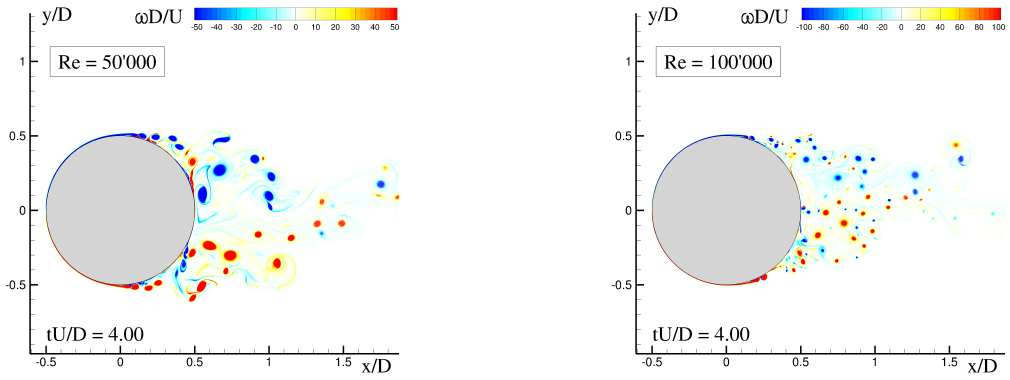

Figure 1.3: Flow around an impulsively started circular cylinder: vorticity field at time $tU/D = 4$.Left: $Re = 50000$. Right: $Re = 100000$.

(Nair and Sengupta (1997) and Huang and Huang (2013)). The flow past an inclined elliptic cylinder (axis ratio 0.25) at $Re = 10000$ is also simulated and the results are compared with Nair and Sengupta (1997). A convergence result is obtained with an inclined elliptic cylinder (axis ratio 0.4) at $Re = 500$. The convergence is evaluated on the drag coefficient evaluating a convergence ratio of about 2. For this case a comparison with SPH is also possible.

Regular bluff bodies: C-shaped cylinders

To test the DVH method with body of more general shape a smooth body composed by four semicircles (resembling a "C") is used. The simulations are performed at $Re = 2000$ with various angle of attack, showing the effect of a body with cavity in the wake formation and on the lift and drag coefficient.

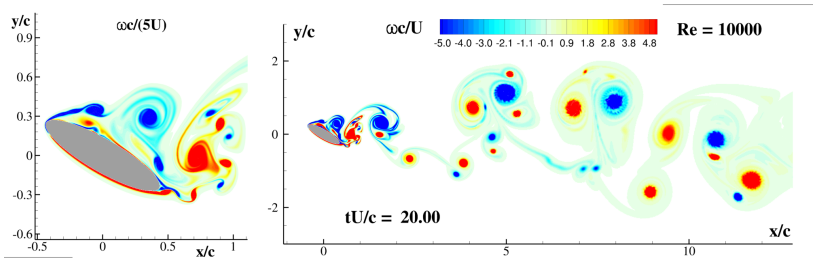

Figure 1.4: Evolution of the vorticity field for $c/\Delta r = 1000$ for an elliptical cylinder (axis ratio 0.25, $\alpha = 30°$) at $Re = 10000$. Left: enlarged view close to the body. Right: wake field.

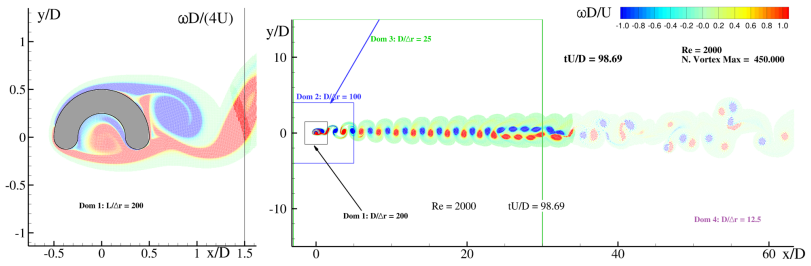

Figure 1.5: Flow around a C-Shape body at Re = 2000 with $\alpha = 0°$: evolution of the vorticity field past the body

Bluff bodies with edges: squares and rectangles

A series of simulations at Re = 200 using squares and rectangles at various angle of attack is performed to test the new diffusion algorithm in presence of bodies with edges. The results are compared with Steggel (1998).

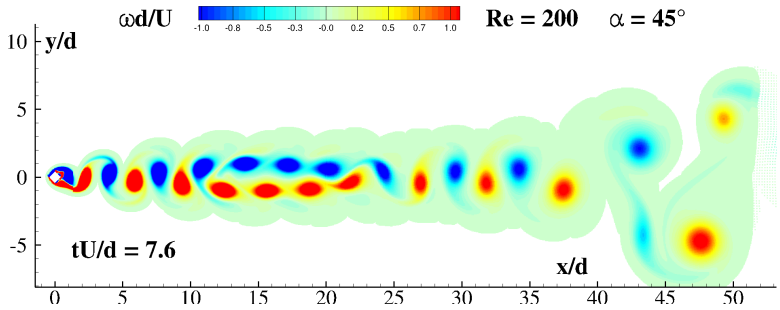

Figure 1.6: Vorticity field for a squared cylinder at Re = 200

Bluff bodies with edges: airfoils

The flow past an inclined (angle of attack alpha = 4°) NACA0008 profile is simulated for two different Reynolds numbers Re = 2000 and RE = 6000, comparing the results with those present in literature (Mittal et al. (2008)).

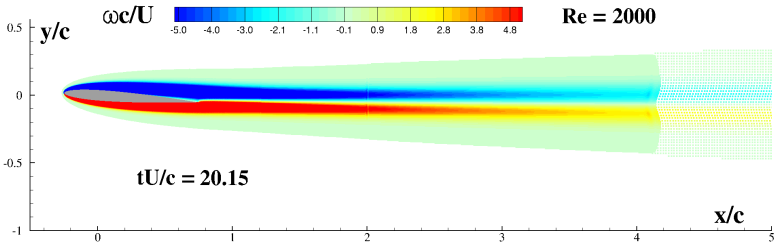

Figure 1.7: Vorticity field for NACA0008 profile with angle of attack $\alpha = 4°$ and Re = 2000

Bluff bodies with edges: waterline of a DDG51 hull

A two dimensional simulation of the water line of a hull DDG51 has been performed at $\mathrm{Re} = 100000$. The ship is supposed to advance with a steady drift angle $\alpha = 30°$, with a low Froude number $\mathrm{Fr} = 0.01$ in order to guarantee that the free surface remains unperturbed (no ship waves generation) as may happen for a ship maneuvering in a harbour.

This case is of great interest as an example of the complex vorticity field generated by norrow object at an high Reynolds number.

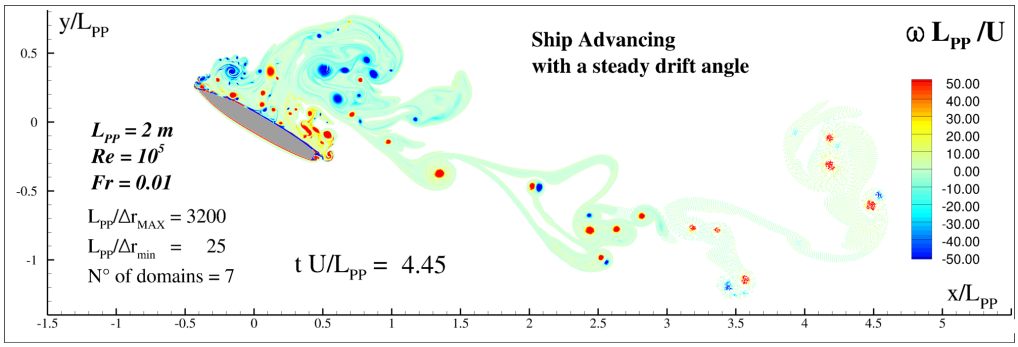

Figure 1.8: Vorticity field generated by the waterline of a DDG51 shiphull advancing with a steady drift angle $\alpha = 30°$ at a low Froude number $\mathrm{Fr} = 0.01$

Part I

VORTEX PARTICLE METHODS

2 VORTEX METHOD STATE OF ART

The first simulation made using a particle vortex method was made by Rosenhead (1931). He studied the motion of a vortex sheet at the interface of discontinuity in the velocity field inside an inviscid fluid of given density. A great improvement in the development of the method was given by Chorin (1973) with the introduction of the operator splitting technique in which the evolution of the vorticity field described by the Navier-Stokes equation, is divided into two steps. In the first step the fluid is considered inviscid and the evolution of the vorticity field is governed by the Euler equation. In the second step the velocity of the fluid is neglected and the vorticity undergo a diffusion process governed by the heat equation.

Since then a great number of different vortex methods have been used and they can be described using three main categories:

- vorticity field discretization;
- velocity field evaluation;
- solution of the heat eqaution.

A brief description of the existing vortex methods will be given in the following sections using the above categories. Since vortex methods are based on a Lagrangian formulation, he vorticity distribution is affected by a spatial deterioration in which the vortex elements (composing the discrete vorticity field) are brought afar from each other during the simulation, creating rarefaction and clusterization in the vorticity distribution. To avoid this problem

in such a way to describe DVH using the existing categories and giving a short explanation of the method itself. Detailed description of DVH method will be given in section 4.

Because the DVH will be also used to study vorticity generation and wake evolution in flow past bluff bodies, section 3.2.4 is dedicated to the explanation of the enforcement of the no slip boundary condition and the vorticity generation at boundaries. To avoid this problem many different methods,depending on the discretization technique adopted, have been introduced. In section 2.4 will be given a description of the most used methods.

A more detailed work regarding the state of art about vortex methods can be found in Stock (2007).

2.1 VORTICITY DISCRETIZATION

2.1.1 Vortex particle method

The first simulation made using a particle vortex method was made by Rosenhead (1931) to study the motion of a vortex sheet at the interface of discontinuity in the velocity field inside an inviscid fluid of given density.

In the method proposed by Rosenhead the vorticity distribution is described as:

$$\omega = \sum_{i=1}^{N} \Gamma_i \delta_{\mathbf{r}_i}(d\mathbf{r})$$

where δ is the two dimensional Dirac delta distribution and Γ_i is the circulation of each vortex.

In absence of boundaries the velocity field, for an inviscid flow in a 2D framework, can be calculated using the Biot-Savart equation:

$$\mathbf{u}(\mathbf{r}_i, t) = -\frac{1}{2\pi} \sum_{j=1}^{N} \Gamma_j(t) \frac{\mathbf{e}_3 \times (\mathbf{r}_i - \mathbf{r}_j)}{|\mathbf{r}_i - \mathbf{r}_j|^2}$$

then the evolution of the vorticity field is obtained by displacing the vortex particles by:

$$\frac{d\mathbf{r}_i}{dt} = \mathbf{u}(\mathbf{r}_i, t).$$

being $\mathbf{r}_i$ the position of the i-th vortex particle.

The singular nature of both the point vortex discretization and of the Biot-Savart kernel may lead to chaotic behaviours in the vortex evolution and, in general, such a scheme may not lead to a convergent solution.

To solve this problem one can either desingularize the point vortex distibution using the so called vortex blob method, or desingularize the Biot-Savart kernel. Although these two methods use different assumptions, they lead to the same result: the well posedness of the vortex sheet.

Following Leonard (1980), in the vortex blob method the vorticity is described as follows

$$\omega(\mathbf{r}) = \sum_{i=1}^{N} \Gamma_i \int W_\epsilon^{(i)}(\mathbf{r} - \mathbf{z}) \delta_{\mathbf{r}_i}(d\mathbf{z}) = \sum_{i=1}^{N} \Gamma_i W_\epsilon^{(i)}(\mathbf{r} - \mathbf{r}_i)$$

where $W_\epsilon^{(i)}$ is the normalized distribution of a vortex located in $\mathbf{r}_i$:

$$W_\epsilon^{(i)}(\mathbf{y}) = \frac{1}{\epsilon_i^2} W\left(\frac{|\mathbf{y}|}{\epsilon_i}\right)$$

where f is a function common to all vortices. Clearly the factor ϵ can be regarded as the core radius of the blob.

Thus the velocity field can be calculated in the following way

$$\mathbf{u}(\mathbf{r}_i, t) = \sum_{j=1}^{N} \Gamma_j \mathbf{K}_\epsilon(\mathbf{r}_i, \mathbf{r}_j)$$

where

$$\mathbf{K}_\epsilon(\mathbf{r}_i, \mathbf{r}_j) = \int \mathbf{K}(\mathbf{r}_i, \mathbf{z}) W_\epsilon^{(j)}(\mathbf{z} - \mathbf{r}_j) d\mathbf{z}.$$

A comprehensive discussion about vortex particle and vortex blob method can be found in Leonard (1980).

2.1.2 Vortex sheet method

Following Cottet and Koumoutsakos (2000) and Agishtein and Migdal (1989), a vortex sheet is a distribution of vorticity concentrated on a surface for a three dimensional flow (or a curve for a two dimensional flow). Consider now the surface $\gamma(\xi)$ with $\xi = (\xi_1, \xi_2) \in \Pi$, $\Pi \subset \mathbb{R}^2$ on which is defined the normal vector $\mathbf{n}(\xi, t)$. We can then consider a distribution of vorticity concentrated on the surface $\gamma(\xi)$, i.e. $\omega(\xi) = \alpha(\xi)\delta(\gamma(\xi))$, where $\alpha(\xi)$ is the intensity of the vortex distribution and δ is the three dimensional Dirac delta function.

The evolution of the vortex distribution is then determined by the motion of the surface $\gamma(\xi)$

$$\frac{\partial \gamma}{\partial t} = \mathbf{u}(\gamma(\xi), t).$$

On the vortex sheet surface the velocity field presents a discontinuity in the component tangent to the vortex sheet itself. Calling $\mathbf{u}(\mathbf{r}^+, t)$ and $\mathbf{u}(\mathbf{r}^-, t)$ the tangent components of the velocity field evaluated on the two side of the vortex sheet itself ($\mathbf{r}^+$ and $\mathbf{r}^-$ respectively), it is possible to define the discontinuity in the velocity field of the following way

$$\delta\mathbf{u} = \mathbf{u}(\mathbf{r}^+, t) - \mathbf{u}(\mathbf{r}^-, t).$$

It is now easy to see that the function $\alpha(\xi)$ gives a measure of this discontinuity, in fact:

$$\alpha(\xi) = \int_{\xi_0}^{\xi} \delta u(\xi') d\xi' \tag{2.1}$$

where ξ_0 and ξ are two points on the vortex sheet. The shape of the contour used in the integral of eq- (2.1) is no relevant because the curl of the integrand vanishes. In fact because the vorticity is present only on the surface γ every integral $\oint \mathbf{u} d\xi$ on every closed curve not intersecting the surface vanishes, thus the above expression represents the circulation along a loop intersecting the surface γ. It is possible deform this loop as long as it does not intersect the surface in more than two points, making the loop integral a function of the intersection points only rather than a functional of the loop.

The vortex sheet can be discretized in various ways. Many researchers represented it as a collection of filaments or particles but the first to use a three dimensional vortex method based on vortex sheets were Agishtein and Migdal Agishtein and Migdal (1989) where they discretize the vortex sheet using flat triangles.

In both particle and sheet vortex method one must discretize a distribution of vorticity into points, each carrying its own circulation, but while in the first one there is no topological connection between points, in the latter one these connections must be preserved during the motion of the vortex sheet.

Many authors also used discretized vortex sheet elements in the computation of two and three dimensional boundary-layer flows to track vorticity diffusion into the fluid, the first being Chorin (1978) followed by Bernard (1995), Bernard (1996) and Gharakhani and Ghoniem (1997).

2.1.3 Vortex filament method

A possible generalization of the two dimensional vortex blob method to three dimensions is the use of a collection of vortex tubes or filaments to discretize the vorticity field.

By Kelvin's theorem the circulation of the i-th filament is given by

$$\Gamma_i = \int \omega \, d\mathbf{A} \tag{2.2}$$

where the integral is extended over the core of the filament. If the fluid is considered inviscid and with constant density the circulation Γ_i is constant in time and the filament moves as a material line.

Following Cottet and Koumoutsakos (2000) and Leonard (1980) a vortex filament is then a vorticity field that is concentrated on a curve that is either closed or extending to infinity. Its direction is given by the local tangent on each point of the curve and its strength is given by the vorticity flux across a cross section of the filament. For a collection of vortex filaments one can think in terms of centerlines of vortex tubes, with longitudinal walls parallel to the vorticity field and centered around each filament.

For a single space curve C_i a vorticity field concentrated on it takes the following form

$$\omega_i(\mathbf{r}) = \Gamma_i \int_{C_i} W_\epsilon(\mathbf{r} - \mathbf{r}_i(s)) \frac{\partial \mathbf{r}_i}{\partial s} ds, \ \forall \mathbf{r} \in \mathbb{R}^3$$

where Γ is the circulation of the filament, $r_i(s)$ is the space curve parametrized by the arc length s and W_ϵ is a smooth approximation of the three dimensional Dirac delta function such that

$$\int W_\epsilon(\mathbf{r}) d\mathbf{r} = 1 \tag{2.3}$$

and

$$W_\epsilon(|\mathbf{r}-\mathbf{r}'|) = \frac{1}{\epsilon^3} W\left(\frac{|\mathbf{r}-\mathbf{r}'|}{\epsilon}\right). \tag{2.4}$$

The vorticity field generated by a set of N vortex filaments is given by

$$\omega(\mathbf{r}) = \sum_{i=1}^{N} \omega_i(\mathbf{r}) = \sum_{i=1}^{N} \Gamma_i \int W_\epsilon(\mathbf{r}-\mathbf{r}_i(s)) \frac{\partial \mathbf{r}_i}{\partial s} ds. \tag{2.5}$$

and the velocity field induced by this vorticity distribution can be calculated as

$$\mathbf{u}(\mathbf{r}) = -\frac{1}{4\pi} \int \frac{[\mathbf{r}-\mathbf{r}'] \times \omega(\mathbf{r}', t)}{|\mathbf{r}-\mathbf{r}'|^3} d\mathbf{r}' + \nabla\phi \tag{2.6}$$

where ϕ is the velocity potential induced by the presence of solid walls within the fluid domain.

Substituting now the eq. (2.5) in the Biot-Savart integral of eq. (2.6) is possible to obtain the following expression:

$$\mathbf{u}(\mathbf{r}) = -\frac{1}{4\pi} \sum_{i=1}^{N} \Gamma_i \int \frac{|\mathbf{r}-\mathbf{r}_i(s,t)| \times (\partial \mathbf{r}_i/\partial s) q(|\mathbf{r}-\mathbf{r}_i|/\epsilon)}{|\mathbf{r}-\mathbf{r}_i(s,t)|^3} ds \tag{2.7}$$

where

$$q(x) = 4\pi \int_0^x f(z) z^2 dz. \tag{2.8}$$

As for the vortex sheet, the vortex filaments are discretized into connected points. Early filamnets methods used straight lines to connect these points but higher order splines have been used like the third order splines introduced by Ashurst and Meiburg (1988).

A particular problem arises in filament methods when a number of closely packed filaments are used to represent large vorticity distributions, in this case in finite time these structures will thin in the direction normal to the filament axes (see *e.g.* Martin and Meiburg (1991), Sakajo (2001)). Solution to this problem involves remeshing techniques that will be briefly treated in section 2.4.

2.2 VELOCITY FIELD EVALUATION

As we have seen in the previous sections the vorticity field for a vortex method is represented by a collection of vorticity elements (particles, filaments or sheets) that are moved according to the velocity field generated by the distribution of vorticity itself and by the presence of solid boundaries within the fluid domain, namely

$$\mathbf{u}(\mathbf{r}) = \int \mathbf{K}(\mathbf{r}, \mathbf{r}') \omega(\mathbf{r}', t) d\mathbf{r}' + \nabla\phi$$

where ϕ is the velocity potential induced by the presence of solid walls within the fluid domain and $\mathbf{K}(\mathbf{r}, \mathbf{r}')$ is given by

$$\mathbf{K}(\mathbf{r}, \mathbf{r}') = \nabla^{\perp} G(\mathbf{r}, \mathbf{r}'); \quad G(\mathbf{r}, \mathbf{r}') = \frac{1}{2\pi} \ln |\mathbf{r} - \mathbf{r}'|.$$

In the following sections we will briefly describe the most used methods to evaluate the Biot-Savart integrals: direct evaluation of the Biot-Savart integral, Fast Multiple Method and Vortex-in-Cell method.

2.2.1 Biot-Savart integral and Fast Multipole Method

The velocity field quantified by the Biot-Savart law is:

$$\mathbf{u}(\mathbf{r}, t) = \int \mathbf{K}(\mathbf{r}, \mathbf{r}')\omega(\mathbf{r}', t)\, d\mathbf{r}'.$$

If, for example, we are using a vortex particle method to describe the vorticity field, i.e.

$$\omega = \sum_{j=1}^{N} \Gamma_j \delta_{\mathbf{r}_j}(d\mathbf{r}) \tag{2.9}$$

the discretized Biot-Savart law then reads

$$\mathbf{u}(\mathbf{r}_i, t) = \sum_{j=1}^{N} \Gamma_j \mathbf{K}(\mathbf{r}_i, \mathbf{r}_j) \tag{2.10}$$

where $\mathbf{r}_i$ is the position of the i-th vortex.

Using directly eq. (2.10) to evaluate the velocity field would lead, for every time step, to an operation count of order $\mathcal{O}(N^2)$, being N the number of vortices in the computational domain.

The speed up of this summation is one of the major issue in creating an efficient and accurate vortex method. A simple way to increase the efficiency of the Biot-Savart velocity evaluation is to use parallel algorithms (Sethian et al. (1992), Gharakhani and Ghoniem (1996)) but it would only produce a linear speed-up.

Other methods to speed up the evaluation of the velocity field are the use of long range cut-off to ignore the influence of far vortices on the velocity of the considered one (see e.g. Chorin (1981)).

Another common method used to increase the computational efficiency of the evaluation of the Biot-Savart integral is the use of treecode/fast multipole methods. In this case the computational domain is recursively divided into panels, until every panel contains, at most, a fixed number of vortices. While constructing the domain subdivisions, the panels are given a hyerarchical tree structure.

Running through the panels the velocity of each vortex will be calculated using the Biot-Savart integrals to account for the interaction with the vortices in the nearest neighbours of the actual panel, while the effect of the other vortices will be approximated using a multipole expansion.

2.2.2 Vortex Particle-in-Cell method

The first Particle-In-Cell (PIC) method was used for hydrodynamic problems by Evans et al. (1957), since then PIC methods have been widely used by many researchers giving birth to the Cloud-In-Cell, introduced by Birdsall and Fuss (1997) for plasma particle flows.

Following Liu and Doorly (2000), in PIC method the vorticity distribution is discretized into particles and placed inside a temporary Eulerian mesh. The strength of each particle is then interpolated on the mesh points and the contribution summed to obtain the vorticity distribution on the grid nodes. At this step the velocity field is evaluated on the Eulerian mesh by solving the following Poisson equation:

$$\Delta \mathbf{u} = -\nabla \times \omega \tag{2.11}$$

where $\omega = (\omega_1, \omega_2, \omega_3)$ in 3D or $\omega = \omega e_3$ for 2D problems.

The velocity field on the Eulerian mesh $\mathbf{u}_g$ is then interpolated over the particles to find the velocity of each vortex $\mathbf{u}_i$ then each vortex is displaced according to the following equation

$$\frac{d\mathbf{r}_i}{dt} = \mathbf{u}_i \tag{2.12}$$

where $\mathbf{r}_i$ is the position of the i-th vortex.

After the advection, the particle strength of each vortex is again interpolated over the Eulerian grid to obtain a new distribution of vorticity over the mesh nodes and solve the following equation

$$\frac{\partial \omega}{\partial t} = \omega \cdot \nabla \mathbf{u} + \nu \Delta \omega. \tag{2.13}$$

For 2D problems the previous equation reduces to the heat equation for the vorticity field

$$\frac{\partial \omega}{\partial t} = \nu \Delta \omega. \tag{2.14}$$

The solution obtained for the vorticity field must now be back interpolated over the particles to obtain the updated vorticity distribution.

The advantage of this method is that the only requirement needed is that the velocity must be divergence free, on the other and other than the errors coming from the solution of the Poissons equations there is another source of errors that is the interpolation procedure.

2.3 DIFFUSION

Using the operator splitting scheme introduced by Chorin (1973) the advection and the diffusion of the vorticity field are treated separately. During the diffusion the fluid velocity is neglected while the diffusion of the vorticity field is accounted by solving the following equation

$$\frac{\partial \omega}{\partial t}(\mathbf{r}, t) = \nu \Delta \omega$$

where ν is the cinematic viscosity of the fluid.

In this section we will briefly describe the most used methods adopted to solve the heat eqaution.

2.3.1 Random walk

The random vortex method was introduced by Chorin (1978) and is based on the use of the operator splitting technique together with a solution of the heat equation obtained using a stochastic interpretation of the diffusion process.

In fact being ω a weak solution of the Navier-Stokes equation it is possible to define a stochastic process $\mathbf{r}$ as a solution of the following stochastic differential equation

$$d\mathbf{r}(t) = \mathbf{u}(\mathbf{r}(t), t)dt + \sqrt{2\nu} d\mathbf{w}_t \tag{2.15}$$

where $\mathbf{u}$ is the velocity field given by the Biot-Savart integral

$$\mathbf{u}(\mathbf{r}, t) = \int \mathbf{K}(\mathbf{r}, \mathbf{r}')\omega(\mathbf{r}', t)d\mathbf{r}' \tag{2.16}$$

and w_t is a Wiener process.

Discretizing the vorticity field into particles gives a stochastic equation for the motion of each vortex

$$d\mathbf{r}_i(t) = \sum_{j=1}^{N} \Gamma_j \mathbf{K}(\mathbf{r}_i, \mathbf{r}_j) + \sqrt{2\nu} d\mathbf{w}_i(t) \tag{2.17}$$

where $\mathbf{r}_i$ is the position of the i-th vortex and N is the total number of vortices in the computational domain.

Using the operator splitting technique it is possible to evaluate the velocity field $\mathbf{u}$ using, for example, one of the methods described in section 2.2, while the diffusion is accounted in the diffusive step giving to each vortex particle a random displacement.

Although of very simple implementation, this method needs a great number of particles compared to the Reynolds number to reach convergence (see *e.g.* Leonard (1980) and Milinazzo and Saffman (1977)) while the convergence of the diffusion method using Wiener processes was proven to converge to the heat equation by several authors as Hald (1986), Puckett (1989) and Mortazavi et al. (1996).

2.3.2 Core-spreading

The Core-Spreading technique was first used by Kuwahara and Takami (1973) and later on used by several researchers (see for example Leonard (1980)) to solve the viscous part of the Navier-Stokes equation.

This technique derives from the solution to the two-dimensional heat equation with initial condition a single point vortex

$$\omega_0(\mathbf{r}) = \Gamma_0 \delta(\mathbf{r} - \mathbf{r}_0) \tag{2.18}$$

where Γ_0 is the initial circulation concentrated at point $\mathbf{r}_0$. In this case the solution of the heat equation for the total circulation of the system gives

$$\Gamma(t) = \Gamma_0 \left(1 - \exp\left\{-\frac{|\mathbf{r} - \mathbf{r}_0|^2}{4\nu(t - t_0)}\right\}\right). \tag{2.19}$$

This means that one can approximate the viscous decay of a 2D vortex particle by reducing the circulation associated to the particle or increasing its effective radius. The same technique can be applied to 3D vortex filament also.

Although Greengard (1985) showed that this method approximates the wrong equation, this problem can be corrected by an instantaneous reconfiguration of the large vortex blobs to thinner ones (Rossi (1996) and Benson et al. (1989)). Advantages of the method are shown in Rossi (1996) like its fully deterministic character or the freedom from flow geometry considerations.

2.3.3 Particle Strength Exchange (PSE)

The particle strength exchange is a method to solve the diffusive part of the Navier-Stokes equation first proposed by Mas-Gallic (1987) in his Phd thesis and then studied in details for isotropic and anisotropic diffusion in Degond and Mas-Gallic (1989b) and Degond and Mas-Gallic (1989a).

Following the description made by Winckelmans and Leonard (1993) In the particle strength exchange (PSE) the Laplacian operator in the heat equation is substituted by

$$\Delta f(\mathbf{r}) = \frac{2}{\epsilon^2} \int (f(\mathbf{r}') - f(\mathbf{r})) g_\epsilon(\mathbf{r} - \mathbf{r}') d\mathbf{r}' \tag{2.20}$$

where $g_\epsilon(\mathbf{r}) = (1/\epsilon^3) g(|\mathbf{r}|/\epsilon)$ is a smoothing function.

Considering now a general convection-diffusion problem the Navier-Stokes equation with the PSE approximation of the Laplacian operator is

$$\frac{\partial \omega}{\partial t} + \nabla \cdot (\mathbf{u}\omega) = \frac{2\nu}{\epsilon^2} \int (\omega(\mathbf{r}') - \omega(\mathbf{r})) g_\epsilon(\mathbf{r} - \mathbf{r}') d\mathbf{r}'. \tag{2.21}$$

Consider now the following discretization of the vorticity field

$$\omega(\mathbf{r}, t) = \sum_{i=1}^{N} V_i(t)\omega_i(t) g_\epsilon(\mathbf{r} - \mathbf{r}_i) \tag{2.22}$$

where $\omega_i(t)$ and $V_i(t)$ are the vorticity and the volume of the vortex with position $\mathbf{r}_i$ a time t, the equations to solve to determine the evolution of the N vortices now read

$$\begin{cases} \dfrac{d\mathbf{r}_i}{dt} = \mathbf{u}(\mathbf{r}_i, t) \\ \dfrac{dV_i}{dt} = V_i(t)\nabla \cdot \mathbf{u}(\mathbf{r}_i, t) \\ \dfrac{d}{dt}(V_i(t)\omega_i(t)) = \dfrac{2\nu}{\epsilon^2} V_i(t) \displaystyle\sum_{j=1}^{N} V_j(t)(\omega_j(t) - \omega_i(t)) g_\epsilon(\mathbf{r}_j - \mathbf{r}_i) \end{cases} \tag{2.23}$$

The last equation of system (2.23) gives the approximated solution to the diffusion of the vortices governing the exchange of vorton strength $V\omega$ between neighbours based on the cinematic viscosity ν.

This also means that the PSE rely on effective search strategy to efficiently identify every vortex within a given distance from a point, this can be done by properly dividing the computational domain and using search tree algorithm to speed-up this process.

2.3.4 Vorticity Redistribution Method (VRM)

Another deterministic method to solve the diffusive step is the Vorticity Redistribution Method (VRM). In this method, following Shankar and Dommelen (1996), the vorticity of each vortex is redistributed among the vortices inside a radius Rh_ν from the considered vortex, where R is a parameter to be setted at the start of the simulation and h_ν is the typical diffusive length:

$$h_\nu = \sqrt{\nu \Delta t}$$

and Δt is the diffusive time step.

Calling f_{ij}^n the fraction of vorticity moved from vortex i to vortex j at the n-th step, di vorticity distribution changes from

$$\omega^n(\mathbf{r}, t) = \sum_i \Gamma_i^n \phi_\delta(\mathbf{r} - \mathbf{r}_i)$$

to

$$\omega^{n+1}(\mathbf{r}, t) = \sum_i \sum_j f_{ij}^n \Gamma_i^n \phi_\delta(\mathbf{r} - \mathbf{r}_j),$$

where $Gamma_i^n$ is the circulation of the i-th vortex and $\phi_\delta(\mathbf{r})$ is a vortex core function with the following form

$$\phi_\delta(\mathbf{r}) = \frac{1}{\delta^2}\phi_\delta\left(\frac{\mathbf{r}}{\delta}\right). \tag{2.24}$$

Taking the Fourier transform of equation (2.24) is possible to obtain the following expression

$$\hat{\omega}^{n+1} = \hat{\phi}(\delta\mathbf{k}) \sum_i \Gamma_i^n e^{-i\mathbf{k}\cdot\mathbf{r}_i} \sum_j f_{ij}^n e^{-i\mathbf{k}\cdot(\mathbf{r}_i-\mathbf{r}_j)}, \tag{2.25}$$

comparing this expression with the Fourier transform of the exact diffusion of the vorticity field

$$\hat{\omega}_{exact}^{n+1} = \hat{\phi}(\delta\mathbf{k}) \sum_i \Gamma_i^n e^{-i\mathbf{k}\cdot\mathbf{r}_i} e^{-i|\mathbf{k}|^2\nu\Delta t}$$

and equating the same order coefficient up to the desired order is it possible to obtain a system of equations for the redistribution fractions f_{ij}^n.

However the system of equations obtained not always has a solution as, for example, in the case in which the number of vortex inside the radius Rh_ν is less than the number of equations chosen to determine the redistribution coefficients. In this case vortices with zero circulation are added until the system has a positive solution.

Although similar to PSE the Vorticity Redistribution Method can conserve circulation and vorticity moments up to an arbitrarily high order (depending on the order of the system of equations solved), can fill holes in the vorticity distribution caused by Lagrangian distortion in the motion of the particles and therefore does not need remeshing procedures. However, as for PSE, it relies on effective search strategy to efficiently identify every vortex within a given distance from a point.

2.4 REMESHING

Due to the Lagrangian motion of the vortex particles, the vorticity distribution is affected by a spatial deterioration in which the vortices are brought afar from each other during the simulation, creating rarefaction and clusterization in the vorticity distribution. To avoid this problem many different methods have been introduced by several researchers depending on the discretization technique adopted for the vorticity field. In what follows a brief description of the most used methods will be given.

Using particle discretization of the vorticity field the velocity of the vortices can be evaluated by use of the Biot-Savart law:

$$\mathbf{u}(\mathbf{r}_i, t) = \sum_{j=1}^{N} \Gamma_j(t)\mathbf{K}_\epsilon(\mathbf{r}_i, \mathbf{r}_j) = \sum_{j=1}^{N} \omega(\mathbf{r}_j, t)\mathbf{K}_\epsilon(\mathbf{r}_i, \mathbf{r}_j)A_j \tag{2.26}$$

where $\mathbf{K}_\epsilon$ is a regularization of the Biot-Savart integral kernel and Γ_j is the circulation of the j-th vortex. In equation (2.26) it has been used the fact that it is possible, in general, to associate to every vortex an occupied volume A_j allowing to rewrite the circulation of each particle as $\Gamma_j = \omega_j A_j$.

One way to avoid the excessive clustering or rarefaction of the vortex particle due to the Lagrangian nature of their motion is to evaluate at each time steps the quadrature weights A_j (see *e.g.* Marshall and Grant (1996) and Strain (1996)).

Another possibility is to set a specific and fixed time interval to redistribute the vorticity distribution on a regular grid, generating a new set of particles with regular spatial distribution that substitute the former one. The strength of the new set of particles is set in such a way to recreate as accurately as possible the original vorticity distribution.

In general (see *e.g.* Nordmark (1991)) during the advective step the fluid is considered inviscid and an error on the evolution of the vorticity field can be defined as follows

$$E_\omega(t) = \left[A \sum_j \Gamma_j(t) - \Gamma_j(t_0) \right]^{1/2} \tag{2.27}$$

where $\Gamma_j(t_0)$ and $\Gamma_j(t)$ are the circulation at the initial time t_0 and at a generic time $t > t_0$ respectively and A is the area occupied by the the j-th vortex at t_0 (for simplicity it has been assumed an initial distribution in which every vortex occupy the same area).

It is possible to evaluate the error (2.27) at the end of each time step. If the ratio $E_\omega(t)/E_\omega(t_0)$ exceed a fixed threshold $\eta > 1$, a new set of vortex particles is generated on the positions of a regular mesh nodes. The circulations of the new vortices are found interpolating that of the former one on the nodes of the regular mesh. After this process the former vorticity distribution is substituted by the new one.

The use of an opportune interpolating function is critical to the correct implementation of this procedure: interpolating the circulation on a regular grid introduce in fact a numerical diffusion whose effects can be reduced by using interpolating functions that preserves vorticity momentums up to the desired order. Example of interpolating functions are the M_4' kernel, described in Hockney and J.W. (1988), (see *e.g.* Eldredge (2005)) or the Radial Basis Functions (see *e.g.* Barba et al. (2003)).

Other researchers used grid with varying cell size to better resolve the vorticity field near shedding object (see *e.g.* Cottet et al. (2000) and Ploumhans et al. (2004)) or introducing a methods that uses high order redistribution schemes to correctly redistribute particles in presence of solid bodies (Ploumhans and Winckelmans (2000) and Ploumhans et al. (2002)).

3 DIFFUSED VORTEX HYDRODYNAMIC

In section 2 has been presented a short review of the main characteristics of the most used vortex methods present in literature.

In this chapter will be presented, after a briefly recall of the equation governing the motion of a two dimensional incompressible viscous fluid (section 3.1), the main features of the new vortex method presented in this work, called Diffused Vortex Hydrodynamic (DVH in what follows), dividing them using the categories introduced in section 2:

- vorticity discretization (section 3.2.1),
- velocity field evaluation (section 3.2.2),
- solution of the heat eqaution (section 3.2.3),

in such a way to describe DVH using the existing categories and giving a short explanation of the method itself. Detailed description of DVH method will be given in section 4.

Because the DVH will be also used to study vorticity generation and wake evolution in flow past bluff bodies, section 3.2.4 is dedicated to the explanation of the enforcement of the no slip boundary condition and the vorticity generation at boundaries.

3.1 GOVERNING EQUATIONS

The equations governing the motion of a viscous fluid confined inside the portion of space Ω are:

$$\begin{cases} \dfrac{D}{Dt}\rho(\mathbf{r},t) &= - \rho(\mathbf{r},t)\nabla\cdot\mathbf{u}(\mathbf{r},t) \\ \rho(\mathbf{r},t)\dfrac{D}{Dt}\mathbf{u}(\mathbf{r},t) &= - \nabla p(\mathbf{r},t) + \mu\Delta\mathbf{u}(\mathbf{r},t) + \\ &\quad + (\lambda+\mu)\nabla(\nabla\cdot\mathbf{u}(\mathbf{r},t)) + \rho(\mathbf{r},t)\mathbf{F}(\mathbf{r},t) \end{cases} \tag{3.1}$$

where $\rho(\mathbf{r},t)$ is the density of the fluid, $\mathbf{u}(\mathbf{r},t)$ is its velocity, $p(\mathbf{r},t)$ the pressure field and $\mathbf{F}(\mathbf{r},t)$ are the external forces acting on the fluid. λ and μ are the volume and friction viscous coefficient respectively, while $\frac{D}{Dt}$ is the material deriveative defined as

$$\frac{D}{Dt}f(\mathbf{r},t) := \frac{\partial}{\partial t}f(\mathbf{r},t) + \mathbf{u}(\mathbf{r},t)\cdot\nabla f(\mathbf{r},t).$$

In our analysis we will consider only incompressible fluids, i.e. fluids for which the the material derivative of the density is identically zero

$$\frac{D}{Dt}\rho(\mathbf{r},t) = 0$$

so that the continuity equation reduces to

$$\nabla \cdot \mathbf{u}(\mathbf{r},t) = 0. \tag{3.2}$$

For simplicity we will consider only fluids with constant density $\rho(\mathbf{r},t) = \rho$.

Thus the equations for a viscous incompressible fluids are:

$$\begin{cases} \nabla \cdot \mathbf{u}(\mathbf{r},t) = 0 \\ \\ \dfrac{D\mathbf{u}}{Dt}(\mathbf{r},t) = -\dfrac{1}{\rho}\nabla p(\mathbf{r},t) + \nu\Delta\mathbf{u}(\mathbf{r},t) + \mathbf{F}(\mathbf{r},t) \end{cases} \tag{3.3}$$

where $\nu = \mu/\rho$ is the kinematic viscosity.

Equations (3.3) alone are not sufficient to describe the motion of the fluid. It is necessary to specify the boundary conditions for the velocity field on boundaries of the fluid domain Ω. Calling $\partial\Omega_b$ and $\partial\Omega_\infty$ the boundaries on a solid surface of a body immersed in the fluid and the boundaries at infinity respectively, the boundary conditions can be written as

$$\begin{cases} \mathbf{u}(\mathbf{r},t) = \mathbf{u}_b(\mathbf{r},t), \quad \forall t \geqslant t_0,\ \forall \mathbf{r} \in \partial\Omega_b \\ \\ \mathbf{u}(\mathbf{r},t) = \mathbf{u}_\infty(\mathbf{r},t), \quad \forall t \geqslant t_0,\ \forall \mathbf{r} \in \partial\Omega_\infty \end{cases} \tag{3.4}$$

where the first equation express the no slip boundary condition on the solid boundaries $\partial\Omega_b$, while the second equation reflect the condition of unperturbed flow at infinity. In eq. (3.4) t_0 is the initial time.

If we now consider the vorticity $\omega(\mathbf{r},t) = \nabla \times \mathbf{u}(\mathbf{r},t)$ and for $F(\mathbf{r},t)$ only gradient forces, equation (3.3) can be written as

$$\frac{D}{Dt}\omega(\mathbf{r},t) = \omega(\mathbf{r},t)\cdot\mathbf{u}(\mathbf{r},t) + \nu\Delta\omega(\mathbf{r},t). \tag{3.5}$$

Because we are interested in two dimensional flows, equation (3.5) in 2D became:

$$\frac{D}{Dt}\omega(\mathbf{r},t) = \nu\Delta\omega(\mathbf{r},t). \tag{3.6}$$

where $\omega(\mathbf{r},t)$ is now a scalar field.

Using the vorticity formulation of the Navier-Stokes equation has the advantage of eliminating the pressure field from the unknown variables allowing us to solve one less equation. On the other hand it is impossible to write a boundary condition on the vorticity variables or on its derivative in normal direction with respect to the body contour. It is possible to overcome this problem by introducing approximated boundary conditions on the velocity field such that $\mathbf{u}(\mathbf{r},t)$ satisfies the no slip condition on the body contour.

3.2 OPERATOR SPLITTING AND VORTEX PARTICLE DISCRETIZATION

The Navier-Stokes equation (3.6) simultaneously accounts for the advection and the diffusion of the vorticity field, according to the operator splitting scheme (Chorin 1973, Chorin 1978) these to step can be separately solved in the numerical procedure. Thus the numerical solution is obtained by solving, for each time step, an inviscid advection step governed by the Euler equation

$$\frac{\partial \omega}{\partial t} + \mathbf{u} \cdot \nabla \omega = 0$$

followed by a purely diffusive one governed by the heat equation

$$\frac{\partial \omega}{\partial t} = \nu \Delta \omega.$$

To take into account the presence of solid boundaries, a procedure to enforce the no slip boundary condition must be added between the two previous steps.

3.2.1 Particle discretization of the vorticity field

Following Chorin (1973) the vorticity field $\omega(\mathbf{r}, t)$ can be discretized in the following way

$$\omega_\epsilon(\mathbf{r}, t) = \sum_{i=1}^{N} \Gamma_i(t) W_\epsilon(|\mathbf{r} - \mathbf{r}_i|) \tag{3.7}$$

where W_ϵ is a smooth approximation of the Dirac delta function such that $W_\epsilon \to \delta$ as $\epsilon \to 0$. An example of mollifier function is the following Gaussian kernel:

$$W_\epsilon(|\mathbf{r} - \mathbf{r}_i|) := \frac{1}{4\pi\epsilon^2} \exp\left[\frac{|\mathbf{r} - \mathbf{r}_i|^2}{4\epsilon^2}\right]. \tag{3.8}$$

With a purely Lagrangian description of the velocity field there is the possibility of an excessive clustering or rarefaction of the vortex particles, leading to a poor evaluation of the vorticity field through eq. (3.7). To avoid this problem particle redistribution (or remeshing) procedure have been introduced by many researchers (see section 2.4 for a short review of the most used methods). These procedures, somewhat non-physical, have the advange to restore the consistency of equation (3.7) but, on the other hand, they introduce another font of errors in the form of a numerical dissipation of vorticity.

The DVH method avoids the use of such remeshing procedures because, following the the deterministic diffusion scheme proposed by Benson et al. (1989), the particles are given a new regular distribution during the diffusive step itself.

3.2.2 Advection

During the advective step the fluid is considered inviscid, so that the governing equation is the Euler equation

$$\begin{cases} \nabla \cdot \mathbf{u}(\mathbf{r}, t) = 0 \\ \frac{D}{Dt}\omega(\mathbf{r}, t) = 0 \\ \Delta\psi(\mathbf{r}, t) = -\omega(\mathbf{r}, t), \ \mathbf{u}(\mathbf{r}, t) = -\nabla^{\perp}\psi \end{cases} \tag{3.9}$$

together with the incompressible condition and the no slip boundary condition on the solid boundaries $\partial\Omega_b$. The velocity of the vorticity field can then be decomposed in the following way:

$$\mathbf{u} = \mathbf{u}_{\infty} + \mathbf{u}_{\omega} + \mathbf{u}' \tag{3.10}$$

where $\mathbf{u}_{\infty}$ is the unperturbed flow velocity, $\mathbf{u}_{\omega}$ is the velocity induced by the vorticity field itself

$$\mathbf{u}_{\omega}(\mathbf{r}) = \int_{\Omega} \mathbf{K}(\mathbf{r}, \mathbf{r}^{\star})\omega(\mathbf{r}^{\star})d\mathbf{r}^{\star},$$

and $\mathbf{u}'$ is the velocity due to the presence of solid boundaries

$$\mathbf{u}'(\mathbf{r}) = -\int_{\partial\Omega_b} \sigma(\mathbf{r}^{\star})\mathbf{K}^{\perp}(\mathbf{r}, \mathbf{r}^{\star})d\mathbf{r}^{\star} + \int_{\partial\Omega_b} \gamma(\mathbf{r}^{\star})\mathbf{K}(\mathbf{r}, \mathbf{r}^{\star})d\mathbf{r}^{\star}$$

where it has been introduced a description of the body using an inderect integral representation of the velocity field using distributions of sources σ and circulations γ (details about these last two terms will be given in section 4.2). In the previous equations the integral kernel $\mathbf{K}$ is given by:

$$\mathbf{K}(\mathbf{r}, \mathbf{r}') = \nabla^{\perp}G(\mathbf{r}, \mathbf{r}'); \quad G(\mathbf{r}, \mathbf{r}') = \frac{1}{2\pi}\ln|\mathbf{r} - \mathbf{r}'|.$$

The velocity field for a discrete set of vortex particles can be evaluated using the following equation

$$\begin{aligned} \mathbf{u}(\mathbf{r}_i, t) \ = \ \mathbf{u}_{\infty} \ &+ \ \sum_{j=1}^{N_v} \Gamma_j(t)\mathbf{K}_{\epsilon}(\mathbf{r}_i, \mathbf{r}_j) + \\ &+ \ \sum_{k=1}^{N_b} \left[\mathbf{K}_{\epsilon}(\mathbf{r}_i, \mathbf{r}_k)\gamma_k(t) - \mathbf{e}_3 \times \mathbf{K}_{\epsilon}(\mathbf{r}_i, \mathbf{r}_k)\,\sigma_k(t)\right]\Delta s \end{aligned} \tag{3.11}$$

where N_v is the total number of vortices inside the computational domain, N_b is the total number of points on the body contour with uniform spacing Δs and $\mathbf{K}_{\epsilon}$ is a regularization of the integral kernel $\mathbf{K}$.

Due to the high computational cost of the direct use of eq. (3.11), the velocity evaluation has been performed using a Fast Multipole Method.

Obtained the velocity field $\mathbf{u}$, the position of every single vortex will be displaced according to the following equation:

$$\frac{d}{dt}\mathbf{r}_i(t) = \mathbf{u}(\mathbf{r}_i, t) \tag{3.12}$$

where $\mathbf{r}_i(t)$ is the position of the i-th vortex at time t.

3.2.3 Diffusion

In the diffusive step the velocity of the vortices is neglected and the viscous effects are considered by solving the following heat equation:

$$\frac{\partial}{\partial t}\omega(\mathbf{r}, t) = \nu\Delta\omega(\mathbf{r}, t),\ \omega(\mathbf{r}, 0) = \Gamma_i\delta(\mathbf{r}) \tag{3.13}$$

Eq. (3.13) is solved for every vortex in the computational domain and, thanks to the linearity of this equation, the solution can be approximated as a sum of elementary solutions of the form

$$\omega(\mathbf{r} - \mathbf{r}_0, t - t_0) = \frac{\Gamma_0}{4\pi\nu(t - t_0)} \exp\left\{-\frac{|\mathbf{r} - \mathbf{r}_0|^2}{4\nu(t - t_0)}\right\}$$

where $\mathbf{r}_0$ and Γ_0 are the position and the circulation respectively of a point vortex at the initial time t_0.

"Regular Point Distributions" (RPDs) are used during the diffusive step. All the points belonging to the same RPD have a reciprocal distance close to a mean value Δr which characterizes the spatial resolution of the considered RPD. Each particle is associated with a given RPD and gives its diffusive contribution, using an elementary solution of the heat eqaution, to points of the associated RPD taking into accounts the effects of the presence of solid boundaries when necessary. After every vortex had given its diffusive contribution, the former vorticity distribution is substituted by a new one whose positions are the positions of the RPDs nodes and whose circulation is given by the diffusion process. Details on the approximation used in the diffusive step and on the solution of the heat equation in presence of general shaped boudnaries are given in section 4.6.

The use of RPDs to solve the diffusive step also prevents the eccesive clustering or rarefaction of the vortex particles without introducing, somewhat un-physical, redistribution procedures. At the end of the diffusive step infact the new set of vortices have a regular spatial distribution given by the RPDs nodes positions.

3.2.4 No slip boundary condition and body contribution to the velocity field

The use of the operator splitting scheme requires the introduction, between the advective and the diffusive step, of a procedure to enforce the no slip boundary conditions.

During the advective step in fact the solution of eq. (3.9) produces a velocity field which only satisfy a free slip boundary condition, violating the no slip boundary condition of the full problem.

Being the fluid incompressible and given the perfect adherence conditions on the solid boundaries, one may imagine that the only production of vorticity may happen only on these boundaries on which the velocity of the fluid must be zero. To enforce the no slip boundary condition it is possible to introduce, right after the advective step, a vortex sheet on the body surface with circulation density equal to the tangential velocity of the fluid on the body contour.

The introduction of this vortex sheet means the creation of a set of vortices on the solid boundaries with given circulation such to modify the velocity field in order to re-enforce the no-slip boundary condition.

Details on the generation of vortices on solid boundaries and on the enforcement of the no slip boundary conditions will be given in sections 4.5.

Part II

DVH AND SPH SCHEME DETEAILS

4 DVH SCHEME DETAILS

In this section a detailed description of the DVH method will be given. As already said in section 3.2, the DVH method makes use of the operator splitting scheme (Chorin 1973, Chorin 1978) to account for the advection and the diffusion of the vorticity field. According to this scheme the advection and the diffusion are accounted for, for each time step, separately. The numerical solution is obtained by solving an inviscid advective step governed by the Euler equation

$$\frac{\partial \omega}{\partial t} + \mathbf{u} \cdot \nabla \omega = 0$$

followed by a purely diffusive one governed by the heat equation

$$\frac{\partial \omega}{\partial t} = \nu \Delta \omega.$$

The vorticity field is discretized into particles (see section 4.1 for the details about the discretization) and the evolution of the vorticity field is then computed by the advection and the diffusion of these particles.

Section 4.2 contains the details of the evaluation of the velocity field. To speed up the evaluation of the velocity of the vortex particles a Fast Multiple Method is used (see section 4.4 for details).

If are present solid boundaries within the fluid domain a procedure to enforce the no-slip boundary condition on these boundaries must be introduced, the details of this procedure are given in section 4.5.

Section 4.6 contains the details about the diffusion process giving particular attention to both diffusion in free space and in presence of solid boundaries.

Because the operator splitting scheme introduce two different steps to account for the advection and the diffusion of the vorticity field, the numerical method is governed by two different time steps: an advectice time step Δt_a and a diffusive one Δt_d. The details and the relations between Δt_a and Δt_d will be given in section 4.7.

4.1 VORTEX PARTICLE DISCRETIZATION AND DESINGULARIZED KERNELS

In the framework of vortex method the vorticity field ω should be considered a measure, i.e.

$$\omega_t(f) = \int f(\mathbf{r})\omega(d\mathbf{r}, t) \tag{4.1}$$

where f is a regular test function. In this case discretizing the vorticity field into point vortices means to use the following approximation for ω

$$\omega_t(f) = \sum_{i=1}^{N_v} \int f(\mathbf{r})\, \Gamma_i\, \delta_{\mathbf{r}_i(t)}(d\mathbf{r})\,, \tag{4.2}$$

where N_v is the total number of point vortices. Each is characterized by its circulation Γ_i and position $\mathbf{r}_i(t)$. $\delta_{\mathbf{r}_i(t)}(dx)$ is the two dimensional Dirac delta measure

$$\int f(\mathbf{r})\delta_{\mathbf{r}_0}(d\mathbf{r}) = f(\mathbf{r}_0)\,. \tag{4.3}$$

As proposed by Chorin (1973) the Dirac delta distribution in (4.2) can be substituted whit a mollifier function $W_\epsilon(|\mathbf{r}|)$

$$\omega_\epsilon(\mathbf{r}, t) \;=\; \sum_{i=1}^{N} \Gamma_i(t) W_\epsilon(|\mathbf{r} - \mathbf{r}_i(t)|) \tag{4.4}$$

with the following properties (see e.g. Majda and Beale (1982)):

- $W_\epsilon(z) = \epsilon^{-2} W(z/\epsilon)$;
- $W(z) \in C^2(\mathbb{R}^2)$;
- $\int W(z)dz = 1$ and $\int W(z) z^\lambda dz = 0$, where λ is any multi-index such that $1 \leqslant \lambda \leqslant p-1$, i.e. all the moments $W(z)$ must be zero to an order of $p-1$ with p integer greater than one;
- if L is a positive number and β is a multi-index, than the Fourier transform of $W(z)$ satisfies

$$\sup_{z \notin \mathbb{R}^2} |D_z^\beta \hat{W}(z)| \leqslant C_\beta (1 + |z|)^{-(L+\beta)}$$

The function $W = W(z)$ with $z = |\mathbf{r}|$ can be taken of various form: Beale and Majda (1985) suggest the use of functions of the form

$$W(z) = P(z) e^{-z^2} \tag{4.5}$$

where $P(z)$ is a polynomial containing only the even powers of z, while Rosenhead and Rosenhead (1963) suggests the use for $W(z)$ of rational functions

containing only even powers of z. This last choice is the one that will be used in the present work. Following Ranucci (1995) we will use for W the following rational function

$$W(z) = \frac{2(2-z^2)}{\pi(1+z^2)^4}. \tag{4.6}$$

Note that using expression (4.4) is equivalent to
Using this expression, the Biot-Savart law become

$$\begin{aligned}
\mathbf{u}(\mathbf{r},t) &= \int \mathbf{K}(\mathbf{r},\mathbf{r}')\omega_\epsilon(\mathbf{r}',t)d\mathbf{r}' = \\
&= \sum_{i=1}^{N} \Gamma_i(t) \int \mathbf{K}(\mathbf{r},\mathbf{r}')W_\epsilon(\mathbf{r}'-\mathbf{r}_i)d\mathbf{r}' = \\
&= \sum_{i=1}^{N} \Gamma_i(t) \iint \mathbf{K}(\mathbf{r},\mathbf{r}')W_\epsilon(\mathbf{r}'-\mathbf{r}'')\delta_{\mathbf{r}_i}(d\mathbf{r}'')d\mathbf{r}' = \\
&= \int K_\epsilon(\mathbf{r},\mathbf{r}'')\omega(d\mathbf{r}'',t)
\end{aligned} \tag{4.7}$$

where the desingularized kernel K_ϵ is the convolution of the kernel K whit the mollifier function W_ϵ

$$K_\epsilon(\mathbf{r},\mathbf{r}') = \int K(\mathbf{r},\mathbf{r}'')W_\epsilon(\mathbf{r}''-\mathbf{r}')d\mathbf{r}'' \tag{4.8}$$

and $\omega(d\mathbf{r},t)$ is the distribution of vorticity as deifined in (**??**).

The function $W(z)$ will then be used to evaluate $\mathbf{K}_\epsilon$, G_ϵ and ψ_ϵ, the desingularized version of the kernel $\mathbf{K}$, the Green function G and the stream function ψ respectively.

To evaluate the functions $\mathbf{K}_\epsilon$, ψ_ϵ and G_ϵ it is possible to solve the following Poisson equation

$$\Delta\psi_\epsilon(\mathbf{r}) = W_\epsilon(|\mathbf{r}|) \tag{4.9}$$

with

$$W_\epsilon(z) = \frac{2\epsilon^4(2\epsilon^2-z^2)}{\pi(\epsilon^2+z^2)^4}. \tag{4.10}$$

The expression for K_ϵ is easily obtained by writing eq. (4.9) in polar coordinates and integrating it

$$K_\epsilon(\mathbf{r}) = -\frac{\mathbf{r}^\perp}{2\pi}\left[\frac{|\mathbf{r}|^4+3\epsilon^2|\mathbf{r}|^2+4\epsilon^4}{(\epsilon^2+|\mathbf{r}|^2)^3}\right]. \tag{4.11}$$

Another integration lead to the stream function ψ_ϵ

$$\psi_\epsilon(\mathbf{r}) = \frac{1}{4\pi}\left[\frac{2|\mathbf{r}|^4+3\epsilon^2|\mathbf{r}|^2}{(\epsilon^2+|\mathbf{r}|^2)^2} + \log\left(1+\frac{|\mathbf{r}|^2}{\epsilon^2}\right)\right] + \frac{1}{2\pi}(1-\log\epsilon). \tag{4.12}$$

The Green function G_ϵ is recovered from the following convolution integral

$$G_\epsilon(\mathbf{r}, \mathbf{r}') = \int G(\mathbf{r}, \mathbf{r}'') W_\epsilon(\mathbf{r}'' - \mathbf{r}') d\mathbf{r}'' \tag{4.13}$$

from which we have that

$$G_\epsilon(\mathbf{r}) = -\psi_\epsilon(\mathbf{r}). \tag{4.14}$$

4.2 VELOCITY FIELD EVALUATION

During the advective step the fluid is considered inviscid and the evolution of the vorticity field is governed by the Euler equation

$$\frac{\partial \omega}{\partial t} + \mathbf{u} \cdot \nabla \omega = 0.$$

The velocity field can be written as a sum of three fundamental contributions

$$\mathbf{u} = \mathbf{u}_\infty + \mathbf{u}_\omega + \mathbf{u}' \tag{4.15}$$

where $\mathbf{u}_\infty$ is the free stream velocity, $\mathbf{u}_\omega$ is the velocity contribution due to the vorticity field itself and, finally, $\mathbf{u}'$ is the velocity field contribution which allows for the enforcement of the boundary condition on the solid surfaces.

In this section two ways to evaluate the velocity field will be presented: in section 4.2.1 the direct integral representation of the velocity field is described while section 4.2.2 deals with the indirect integral representation, the latter being the one used in the DVH scheme.

4.2.1 Direct integral representation of the velocity field

One way to evaluate a solenoidal and rotational velocity field is to use (see e.g. Bassanini et al. (1991) and Di Salvo (1996)) the Poincarè integral representation:

$$\begin{aligned} \mathbf{u}(\mathbf{r}) - \mathbf{u}_\infty \;=\; & -\; \nabla \int_{\partial\Omega_b} (\mathbf{u}(\mathbf{r}^\star) - \mathbf{u}_\infty) \cdot \mathbf{n}(\mathbf{r}^\star) G(\mathbf{r}, \mathbf{r}^\star) d\mathbf{r}^\star + \\ & +\; \nabla \times \int_{\partial\Omega_b} \mathbf{n}(\mathbf{r}^\star) \times (\mathbf{u}(\mathbf{r}^\star) - \mathbf{u}_\infty) G(\mathbf{r}, \mathbf{r}^\star) d\mathbf{r}^\star + \\ & -\; \nabla \times \int_\Omega \omega(\mathbf{r}^\star) \mathbf{e}_z G(\mathbf{r}, \mathbf{r}^\star) d\mathbf{r}^\star. \end{aligned} \tag{4.16}$$

where $\mathbf{r} \in \Omega$, $\mathbf{n}$ is the outgoing unit normal vector from the fluid, $\partial\Omega_b$ is boundary of the body and $G(\mathbf{r}, \mathbf{r}^\star)$ is the Green function for a fluid whose domain $\Omega = \mathbb{R}^2$:

$$G(\mathbf{r}, \mathbf{r}^\star) = \frac{1}{2\pi} \ln |\mathbf{r} - \mathbf{r}^\star|. \tag{4.17}$$

Noting that

$$\mathbf{n}(\mathbf{r}) \times (\mathbf{u}(\mathbf{r}) - \mathbf{u}_\infty) = -(\mathbf{u}(\mathbf{r}) - \mathbf{u}_\infty) \cdot \tau(\mathbf{r}) \mathbf{e}_z$$

and calling $u_\tau = (\mathbf{u} - \mathbf{u}_\infty) \cdot \tau$ and $u_n = (\mathbf{u} - \mathbf{u}_\infty) \cdot \mathbf{n}$ (being τ the tangent unit vector to the body contour), eq. (4.16) become

$$\begin{aligned} \mathbf{u}(\mathbf{r}) - \mathbf{u}_\infty \quad = \quad & \int_{\partial\Omega_b} u_n(\mathbf{r}^\star) \nabla G(\mathbf{r}, \mathbf{r}^\star) d\mathbf{r}^\star + \\ - \quad & \int_{\partial\Omega_b} u_\tau(\mathbf{r}^\star) \nabla \times \mathbf{e}_z G(\mathbf{r}, \mathbf{r}^\star) d\mathbf{r}^\star + \\ - \quad & \int_{\Omega} \omega(\mathbf{r}^\star) \nabla \times \mathbf{e}_z G(\mathbf{r}, \mathbf{r}^\star) d\mathbf{r}^\star. \end{aligned} \tag{4.18}$$

Noting that in a 2D framework

$$\nabla \times \mathbf{e}_z G = -\nabla^\perp G \tag{4.19}$$

equation (4.18) can be written as:

$$\begin{aligned} \mathbf{u}(\mathbf{r}) - \mathbf{u}_\infty \quad = \quad - \quad & \nabla \int_{\partial\Omega_b} u_n(\mathbf{r}^\star) G(\mathbf{r}, \mathbf{r}^\star) d\mathbf{r}^\star + \\ + \quad & \nabla^\perp \left[\int_{\partial\Omega_b} u_\tau(\mathbf{r}^\star) G(\mathbf{r}, \mathbf{r}^\star) d\mathbf{r}^\star + \right. \\ + \quad & \left. \int_{\Omega} \omega(\mathbf{r}^\star) G(\mathbf{r}, \mathbf{r}^\star) d\mathbf{r}^\star \right]. \end{aligned} \tag{4.20}$$

Writing the no slip boundary condition in the following way

$$(\mathbf{u} - \mathbf{u}_\infty) \cdot \mathbf{n} = -\mathbf{u}_\infty \cdot \mathbf{n} \tag{4.21}$$

it is possible to write the following relations:

$$\begin{aligned} -\nabla \int_{\partial\Omega_b} [\mathbf{u}(\mathbf{r}^\star) - \mathbf{u}_\infty] \cdot \mathbf{n} G(\mathbf{r}, \mathbf{r}^\star) d\mathbf{r}^\star \quad &= \quad \nabla \int_{\partial\Omega_b} \mathbf{u}_\infty \cdot \mathbf{n}(\mathbf{r}^\star) G(\mathbf{r}, \mathbf{r}^\star) d\mathbf{r}^\star = \\ &= \quad \nabla^\perp \int_{\partial\Omega_b} \mathbf{u}_\infty \cdot \tau(\mathbf{r}^\star) G(\mathbf{r}, \mathbf{r}^\star) d\mathbf{r}^\star. \end{aligned} \tag{4.22}$$

Using eq. (4.22), eq. (4.20) become

$$\mathbf{u}(\mathbf{r}) - \mathbf{u}_\infty = \nabla^\perp \left[\int_{\partial\Omega_b} \mathbf{u}(\mathbf{r}^\star) \cdot \tau(\mathbf{r}^\star) G(\mathbf{r}, \mathbf{r}^\star) d\mathbf{r}^\star + \int_{\Omega} \omega(\mathbf{r}^\star) G(\mathbf{r}, \mathbf{r}^\star) d\mathbf{r}^\star \right]. \tag{4.23}$$

The skew gradient of the Green function G can be written in terms of the tangent and normal derivatives along the body contour

$$\nabla^{\perp} G = \frac{\partial G}{\partial \tau}\mathbf{n} - \frac{\partial G}{\partial n}\tau. \tag{4.24}$$

Using eq. (4.24), eq.(4.23) become

$$\begin{aligned}\mathbf{u}(\mathbf{r}) - \mathbf{u}_\infty \quad = \quad & \int_{\partial\Omega_b} [\mathbf{u}(\mathbf{r}^\star)\cdot\tau(\mathbf{r}^\star)]\frac{\partial G}{\partial \tau}(\mathbf{r},\mathbf{r}^\star)\mathbf{n}(\mathbf{r}^\star)\,d\mathbf{r}^\star + \\ & - \int_{\partial\Omega_b} [\mathbf{u}(\mathbf{r}^\star)\cdot\tau(\mathbf{r}^\star)]\frac{\partial G}{\partial n}(\mathbf{r},\mathbf{r}^\star)\tau(\mathbf{r}^\star)\,d\mathbf{r}^\star + \\ & + \int_{\Omega} \omega(\mathbf{r}^\star)\frac{\partial G}{\partial n}(\mathbf{r},\mathbf{r}^\star)\tau(\mathbf{r}^\star)\,d\mathbf{r}^\star\end{aligned} \tag{4.25}$$

obtaining the expression of the velocity field for every point $\mathbf{r} \in \Omega$.

The velocity field of eq. (4.25) only satisfy the free slip boundary condition introduced in (4.21). To enforce the no-slip boundary condition a vortex sheet concentrated on $\partial\Omega_b$ must be introduced in order to have $\mathbf{u}\cdot\tau = 0$ on $\partial\Omega_b$.

It is possible to write an equation for $\mathbf{u}\cdot\tau$ on $\partial\Omega_b$ taking the limit for $\mathbf{r} \to \mathbf{r}'$ with $\mathbf{r}' \in \partial\Omega$ in eq. (4.25) and taking the projection on the tangent direction to the body

$$\begin{aligned}\left[\mathbf{u}(\mathbf{r}') - \mathbf{u}_\infty\right]\cdot\tau(\mathbf{r}') \quad = \quad & \left(-\lim_{\mathbf{r}\to\mathbf{r}'}\int_{\partial\Omega_b} \mathbf{u}(\mathbf{r}^\star)\cdot\tau(\mathbf{r}^\star)\frac{\partial G}{\partial n}(\mathbf{r},\mathbf{r}^\star)\,d\mathbf{r}^\star\right) + \\ & - \int_{\Omega} \omega(\mathbf{r}^\star)\frac{\partial G}{\partial n}(\mathbf{r}',\mathbf{r}^\star)\,d\mathbf{r}^\star.\end{aligned} \tag{4.26}$$

The first term in the previous equation needs particular attentions. Writing explicitly the derivatives along the normal direction of the Green function

$$\frac{\partial G}{\partial n}(\mathbf{r},\mathbf{r}^\star) = \frac{1}{2\pi}\frac{(\mathbf{r}-\mathbf{r}^\star)\cdot\mathbf{n}}{|\mathbf{r}-\mathbf{r}^\star|^2}, \quad \mathbf{r}^\star \in \partial\Omega \tag{4.27}$$

it is straightforward to note that in the limit for $\mathbf{r} \to \mathbf{r}'$ with $\mathbf{r}' \in \partial\Omega$ this term may become singular.

To avoid this problem the following relation for a closed domain can be proved:

$$\begin{aligned}\lim_{\mathbf{r}'\to\mathbf{r}}\int_{\partial\Omega} \mathbf{u}(\mathbf{r}^\star)\cdot\tau(\mathbf{r}^\star)\frac{\partial G}{\partial n}(\mathbf{r}',\mathbf{r}^\star)\,d\mathbf{r}^\star = \quad & -\frac{1}{2}\mathbf{u}(\mathbf{r}')\cdot\tau(\mathbf{r}') + \\ & + \fint_{\partial\Omega} \mathbf{u}(\mathbf{r}^\star)\cdot\tau(\mathbf{r}^\star)\frac{\partial G}{\partial n}(\mathbf{r}',\mathbf{r}^\star)\,d\mathbf{r}^\star\end{aligned} \tag{4.28}$$

where $⨍$ is the principal value of the integral.

Using expression (4.28), equation (4.26) become

$$\begin{aligned}\left[\mathbf{u}(\mathbf{r}') - \mathbf{u}_\infty\right] \cdot \tau(\mathbf{r}') = \; & - \; ⨍_{\partial\Omega} \mathbf{u}(\mathbf{r}^\star) \cdot \tau(\mathbf{r}^\star) \frac{\partial G}{\partial n}(\mathbf{r}', \mathbf{r}^\star) d\mathbf{r}^\star + \\ & - \; \int_\Omega \omega(\mathbf{r}^\star) \frac{\partial G}{\partial n}(\mathbf{r}', \mathbf{r}^\star) d\mathbf{r}^\star + \\ & + \; \frac{1}{2}\mathbf{u}(\mathbf{r}') \cdot \tau(\mathbf{r}').\end{aligned} \tag{4.29}$$

Thus the Fredholm integral equation of the second kind has been found

$$\frac{1}{2}\mathbf{u}(\mathbf{r}') \cdot \tau(\mathbf{r}') + ⨍_{\partial\Omega} \mathbf{u}(\mathbf{r}^\star) \cdot \tau(\mathbf{r}^\star) \frac{\partial G}{\partial n}(\mathbf{r}', \mathbf{r}^\star) d\mathbf{r}^\star = \mathbf{u}_\infty(\mathbf{r}') \cdot \tau(\mathbf{r}') - \mathbf{u}_\omega(\mathbf{r}') \cdot \tau(\mathbf{r}') \tag{4.30}$$

where $\mathbf{r}' \in \partial\Omega$ and

$$\mathbf{u}_\omega(\mathbf{r}) = \int \omega(\mathbf{r}^\star) \mathbf{K}(\mathbf{r}^\star, \mathbf{r}) d\mathbf{r}^\star. \tag{4.31}$$

In equation (4.31) the kernel $\mathbf{K}$ is given by

$$\mathbf{K}(\mathbf{r}^\star, \mathbf{r}) = \nabla^\perp G(\mathbf{r}^\star, \mathbf{r}) \tag{4.32}$$

where G is defined in eq. (4.17).

Knowing the right hand side of eq. (4.30) one must discretize the principal value integral and the whole equation on the points of the body surface to obtain a a system of N_{body} equations that in matricial form has the following expression

$$[A]\{u_\tau\} = \{u_{\infty\tau}\} + \{u_{\omega\tau}\}. \tag{4.33}$$

The solution of this system of equations gives the values of the tangential velocity on the body points that can be used to generate a vortex sheet on the body itself so to modify the velocity field in such a way to enforce the no slip boundary condition, in particular it is possible to generate a set of vortices on the body points each with circulation given by

$$\Gamma_i = u_\tau(\mathbf{r}_i)\Delta s, \; i = 1, ..., N_{body} \tag{4.34}$$

where Δs is the body discretization.

It is possible to prove that (4.33), in case of multiply connected domains, has as many eigensolutions as the number of holes in the domain Ω, meaning that the matrix A is a singular and that Singular Value Decomposition techniques see e.g. Press (2007)) are needed to solve (4.33).

Due to the high computational cost of these techniques we will use an indirect integral representation of the velocity field that will be described in the next section.

4.2.2 Indirect integral representation of the velocity field

Using an indirect integral representation, the velocity field can be written as

$$\begin{aligned}\mathbf{u}(\mathbf{r}) - \mathbf{u}_\infty = &- \int_{\partial\Omega_b} \sigma(\mathbf{r}^\star)\mathbf{K}^\perp(\mathbf{r},\mathbf{r}^\star)\,d\mathbf{r}^\star + \\ &+ \int_{\partial\Omega_b} \gamma(\mathbf{r}^\star)\,\mathbf{K}(\mathbf{r},\mathbf{r}^\star)\,d\mathbf{r}^\star + \\ &+ \mathbf{u}_\omega(\mathbf{r})\end{aligned} \tag{4.35}$$

where the body contribution to the velocity field is described in terms of sources $\sigma(\mathbf{r})$ and circulation $\gamma(\mathbf{r})$ distributions and $\mathbf{r} \in \Omega \cup \partial\Omega$. Also in this case the integral kernel $\mathbf{K}$ is given by

$$\mathbf{K}(\mathbf{r}^\star,\mathbf{r}) = \nabla^\perp G(\mathbf{r}^\star,\mathbf{r}); \quad G(\mathbf{r}^\star,\mathbf{r}) = \frac{1}{2\pi}\ln|\mathbf{r}^\star,\mathbf{r}|. \tag{4.36}$$

Consider now only the contributions to the velocity field due to the presence of a body

$$\mathbf{u}'(\mathbf{r}) = -\int_{\partial\Omega_b} \sigma(\mathbf{r}^\star)\mathbf{K}^\perp(\mathbf{r},\mathbf{r}^\star)\,d\mathbf{r}^\star + \int_{\partial\Omega_b} \gamma(\mathbf{r}^\star)\,\mathbf{K}(\mathbf{r},\mathbf{r}^\star)\,d\mathbf{r}^\star\,, \tag{4.37}$$

it is useful to introduce a complex formulation of eq. (4.37) that will be used in section 4.5 to enforce the no slip boundary condition.

Calling $q(z)$ the complex velocity field

$$q(z) := u_x(x,y) - iu_y(x,y)\,, \tag{4.38}$$

where u_x and u_y are the two velocity components of the vector $\mathbf{u}$, equation (4.37) can be written as

$$q'(z) = \frac{1}{2\pi i}\int_{\partial\Omega_b} \frac{i\sigma(z^\star)+\gamma(z^\star)}{\tau(z^\star)}\frac{dz^\star}{z-z^\star},\ \forall z \in \Omega. \tag{4.39}$$

where $\tau = \tau_x + i\tau_y$ is the complex tangent to the body contour.

Consider now the integral singular kernel

$$\mathcal{K}(z,z^\star) = \frac{1}{z-z^\star}, \tag{4.40}$$

it is straightforward to note that eq. (4.39) become singular when $z^\star \in \partial\Omega_b$ and $z \to z^\star$. Using Plemelji formulas (Landrini (1993)) it is possible to obtain an expression of eq. (4.39) when $z \in \partial\Omega_b$:

$$q'(z) = \frac{i\sigma(z)+\gamma(z)}{2\tau} + \frac{1}{2\pi i}\int_{\partial\Omega_b} \frac{i\sigma(z^\star)+\gamma(z^\star)}{\tau(z^\star)}\frac{dz^\star}{z-z^\star},\ \forall z \in \partial\Omega_b. \tag{4.41}$$

Thus the representation of eq. (4.37) in complex notation is given by

$$\begin{cases} f(z) & := & \dfrac{i\sigma(z)+\gamma(z)}{\tau(z)}, \qquad \mathcal{K}(z,z^\star) := \dfrac{1}{z-z^\star} & \\ q'(z) & = & \dfrac{1}{2\pi i}\displaystyle\int_{\partial\Omega_b} f(z^\star)\,\mathcal{K}(z,z^\star)dz^\star, & \forall\, z\in\Omega \\ q'(z) & = & \dfrac{1}{2}f(z) + \dfrac{1}{2\pi i}\fint_{\partial\Omega_b} f(z^\star)\,\mathcal{K}(z,z^\star)dz^\star, & \forall\, z\in\partial\Omega_b \end{cases} \tag{4.42}$$

It is easy to obtain a solution of (4.42) if the distributions of σ and γ on the body contour are known. The way to evaluate σ and γ, together with the enforcement of the no slip boundary condition will be presented in the next section 4.5

4.3 DISCRETE VELOCITY FIELD AND PARTICLE ADVECTION

The use of the indirect integral representation (4.35) has a great advantage, the possibility to discretize the velocity field induced by the vorticity distribution and by the presence of the body in a similar way.

In fact being N_{vortex} the number of vortices in the fluid domain, the velocity field induced by the discrete distribution of vorticity (**??**)

$$\omega(\mathbf{r},t) = \sum_{i=1}^{N_{vortex}} \Gamma_i(t)\delta_\epsilon(\mathbf{r},\mathbf{r}_i) \tag{4.43}$$

is given by

$$\mathbf{u}_\omega(\mathbf{r},t) = \sum_{i=1}^{N_{vortex}} \Gamma_i(t)\mathbf{K}_\epsilon(\mathbf{r},\mathbf{r}_i). \tag{4.44}$$

If the body boundary is discretized into N_{body} points with uniform spacing Δs, equation (4.42) can be written in the following discrete form:

$$\mathbf{u}'(\mathbf{r},t) = \sum_{k=1}^{N_{body}} \left[\mathbf{K}_\epsilon(\mathbf{r},\mathbf{r}_k)\gamma_k(t) - \mathbf{e}_3\times\mathbf{K}_\epsilon(\mathbf{r},\mathbf{r}_k)\,\sigma_k(t)\right]\Delta s \tag{4.45}$$

where $\mathbf{r}_k$ is the position of the k-th generic body element and σ_k and γ_k are the distribution of sorgents and circulations respectively, discretized on the body contour.

Using equations (4.44) and (4.45) into eq. (4.15) it is possible to write an expression for the velocity of each vortex particle in the following way

$$\begin{cases} \mathbf{u}(\mathbf{r}_i,t) = \mathbf{u}_\infty + \sum_{j=1}^{N_{vortex}} \Gamma_j(t)\mathbf{K}_\epsilon(\mathbf{r}_i,\mathbf{r}_j) + \\ \qquad\qquad + \sum_{k=1}^{N_{body}} \left[\mathbf{K}_\epsilon(\mathbf{r}_i,\mathbf{r}_k)\gamma_k(t) - \mathbf{e}_3 \times \mathbf{K}_\epsilon(\mathbf{r}_i,\mathbf{r}_k)\,\sigma_k(t)\right]\Delta s \\ \dfrac{D\mathbf{r}_i(t)}{Dt} = \mathbf{u}(\mathbf{r}_i,t) \\ \dfrac{D\Gamma_i(t)}{Dt} = 0. \end{cases} \tag{4.46}$$

After evaluating the velocity of each vortex using the first equation of system (4.46), the vortices are displaced according to the second equation using a fourth order Runge-Kutta algorithm using a specific time step, Δt_a, for all the vortex particles (see section 4.7). Finally each vortex carries its own circulation during the advective step.

The direct use of the first equation of system (4.46) would lead to a computation count of order N^2_{vortex}. To decrease the computational cost of the evaluation of the velocity field a Fast Multipole Method is adopted (see section 4.4).

4.4 FAST MULTIPOLE METHOD

Consider now only the first equation of system (4.46)

$$\begin{aligned} \mathbf{u}(\mathbf{r}_i,t) = \mathbf{u}_\infty &+ \sum_{j=1}^{N_v} \Gamma_j(t)\,\mathbf{K}_\epsilon(\mathbf{r}_i,\mathbf{r}_j) + \\ &+ \sum_{k=1}^{N_b} \mathbf{K}_\epsilon(\mathbf{r}_i,\mathbf{r}_k)\,\gamma_k(t)\Delta s + \\ &- \sum_{k=1}^{N_b} \mathbf{e}_3 \times \mathbf{K}_\epsilon(\mathbf{r}_i,\mathbf{r}_k)\,\sigma_k(t)\,\Delta s \end{aligned} \tag{4.47}$$

it is easy to see that increasing the number of vortices and adopting finer discretizations for the description of the body contour, the evaluation of the velocity field can reach a computation count of order N^2_{vortex} operations for

the velocity field induced by the vorticity distribution and of order $N_{vortex} \times N_{body}$ in case of the velocity field induced by the presence of a solid body.

Due to these high computational cost various method to speed up the evaluation of the velocity field have been developed by many researchers. In the present work a Fast Multipole Method, originally proposed by Appel (1985) and Barnes and Hut (1986), will be used, in particular the method introduced by Ranucci (1995) will be followed.

In Ranucci (1995) the computational domain is recursively divided into panels each containing at mos a fixed number of vortices N_{max}. Using an oct-tree structure it is possible to find for each panel its nearest neighbours.

Starting from the panels at the lowest level (highest number of subdivision), the velocity of each vortex is evaluated using the Biot-Savart law to account for the interactions with the vortices in the present panel and in its neighborhood, while the contributions of the vortices contained in panels outside the neighborhood of the selected panel are approximated using a multipole expansion. Details about the domain subdivision and the construction of the tree structure are given in section 4.4.1, while details about the multipole expansion will be given in section 4.4.2.

4.4.1 Tree-code structure

Given a distribution of N_{vortex} vortices, it can be arranged in an oct-tree structure by subdividing the domain into panels and linking each vortex to the appropriate panels. An example of recursive subdivision of the computational domain is given in Fig. 4.1.

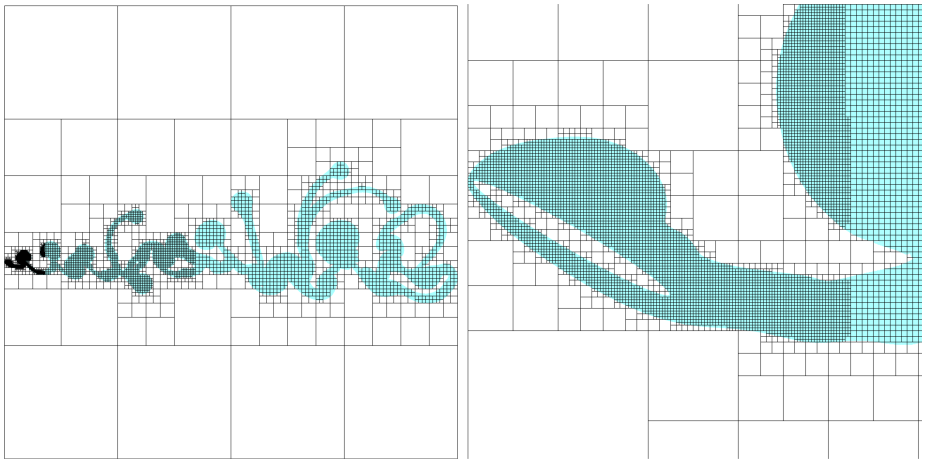

Figure 4.1: Example of recursive subdivision of the computational domain. Left: domain subdivision at the end of the simulation of an impulsively started inclined elliptic cylinder at $Re = 3000$. Right: Zoom on the computational domain near the body

To recursively divide the domain two parameters must be fixed: the maximum number of vortices contained in each panel N_{max} and the maximum number of subdivision L_{max} that each panel can undergo. Typical numbers for the maximum number of vortices and subdivisions used in the simulations presented in this work are $N_{max} = 200$ and $L_{max} = 15$.

The computational domain is defined by circumscribing the vortices with a square box with size is given by the maximum distance between the vortices themselves, then this box is divided into four panels and the information about the vortices contained in each panel are stored. Then each panel, starting from the upper left, is recursively divided into four new panels, if the number of vortices is greater than a fixed threshold N_{max}. The subdivision process ends when the number of vortices in each panel is lower than N_{max} or the maximum number of subdivision is reached. An example of subdivision in three levels with the corresponding numeration of each panel is given in figure 4.2.

4.4.2 Multipole expansion of the velocity field

Consider now for simplicity only the velocity induced by the rotational part of the fluid

$$\mathbf{u}_\omega(\mathbf{r}_i, t) = \sum_{j=1}^{N_v} \Gamma_j(t)\, \mathbf{K}_\epsilon(\mathbf{r}_i, \mathbf{r}_j) \tag{4.48}$$

consideration and results that will be obtained for $\mathbf{u}_\omega$ are easily extendable to the velocity field induced by the presence of the body.

Consider the computational domain divided into N_p panels, then the velocity field of a vortex with position $\mathbf{r}_i$ can be written as

$$\mathbf{u}_\omega(\mathbf{r}_i, t) = \sum_{k=1}^{N_p} \sum_{j=1}^{N_k} \Gamma_j(t)\, \mathbf{K}_\epsilon(\mathbf{r}_i, \mathbf{r}_j) \tag{4.49}$$

where N_k are the number of vortices contained in each of the N_p panels.

Using the tree structure described in the previous section it is possible to define a neighborhood of the considered panel as the nearest panels with the same order of subdivision as shown in figure 4.3.

The vortices in the neighboring panels shown in figure 4.3 gives contribution to the velocity of the vortex under consideration through the Biot-Savart law.

The vortices contained in all the other panels gives approximated contribution to the velocity of the considered vortex through a multipole expansion, i.e.

$$\mathbf{u}_\omega(\mathbf{r}_i, t) = \sum_{k=1}^{n} \sum_{j=1}^{N_k} \Gamma_j(t)\, \mathbf{K}_\epsilon(\mathbf{r}_i, \mathbf{r}_j) + \mathit{multipole\ expansion} \tag{4.50}$$

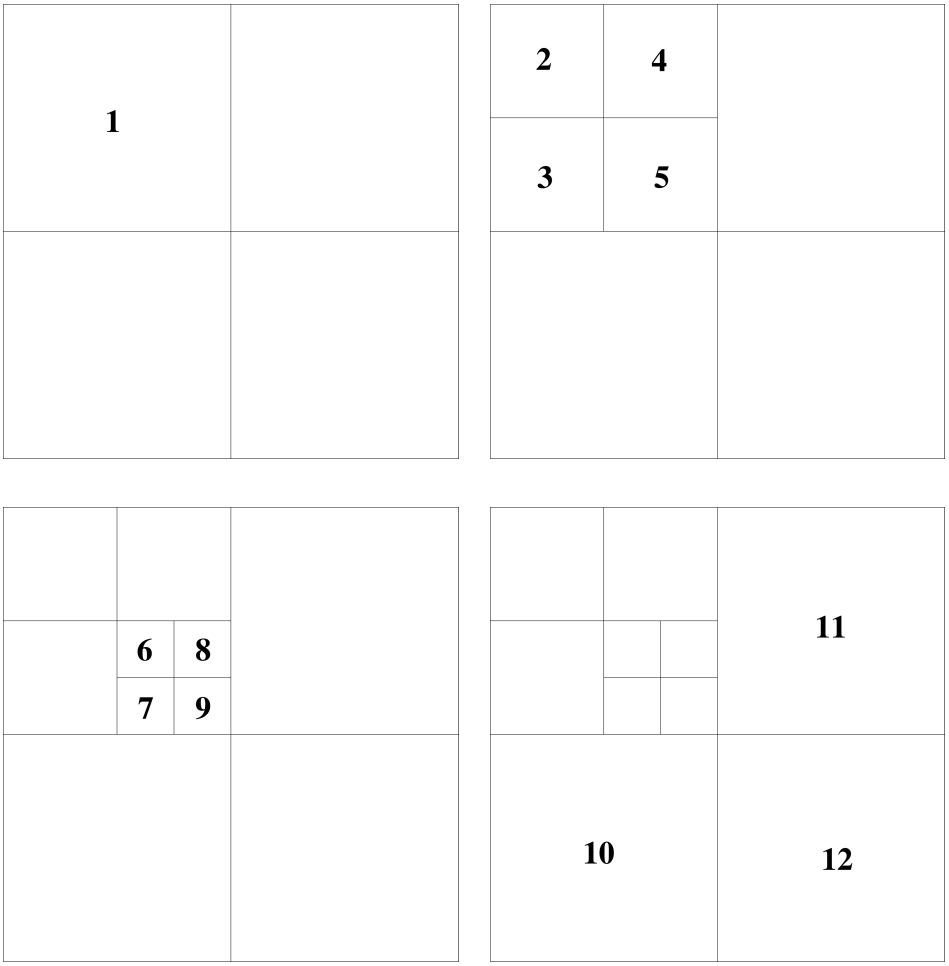

Figure 4.2: Example of domain subdiviosion in three levels

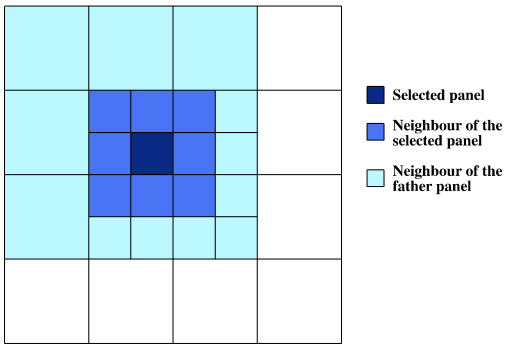

Figure 4.3: Definition of the neighborhood of a panel and of its father panel.

where n is the number of panels over which the direct summation can be done. To reduce the CPU cost it is possible to evaluate the multipole expansion only for those panels not contained in the neighborhood of the selected one but contained in the neighborhood of the father panel.

Consider now the set of vortices contained in a single panel, the velocity induced by these vortices can be written in complex variables in the following way

$$q_\omega(z) = \frac{1}{2\pi i}\sum_{j=1}^{N}\frac{\Gamma_i}{z-z_j}. \tag{4.51}$$

It is now possible to inscribe the vortices contained in the selected panel in a circle of radius R and center the center of the panel z_0, allowing to write expression (4.51) in the following form

$$q_\omega(z) = \frac{i}{2\pi(z-z_0)}\sum_{j=1}^{N_v}\frac{\Gamma_j}{1-\frac{z_j-z_0}{z-z_0}}. \tag{4.52}$$

Remembering that the geometric series $\sum_{k=1}^{\infty} p^k$ is absolutely convergent if $|p|<1$ and that the following relation holds

$$\sum_{k=1}^{\infty} p^k = \frac{1}{1-p}, \tag{4.53}$$

the velocity $q_\omega(z)$ can be written using a Laurent series expansion in the following way

$$q_\omega(z) = \sum_{k=1}^{\infty}\frac{C_k}{(z-z_0)^k}; \quad C_k = -\frac{1}{2\pi i}\sum_{j=1}^{N_v}\Gamma_j(z_j-z_0)^{k-1}. \tag{4.54}$$

From eq. (4.54) it is possible to obtain an approximated solution of the velocity field induced by the vorticity distribution considering only the first K_{max} terms of the Laurent series

$$q_\omega(z) = \sum_{k=1}^{K_{max}}\frac{C_k}{(z-z_0)^k}, \tag{4.55}$$

detail about the errors made using this approximation can be found in Ranucci (1995).

Note that if $K_{max}=1$ the velocity has the following expression

$$q_\omega(z) = \frac{C_1}{(z-z_0)}, \quad C_1 = -\frac{1}{2\pi i}\sum_{j=1}^{N_v}\Gamma_j. \tag{4.56}$$

meaning that the distribution of vorticity ω has been replaced by a single vortex with complex position z_0 and circulation $\sum_{j=1}^{N_v} \Gamma_j$. Thus the number K_{max} must be finite and greater than one in order to guarantee a good approximation of the velocity field. A typical value for the number of coefficients of the Laurent series used in the present work is $K_{max} = 20$.

Given a vorticity distribution, each vortex is contained in a number of panels equal to the maximum number of subdivision reached. Consider for example a vortex contained in panel 9 of Figure 4.2 it is also contained in panels 5 and 1, each of these panels containing a different number of vortices N_9, N_5 and N_1. In this case to evaluate the coefficients C_k^1, C_k^5 and C_k^9 using eq. (4.54), the k-th momentum of the selected vortex must be computed with respect to the center of the three panels, possibly limiting the efficiency of the algorithm.

One way to speed up this procedure is given by the possibility to evaluate the coefficients of the Laurent series of a father panel using the coefficients of the son panels.

Thus consider a panel of level l divided into four son panels of level $l+1$. If the father panels has center z_0 it is possible to use the Taylor series expansion in eq. (4.54) around a point $\hat{z} \neq z_0$

$$q(z) = \sum_{m=0}^{\infty} \frac{1}{l!} \left(\frac{\partial}{\partial z_0} \right)^l q(z, \hat{z})(z_0 - \hat{z})^l \tag{4.57}$$

obtaining the following expression

$$\begin{aligned} q(z) &= \sum_{m=1}^{\infty} \sum_{k=1}^{\infty} \frac{(z_0 - \hat{z})^{m-k}}{(z_0 - \hat{z})^m} \frac{k(k+1)(k+2)...(k+l-1)}{l!} C_k \\ &= \sum_{m=1}^{\infty} \sum_{k=1}^{m} \frac{(z_0 - \hat{z})^{m-k}}{(z_0 - \hat{z})^m} \begin{pmatrix} m-1 \\ \\ k-1 \end{pmatrix} C_k \end{aligned} \tag{4.58}$$

where $m = k + l$, $l \geqslant 0$ and thus $k \leqslant m$.

Thus it is possible to write the following expression

$$q(z) = \sum_{m=1}^{\infty} \frac{C'_m}{(z - \hat{z})^m}, \quad C'_m = \sum_{k=1}^{m} \begin{pmatrix} m-1 \\ \\ k-1 \end{pmatrix} (z_0 - \hat{z})^{m-k} C_k \tag{4.59}$$

linking the moments of the vorticity field evaluated respect to the center z_0 to the ones evaluated using the center $\hat{z}$.

4.5 ENFORCEMENT OF THE NO SLIP BOUNDARY CONDITIONS

The velocity field evaluated during the advective step only satisfies a free slip boundary condition, violating the no slip boundary condition of the full problem.

To restore the correct boundary condition a vortex sheet is generated on the solid boundaries right after the advective step with circulation density equal to the tangential velocity on the solid boundaries. During this process the distribution of σ and γ on the boundaries are also evaluated.

The enforcement of the no-slip boundary condition can be divided into two steps: in the first step the free slip boundary condition is used to evaluate the distribution of σ while in the second step the vortex sheet is generated right after the evaluation of the tangential velocity on the body contour.

Consider now the last equation of system (4.42):

$$q'(z) = \frac{1}{2}f(z) + \frac{1}{2\pi i}\oint_{\partial\Omega_b} f(z^\star)\,\mathcal{K}(z,z^\star)dz^\star\,,\ \forall\, z \notin \partial\Omega_b \tag{4.60}$$

to obtain the integral equations for the normal and tangent component of the velocity field $\mathbf{u}$ it is sufficient to multiply this equation by the complex tangent and the take the imaginary and real part respectively

$$q\cdot\tau = u_\tau - iu_n \tag{4.61}$$

obtaining the following expression for the normal component u_n' and the tangential component u_τ'

$$u_n'(z) = -\Im\left[\frac{i\sigma(z)+\gamma(z)}{2} + \frac{\tau(z)}{2\pi i}\oint_{\partial\Omega_b}\frac{i\sigma(z^\star)+\gamma(z^\star)}{2\tau(z^\star)}\,\mathcal{K}(z,z^\star)dz^\star\right] \tag{4.62}$$

$$u_\tau'(z) = \Re\left[\frac{i\sigma(z)+\gamma(z)}{2} + \frac{\tau(z)}{2\pi i}\oint_{\partial\Omega_b}\frac{i\sigma(z^\star)+\gamma(z^\star)}{2\tau(z^\star)}\,\mathcal{K}(z,z^\star)dz^\star\right]. \tag{4.63}$$

The free slip boundary condition on $\partial\Omega_b$ can be written as

$$(\mathbf{u}_\infty + \mathbf{u}_\omega + \mathbf{u}')\cdot\mathbf{n} = \mathbf{u}_{body}\cdot\mathbf{n} \tag{4.64}$$

using (4.62) it is possible to obtain the following equation

$$\begin{aligned}&\frac{1}{2}\sigma(z) + \Im\left[\frac{\tau(z)}{2\pi i}\oint_{\partial\Omega_b}\frac{i\sigma(z^\star)}{\tau(z^\star)}\mathcal{K}(z,z^\star)dz^\star\right] = \\ &= (-\mathbf{u}_{body} + \mathbf{u}_\infty + \mathbf{u}_\omega)\cdot\mathbf{n} + \Im\left[\frac{\tau(z)}{2\pi i}\oint_{\partial\Omega_b}\frac{\gamma(z^\star)}{\tau(z^\star)}\mathcal{K}(z,z^\star)dz^\star\right].\end{aligned} \tag{4.65}$$

If the right hand side is known eq. (4.65) is an integral equation whose solution is the distribution of σ on $\partial\Omega_b$.

At this stage the distribution of circulations is also an unknown of the problem, however a constant distribution for γ can be considered and the value can be set using the Kelvin theorem:

$$\gamma(z) = \frac{\Gamma(t_0) - \Gamma(t)}{\mathcal{P}}, \ \forall z \in \partial\Omega_b \tag{4.66}$$

where $\Gamma(t_0)$ is the circulation around the body at the initial time t_0, $\Gamma(t)$ is the total circulation at time t, i.e. $\Gamma(t) = \int_\Omega \omega(\mathbf{r})d\mathbf{r}$, and $\mathcal{P}$ is the total perimeter of the body.

Knowing the σ and γ distribution it is now possible to evaluate the velocity field in every points of the fluid domain Ω but also to enforce the no slip boundary condition. However the velocity field that would be generated this way only satisfies the free slip boundary condition (4.64).

To enforce the no-slip boundary condition on $\partial\Omega_b$ the following condition must be considered

$$(\mathbf{u}_\infty + \mathbf{u}_\omega + \mathbf{u}') \cdot \tau = \mathbf{u}_{body} \cdot \tau \tag{4.67}$$

Using eq. (4.63) in (4.67) it is possible to obtain the following equation for u'_τ

$$\begin{aligned} u'_\tau = \frac{\gamma(z)}{2} \quad &+ \quad \Re\left[\frac{\tau(z)}{2\pi i}\oint_{\partial\Omega_b} \frac{i\sigma(z^\star) + \gamma(z^\star)}{2\tau(z^\star)}\mathcal{K}(z, z^\star)dz^\star\right] \\ &+ \quad (-\mathbf{u}_{body} + \mathbf{u}_\infty + \mathbf{u}_\omega) \cdot \tau. \end{aligned} \tag{4.68}$$

u'_τ can now be used to introduce a vortex sheet with total circulation

$$\Gamma = \int_{\partial\Omega_b} u'_\tau ds \tag{4.69}$$

in such a way to make zero the total velocity on $\partial\Omega_b$, enforcing the no-slip boundary condition.

4.5.1 Discretization of the integral equations

Once the body contour is discretized in N_{body} points with uniform spacing Δs, the equations (4.62) and (4.63) must be written for this set of points.

To discretize the integrals in equations (4.62) and (4.63) a quadrature rule formula (Landrini (1993) and Di Salvo (1996)), in particular the generalized trapezoidal rule, is used. For a generic function f

$$\begin{aligned} \int_{\partial\Omega} f(z^\star(s))\mathcal{K}(z, z^\star(s))ds = \Delta s \sum_{i=2}^{N-1} f(z^\star(s_i))\mathcal{K}(z, z^\star(s_i)) + \\ + \frac{1}{2}[f(z^\star(s_1))\mathcal{K}(z, z^\star(s_1) + f(z^\star(s_N))\mathcal{K}(z, z^\star(s_N)] \end{aligned} \tag{4.70}$$

where Δs is the body constant discretization. Eq. (4.70) holds for every $z \notin \partial\Omega_b$, infact when $z \to z(z_i)$ with $z(s_i) \in \partial\Omega_b$ con $i = 1, ..., N_{body}$ the integral kernel $\mathcal{K}(z, z(s_i))$ become singular.

In this case the following expression can be used:

$$f(z^\star(s))\mathcal{K}(z(s), z^\star(s)) = f(s^\star)\mathcal{K}(s, s^\star) = \frac{\Phi(s^\star)}{s - s^\star} + \tilde{\Phi}(s) \tag{4.71}$$

where Φ is a function such that

$$\Phi(s) \neq 0, \ \forall s \in \partial\Omega_b \tag{4.72}$$

and $\tilde{\Phi}$ is a regular function $\forall s \in [0, \mathcal{P}]$. Thus the only integral to be evaluated is the principal value integral of the singular part of expression (4.71), it is possible to prove the following formula:

$$\oint_{\partial\Omega_b} \frac{\Phi(s^\star)}{s - s^\star} ds^\star = \Delta s \sum_{i=2}^{N_{body}-1} \frac{\Phi(s_i)}{s - s_i} + \frac{1}{2}\left[\frac{\Phi(s_1)}{s - s_1} + \frac{\Phi(s_N)}{s - s_N}\right] - \Delta s \frac{d\Phi}{ds}(s). \tag{4.73}$$

Using expression (4.73) it is possible to discretize the integrals in eq.s (4.62) and (4.63) in the following way

$$\begin{aligned}
\frac{1}{2\pi}\oint_{\partial\Omega_b} \sigma(z(s))\mathcal{K}(z, z(s))ds &= \frac{1}{2\pi}\sum_{i=1}^{N_{body}} \frac{\sigma(z(s_i))}{z - z(s_i)}\Delta s + \\
&\quad + \frac{1}{2\pi}\left(-\frac{\sigma(z)}{2}\left.\overline{\frac{d^2z}{ds^2}}\right|_z - \frac{1}{\tau}\frac{d\sigma}{ds}\right)\Delta s \quad z \in \partial\Omega_b \\
\frac{1}{2\pi i}\oint_{\partial\Omega_b} \gamma(z(s))\mathcal{K}(z, z(s))ds &= \frac{1}{2\pi i}\sum_{i=1}^{N_{body}} \frac{\gamma(z(s_i))}{z - z(s_i)}\Delta s + \\
&\quad + \frac{1}{2\pi i}\left(-\frac{\gamma(z)}{2}\left.\overline{\frac{d^2z}{ds^2}}\right|_z - \frac{1}{\tau}\frac{d\gamma}{ds}\right)\Delta s \quad z \in \partial\Omega_b
\end{aligned}$$

Substituting the previous formulas in eq.s (4.65) and (4.68) and defining the complex matrix $\mathbb{F}$ as

$$\mathbb{F}_{ij} = \begin{cases} \dfrac{1}{2\pi}\dfrac{\tau}{z_i - z_j} & i \neq j \\ -\dfrac{1}{2\pi}\overline{\left[\dfrac{(d^2z/ds^2)}{2(dz/ds)}\right]} & i = j \end{cases} \qquad i, j \in [1, N_b] \tag{4.74}$$

it is possible to obtain the following equations for σ and u_τ on the points of the body contour

$$\left[\frac{1}{2}\mathbb{I}+\mathcal{I}(\mathbb{F})\Delta s\right]\{\sigma\} = -\{\mathbf{u}_{body}\cdot\mathbf{n}\}+\{\mathbf{u}_\infty\cdot\mathbf{n}\}+\{\mathbf{u}_\omega\cdot\mathbf{n}\}+[\mathcal{R}(\mathbb{F})\Delta s]\{\gamma\}\,, \tag{4.75}$$

$$\{u_\tau\} = \left[\frac{1}{2}\mathbb{I}+\mathcal{I}(\mathbb{F})\Delta s\right]\{\gamma\}+[\mathcal{R}(\mathbb{F})\Delta s]\{\sigma\}-\frac{\Delta s}{2\pi}\left\{\frac{d\sigma}{ds}\right\}+ \\ -\{\mathbf{u}_{body}\cdot\tau\}+\{\mathbf{u}_\infty\cdot\tau\}+\{\mathbf{u}_\omega\cdot\tau\}\,. \tag{4.76}$$

where $\mathbb{I}$ is the identity matrix, $\{\cdot\}$ and $[\cdot]$ indicates a vector of dimension N_b and a matrix of dimension $N_b\times N_b$ evaluated on the body points respectively.

Using eq. (4.66), the right hand side of (4.75) is a known quantity. Solving eq. (4.75) gives the σ distribution on the points of the body contour. Once the σ distribution is known, it is possible to solve eq. (4.76) to obtain the tangent velocity on the body contour u_τ.

To enforce the no slip boundary condition it is now possible to generate a set of vortices on the body contour with positions the positions of the N_b body points and with circulations given by

$$\Gamma_i = u_\tau(\mathbf{r}_i)\Delta s,\quad i=1,...,N_b.$$

4.6 DIFFUSION

During the diffusive step the velocity of the vortices is neglected and the diffusive effect are accounted by solving the following heat equation

$$\frac{\partial\omega}{\partial t}=\nu\Delta\omega. \tag{4.77}$$

To represent the solution of this equation for a fluid confined in a domain Ω with boundaries $\partial\Omega$ it is possible to use the fundamental solution of the heat equation

$$\mathcal{F}(\mathbf{r}^\star-\mathbf{r},t-t') = \frac{1}{4\pi\nu(t-t')}\exp\left\{-\frac{|\mathbf{r}^\star-\mathbf{r}|^2}{4\nu(t-t')}\right\} \tag{4.78}$$

to write a general solution for the heat equation in the following way

$$\omega(\mathbf{r},t) = -\nu\int_{t_0}^{t}\int_{\partial\Omega}\left[\mathcal{F}(\mathbf{r}^\star-\mathbf{r},t-t')\frac{\partial\omega}{\partial n}(\mathbf{r}^\star)-\omega\frac{\partial\mathcal{F}}{\partial n}(\mathbf{r}^\star-\mathbf{r},t-t')\right]d\mathbf{r}^\star dt'+ \\ +\int_\Omega\omega(\mathbf{r}^\star,t_0)\mathcal{F}(\mathbf{r}^\star-\mathbf{r},t-t_0)d\mathbf{r}^\star \tag{4.79}$$

where $\omega(\mathbf{r}^\star,t_0)$ is the initial vorticity distribution.

A discrete version of eq. (4.79) is presented in the following sections to solve diffusion both in free space and in presence of solid boundaries, the discrete

versions of eq.(4.79) are used to give the diffusive contribution of each point vortex to the RPD nodes, after the diffusion process the former distribution of vorticity is substituted by a new one whose vortices are placed on the RPD nodes involved in the diffusion process.

4.6.1 Diffusion of a single vortex particle in free-space

Equation (4.79) takes a very simple form when dealing with free space problems

$$\omega(\mathbf{r},t) = \int_{\Omega} \omega(\mathbf{r}^{\star},t_0)\mathcal{F}(\mathbf{r}^{\star}-\mathbf{r},t-t_0)d\mathbf{r}^{\star} \tag{4.80}$$

where $\mathcal{F}(\mathbf{r}^{\star}-\mathbf{r},t-t_0)$ is the fundamental solution of the heat equation defined in eq. (4.78).

Consider now a single point vortex with position $\mathbf{r}_i$ and strength Γ_i, the solution of the heat equation for this initial condition is given by:

$$\omega(\mathbf{r},t) = \Gamma_i \frac{1}{4\pi\nu(t-t_0)} \exp\left\{-\frac{|\mathbf{r}^{\star}-\mathbf{r}|^2}{4\nu(t-t_0)}\right\}. \tag{4.81}$$

Therefore, even starting with all the circulation concentrated at time t_0 on a single point vortex, for $t = t_0 + \Delta t_d$ we have a distribution of vorticity on all $\mathbb{R}^2$, leading to a situation that is not possible to deal with numerically. To solve this problem we define a finite support for equation (4.80):

$$\begin{cases} \omega(\mathbf{r},t_0+\Delta t_d) = \Gamma_i \dfrac{1}{4\pi\nu\Delta t_d} \exp\left[-\dfrac{(r-r_i)^2}{4\nu\Delta t_d}\right] & \text{if} \quad |\mathbf{r}-\mathbf{r}_i| \leqslant R_d \\ \omega(\mathbf{r},t_0+\Delta t_d) = 0 & \text{otherwise} \end{cases} \tag{4.82}$$

where the gaussian distribution has been truncated at distance R_d for numerical purpose. R_d is called "diffusive radius" and it is a key parameter of the convergence properties of the DVH scheme (see Rossi et al. (2014a)). The relative error in the conservation of circulation introduced by this truncation is:

$$\xi = \left|\frac{\Gamma(t_0+\Delta t_d)-\Gamma(t_0)}{\Gamma(t_0)}\right| = \exp\left(-\frac{R_d^2}{4\nu\Delta t_d}\right) \tag{4.83}$$

This expression is used in the next section to determine the diffusive time step Δt_d.

Following Benson et al. (1989), eq. (4.82) can be used to distribute the vorticity of each vortex over its associated RPD which is characterized by a resolution length Δr (see sketch in figure 4.4).The vorticity field afterdiffusion is then lumped into point vortices located at the nodes of the lattice.

To preserve the conservation of the circulation of each vortex we must undergo a renormalization procedure of the diffused vorticity. Call $\mathbf{r}_j$ the position

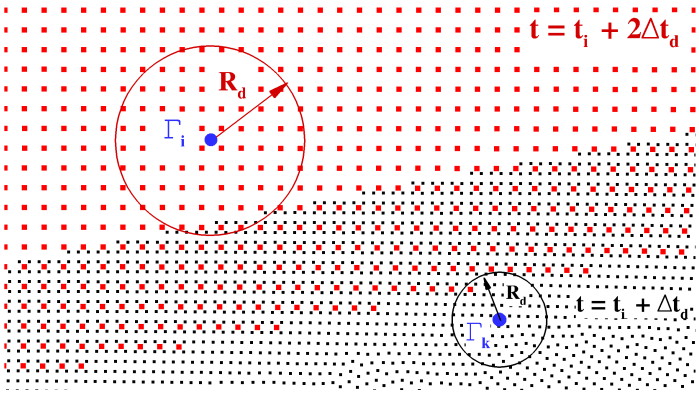

Figure 4.4: Sketch of the vorticity diffusion of two vortex particles in free space using the two associated RPDs

of a generic RPD node, the contribution to the circulation of the node $\mathbf{r}_j$ of the vortex with position $\mathbf{r}_k$ and circulation Γ_k in the time interval Δt_d using eq. (4.82) and the Stokes' theorem, is:

$$\Gamma_j^{(k)} = \frac{\Gamma_k}{4\pi\nu\Delta t} \exp\left\{-\frac{|\mathbf{r}_j - \mathbf{r}_k|^2}{4\nu\Delta t_d}\right\} \Delta r^2 \,. \tag{4.84}$$

Thus to normalize this circulation in r_j the following formula can be used:

$$\Gamma_j^{(k)\prime} = \frac{\Gamma_k}{\sum_l \Gamma_l^{(k)}} \Gamma_j^{(k)} \tag{4.85}$$

where the sum over l is made over set of RPD points with distance from $\mathbf{r}_k$ less than or equal to R_d. It is easy to see that a sum over j of the normalized circulations gives exactly the circulation Γ_k.

After all the vortices have spread their diffusive contributions to the circulations of the points, to reduce the number of vortices generated in this diffusive process the nodes with circulation lower than a fixed cut-off Γ_{cutoff} can be eventually removed.

4.6.2 Diffusion in the presence of a solid boundary

If the vortex particle is at a distance from a solid surface that is less than R_d, the presence of the boundaries needs to be taken into account in the solution of the heat equation. Consider now the solution of the heat equation (4.79)

$$\omega(\mathbf{r}, t) = -\nu \int_{t_0}^{t} \int_{\partial\Omega} \left[\mathcal{F}(\mathbf{r}^\star - \mathbf{r}, t - t') \frac{\partial\omega}{\partial n}(\mathbf{r}^\star) - \omega \frac{\partial\mathcal{F}}{\partial n}(\mathbf{r}^\star - \mathbf{r}, t - t')\right] d\mathbf{r}^\star dt' +$$

$$+ \int_\Omega \omega(\mathbf{r}^\star, t_0) \mathcal{F}(\mathbf{r}^\star - \mathbf{r}, t - t_0) d\mathbf{r}^\star$$

to solve this equation both the vorticity field ω and its normal derivative on the body contour $\partial\omega/\partial n$ must be known on $\partial\Omega_b$.

In what follows an homogeneous Neumann condition for the vorticity field will be considered

$$\left(\frac{\partial\omega}{\partial n}\right)_{\partial\Omega} = 0 \tag{4.86}$$

describing the reflection of the vorticity field inside the fluid domain in presence of solid boundaries.

Using equation (4.86) in (4.79) gives

$$\begin{aligned}\omega(\mathbf{r},t) &= \nu\int_{t_0}^{t}\int_{\partial\Omega}\omega\frac{\partial\mathcal{F}}{\partial n}(\mathbf{r}^\star-\mathbf{r},t-t')d\mathbf{r}^\star dt'+\\ &+\int_{\Omega}\omega(\mathbf{r}^\star,t_0)\mathcal{F}(\mathbf{r}^\star-\mathbf{r},t-t_0)d\mathbf{r}^\star\end{aligned} \tag{4.87}$$

where the unknown value of ω on $\partial\Omega$ must be found by solving the following equation

$$\begin{aligned}\frac{1}{2}\omega(\mathbf{r}',t) &= \nu\int_{t_0}^{t}\int_{\partial\Omega}\omega\frac{\partial\mathcal{F}}{\partial n}(\mathbf{r}^\star-\mathbf{r}',t-t')d\mathbf{r}^\star dt'+\\ &+\int_{\Omega}\omega(\mathbf{r}^\star,t_0)\mathcal{F}(\mathbf{r}^\star-\mathbf{r}',t-t_0)d\mathbf{r}^\star\end{aligned} \tag{4.88}$$

where $\mathbf{r}' \in \partial\Omega$.

Another way to find a solution of equation (4.87) is to use a Green function $\mathcal{F}_\Omega$, instead of $\mathcal{F}$, dependent on the particular choice of the fluid domain domain Ω, such that:

$$\left(\frac{\partial\mathcal{F}_\Omega}{\partial n}\right)_{\partial\Omega} = 0 \tag{4.89}$$

where n is the normal unit vector on $\partial\Omega$.

With this choice eq. (4.87) reduces to

$$\omega(\mathbf{r},t) = \int_{\Omega}\omega(\mathbf{r}^\star,t_0)\mathcal{F}_\Omega(\mathbf{r}^\star-\mathbf{r},t-t_0)d\mathbf{r}^\star. \tag{4.90}$$

If, on one hand, this choice eliminates all the boundary integrals from the expression of the solution of the heat equation, on the other hand introduces the Green function $\mathcal{F}_\Omega$ dependent on the geometry of the fluid domain Ω.

A particular case in which $\mathcal{F}_\Omega$ can be easily evaluated is in the case of an infinite flat plate. In this case the images method can be used and the diffusion of a single point vortex of position $\mathbf{r}_i$ and strength Γ_i is accounted by substituting to the flat plate an image vortex with the strength $\Gamma^{(im)} = \Gamma_i$ and placed symmetrically to the vortex with respect to the plate.

The diffusion of a single point vortex in presence of a flat plate is therefore solved by diffusing two point vortices in free space, meaning that the Green function $\mathcal{F}_\Omega$ for this problem is

$$\begin{aligned}\mathcal{F}_\Omega(\mathbf{r}_i-\mathbf{r},t-t') &= \frac{1}{4\pi\nu(t-t')}\exp\left\{-\frac{|\mathbf{r}_i-\mathbf{r}|^2}{4\nu(t-t')}\right\}+\\ &+ \frac{1}{4\pi\nu(t-t')}\exp\left\{-\frac{|\mathbf{r}_i^{(im)}-\mathbf{r}|^2}{4\nu(t-t')}\right\}\end{aligned} \tag{4.91}$$

where $\mathbf{r}_i^{(im)}$ is the position of the image vortex.

The same approximation (4.82) introduced in the previous section for the diffusion of a single point vortex in free space can be used for the diffusion in presence of a flat plate, writing the solution of the heat equation in the following way

$$\begin{cases}\omega(\mathbf{r},t_0+\Delta t_d) = \Gamma_i\dfrac{1}{4\pi\nu\Delta t_d}\left[\exp\left\{-\dfrac{|\mathbf{r}_i-\mathbf{r}|^2}{4\,\nu\Delta t_d}\right\}+\right. & \\ \qquad\left.+\exp\left\{-\dfrac{|\mathbf{r}_i^{(im)}-\mathbf{r}|^2}{4\,\nu\Delta t_d}\right\}\right] & \forall|\mathbf{r}_i-\mathbf{r}|\leqslant R_d \\ \omega(\mathbf{r},t_0+\Delta t_d) = 0 & \text{otherwise}\end{cases} \tag{4.92}$$

where the image vortex gives contribution only on those points $\mathbf{r}$ of the fluid domain such that $\left\{\mathbf{r}:(|\mathbf{r}_i-\mathbf{r}|\leqslant R_d)\cap(|\mathbf{r}_i^{(im)}-\mathbf{r}|)\leqslant R_d\right\}$.

If the vortex particle is at a distance from a solid surface that is less than R_d equation (4.92) can be used, otherwise the diffusion can be solved using equation (4.82), neglecting the effects of the body for vortices that are at a distance greater or equal to R_d from the solid surface.

Equation (4.92) is strictly valid only for flat plate problems, however when dealing with solid surfaces with generic shapes if the diffusive radius R_d is small enough to make the body curvature not relevant it is possible to locally approximate the body with a straight line. In this case it is possible to solve the diffusion near the body using the method just described.

Once the image vortex has been constructed, both the image and the vortex gives their diffusive contribution to the RPD nodes at a distance lower or equal to R_d by the use of eq. (4.92). To preserve the conservation of the circulation of each vortex we must undergo the same renormalization procedure described in the previous section.

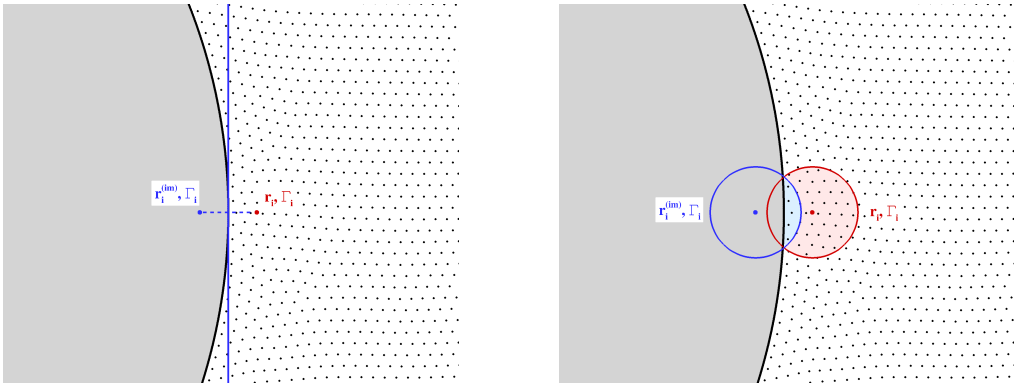

(a) (b)

Figure 4.5: Diffusion in the presence of a solid boundary:(a) construction of the image vortex, (b) Points of the RPD influenced by diffusion

4.6.3 Diffusion in presence of geometrical singularities

If the body has a complex geometrical shape with edges, like for example the one represented in fig. 6.1(a), the flat wall approximation described in the previous section is no longer true: in fact there will always be a set of vortices near the edges for which, no matter how near to the body they are, the will always see the geometrical singularities of the body.

Near an edge of the body three different zones S_1, S_2 and S_3 can be defined using the normal vectors $\mathbf{n}_1$ and $\mathbf{n}_2$ on the two side of the edge as depicted in figure 4.6(a).

One way to perform diffusion near the edges is to use the flat plate approximation for all the vortices in zone S_1 (S_2) using the formulas described in section 4.6.2 while when a vortex is in zone S_3 it diffuses as if it is in free space, i.e. using the formulas of section 4.6.1 without the construction of the image vortex.

Figure 4.6(b) depicts the diffusion of a vortex in zone S_1 as described in section 4.6.2 using the flat plate approximation. The flat plate approximation is also used if the vortex is at a distance lower than R_d from the edge, figure 4.6(c) depicts this case showing the extension of the body used for the flat plate approximation. The same things are true if the vortex is in zone S_2.

Figure 4.6(d) depicts the diffusion of a vortex in zone S_3, it diffuses as if it is in free space giving diffusive contribution to the RPD nodes using formulas of section 4.6.1.

This method is, on one hand, rather simple to implement but, on the other hand, introduces a discontinuity in the treatment of the diffusion process when changing zone from S_1 (or S_2) to S_3.

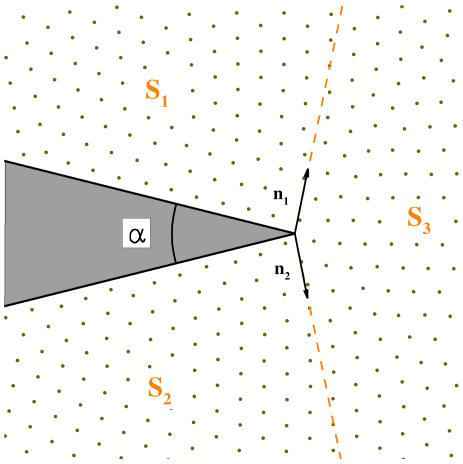

(a) Near body zone subdivision: $\mathbf{n}_1$ and $\mathbf{n}_2$ are the normal vectors on the two side of the edge

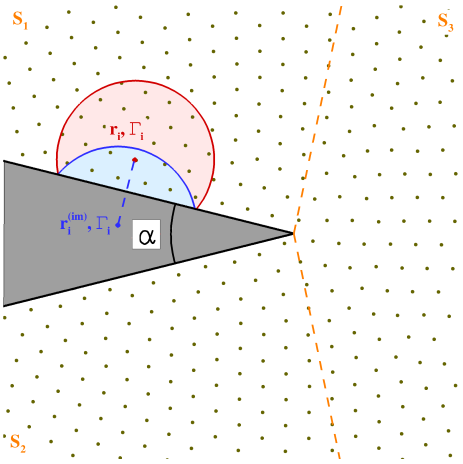

(b) Diffusion of a vortex in zone S_1 with flat plate approximation far from the edge

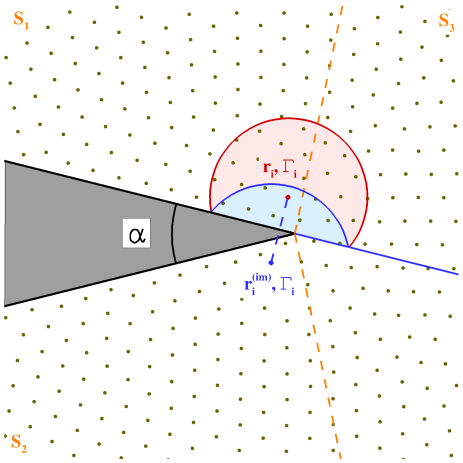

(c) Diffusion of a vortex in zone S_1 with flat plate approximation near the edge

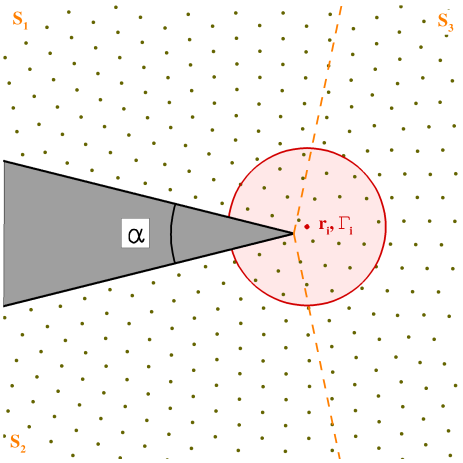

(d) Diffusion of a vortex in zone S_3

Figure 4.6: Diffusion in presence of a body with edges: near body zone subdivision and diffusion scheme using flat plate approximation. The red zones highlight the RPD node that takes diffusive contributions only from the vortex (red point) while the blue zone highlight the RPD node that takes diffusive contributions from both the vortex and the image (blue point).

For this reason the diffusion algorithm has been modified to make the diffusion process continuous when changing zone. The equation used to diffuse a single vortex is the following

$$\begin{cases} \omega(\mathbf{r}, t_0 + \Delta t_d) = \Gamma_i \dfrac{1}{4\pi\nu\Delta t_d}\left[\exp\left\{-\dfrac{|\mathbf{r}_i - \mathbf{r}|^2}{4\nu\Delta t_d}\right\} + \right. & \forall \mathbf{r} \in B_i \\ \left. + \exp\left\{-\dfrac{|\mathbf{r}_i^{(im)} - \mathbf{r}|^2}{4\nu\Delta t_d}\right\}\right] & \\ \omega(\mathbf{r}, t_0 + \Delta t_d) = 0 & \text{otherwise} \end{cases} \tag{4.93}$$

where B_i is a subset of RPD nodes contained in the circle of radius R_d centered on the vortex position. The image vortex, whose position is $\mathbf{r}_i^{(im)}$, gives contribution only on those points $\mathbf{r}$ of the fluid domain such that

$$\left\{\mathbf{r} : B_i \cap (|\mathbf{r}_i^{(im)} - \mathbf{r}|) \leqslant R_d\right\}. \tag{4.94}$$

The set of points B_i must be determined in such a way to make the diffusion process continuous when changing zone from S_1 (or S_2) to S_3.

To determine the RPD nodes inside the support B_i an algorithm, called visibility mask, has been introduced. The action of the visibility mask is depicted in Fig. 4.7: a vortex near an edge of the body is allowed to diffuse only on those RPD points at a distance less or equal to the diffusive radius from the vortex for which a line passing through the vortex and the RPD point under consideration do not intersect the body.

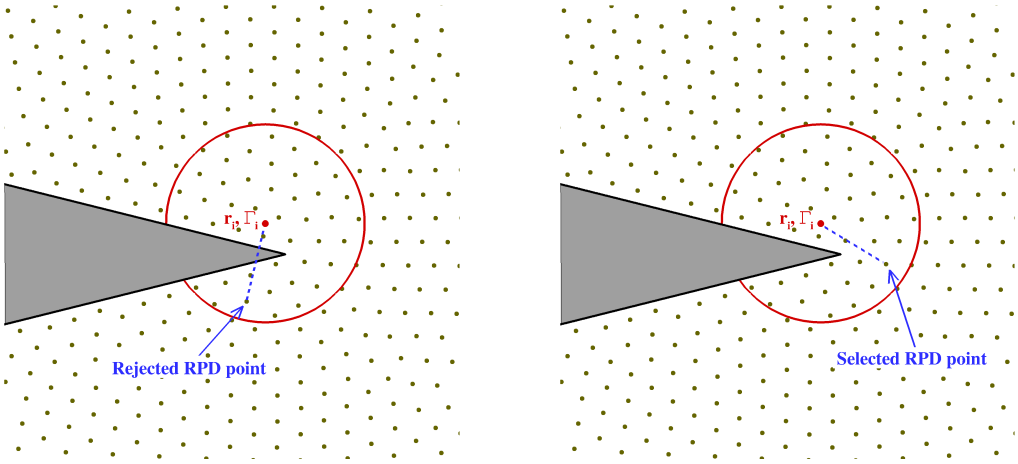

Figure 4.7: Action of the visibility mask algorithm. Left: example of a rejected RPD node. Right: example of a selected RPD node.

Figure 4.8 depicts the RPD points selected (the points inside the red zone) using the visibility mask algorithm in four different situations. Note that changing the position of the vortex through the different zones S_1, S_2 and S_3 the

support B_i changes with continuity. During the diffusion process each vortex gives its diffusive contribution to the RPD points selected this way using equation (4.93).

The effect of the body on the diffusion process is accounted using an image vortex giving diffusive contribution on the RPD points inside the intersection of expression (4.94). Figure 4.9 depicts the position of the image, together with its influence area, for different positions of the vortex. In particular figure 4.9(a) depicts the case of a vortex in zone S_1 at a distance greater than R_d

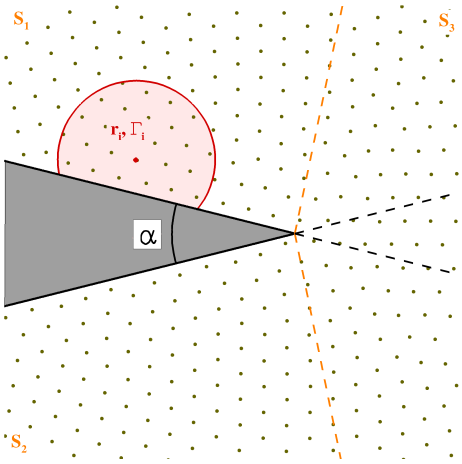

(a) Vortex in zone S_1 at a distance greater than R_d from the edge

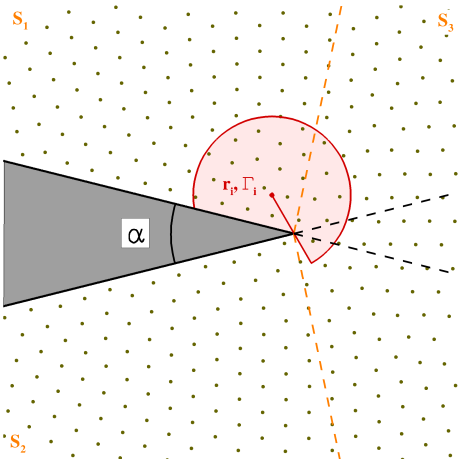

(b) Vortex in zone S_1 at a distance lower than R_d from the edge

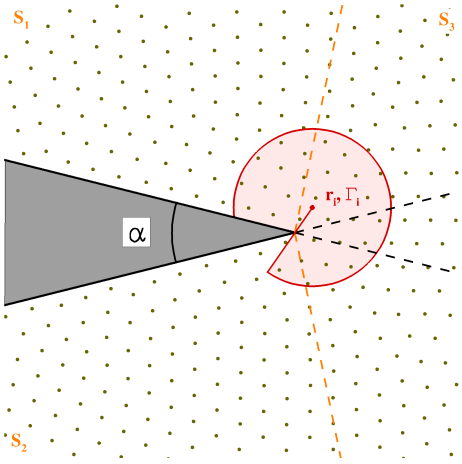

(c) Vortex in zone S_3 at a distance lower than R_d from the edge and on its side

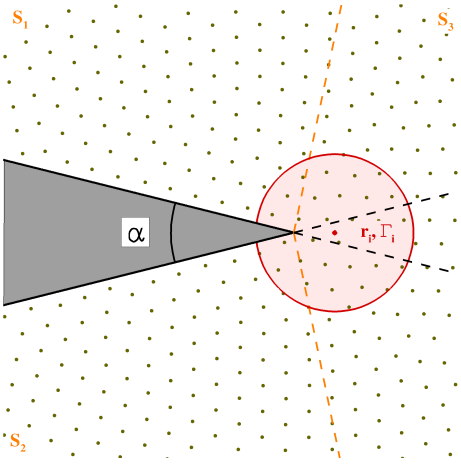

(d) Vortex in zone S_3 at a distance lower than R_d from the edge and in front of it

Figure 4.8: Construction of the support B_i for different position of the vortex using the visibility mask algorithm. The black dashed lines highlights the zone right in front of the edge.

from the edge, in this case the position of the image vortex is constructed as in section 4.6.2. Figure 4.9(b) depicts the case of a vortex in zone S_1 at a distance lower than R_d from the edge, also in this case the the position of the image is constructed by reflection of the vortex position with respect to the body

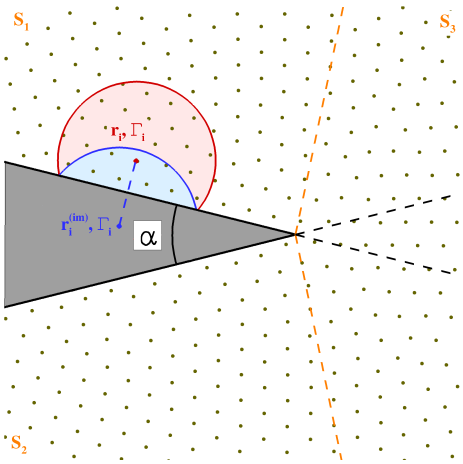

(a) Vortex in zone S_1 at a distance greater then R_d from the edge image position taken as the reflection with respect to the body tangent

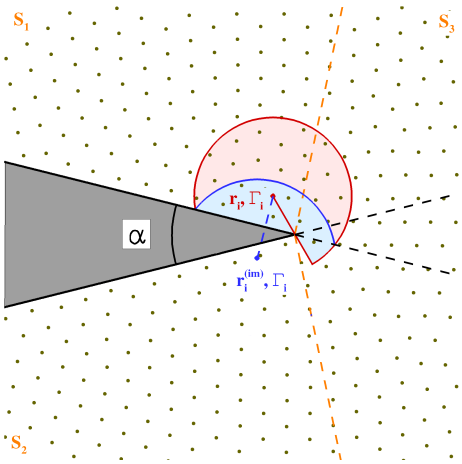

(b) Vortex in zone S_1 at a distance lower then R_d from the edge image position taken as the reflection with respect to the body tangent

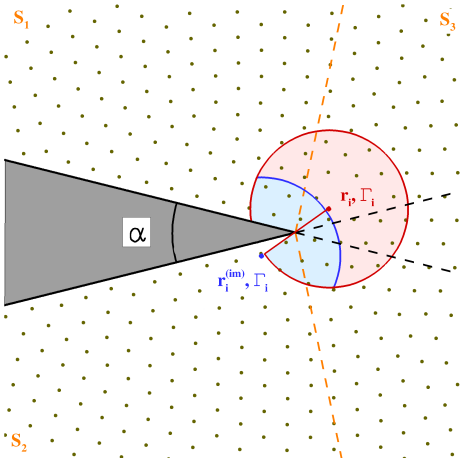

(c) Vortex in zone S_3 at a distance lower then R_d from the edge image position taken as the reflection with respect to the edge position

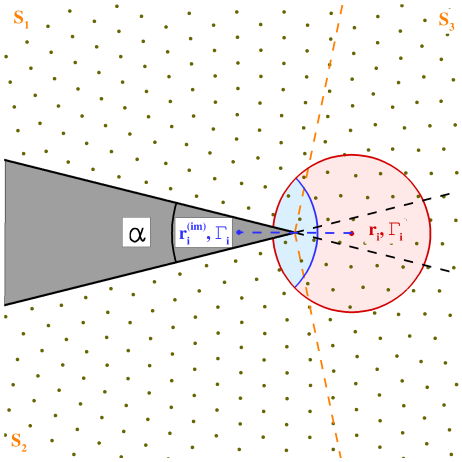

(d) Vortex in zone S_3 at a distance lower then R_d from the edge image position taken as the reflection with respect to the edge position

Figure 4.9: Image vortex position and diffusive influence zones. The red zones are the points on which only the vortex gives diffusive contribution. The ble zones are the points on which only both the vortex and its image give diffusive contribution.

tangent. Figures 4.9(c) and 4.9(d) depict two cases of a vortex in zone S_3, in this case the image position is constructed by reflection of the vortex position with respect to the edge position.

4.7 CHOICE OF TIME STEPS

Considering U and L as the reference velocity and length of the problem, the Reynolds number is defined as $Re = UL/\nu$. For the sake of simplicity a single RPD is considered with the linked spatial resolution equal to $L/\Delta r$.

Using (4.83) it is possible to define the diffusive time step in the following way

$$\Delta t_d \frac{U}{L} = \frac{(R_d/\Delta r)^2}{4\ln(1/\xi)} \frac{1}{(L/\Delta r)^2} Re, \tag{4.95}$$

(4.95) allows for the evaluation of the diffusion time step from the spatial resolution $L/\Delta r$, the ratio $R_d/\Delta r$ and the Reynolds number, once the error ξ has been fixed. The parameter used in this work are: $\xi = 10^{-5}$, $R_d/\Delta r = 4$ and therefore the expression (4.95) can be rewritten as:

$$\Delta t_d \frac{U}{L} \simeq 0.34 \frac{Re}{(L/\Delta r)^2} \tag{4.96}$$

The advection time step Δt_a can be chosen by considering the flow velocity U and the discretization Δr used during the diffusive step. A first evaluation of Δt_a can be chosen as:

$$\Delta t_a \frac{U}{L} = Co \frac{1}{(L/\Delta r)} \tag{4.97}$$

where Co is the Courant number. In the present work Co is maintained close to 1 to avoid that the vortex particles move with large displacements inducing particle disorder during the advective steps. Indeed, for the Reynolds number analysed in this work and for the ratios $L/\Delta r$ possible with the CPU resource available, this second constraint is always less restrictive than that related to the diffusion process (*i.e.* $\Delta t_a < \Delta t_d$, this inequality reverses when considering highly viscous flow or very high spatial resolutions).

This means that during a time interval Δt_d one or more advective step can be performed. In order to synchronize diffusion and advection, once Δt_a has been evaluated, it has to be rearranged to get Δt_d and Δt_a in an integer ratio:

$$N_{\Delta t} = \left[\frac{\Delta t_d}{\Delta t_a}\right] \rightarrow \Delta t_a = \frac{\Delta t_d}{N_{\Delta t}} \tag{4.98}$$

resulting in a correction to the real Courant number used in the simulations with respect to that initially imposed (see also Rossi et al. (2014b)).

To contain the growth of the number of vortex particles during the diffusive step, different RDPs with decreasing resolutions are adopted for increasing

distance from the body. It means that vortex particles are characterized by different diffusive time steps while all of them are moved with the same Δt_a. To synchronize the diffusion process the Δt_d for each RDPs must be chosen such that they are in integer ratio with each other (see sketch of figure 4.4).

5 SMOOTHED PARTICLE HYDRODYNAMICS THEORY RECALL

Another meshless particle method of great interest is the Smoothed Particle Hydrodynamic (SPH), it relies on a Lagrangian approach, that is, the fluid motion is described as a fluid-particle system and the derivatives of the flow quantities are computed along the trajectory of each particle. This leads to an intrinsic meshless character of the solver. The latter implies that the numerical grid points have no predetermined topological connections as in the case of mesh-based methods. The derivatives of the fluid quantities are evaluated for each particle through an interpolation procedure over its neighbouring particles. Thanks to these features the SPH method can naturally treat breaking waves and fragmentation that generally are not easily handled by standard methods.

SPH was first introduced by Lucy (1977) and further developed by Monaghan (1992) to study self-gravitating fluids and for many years SPH was used for astronomical problems; later, it was applied to several physics and engineering problems, ranging from solid mechanics to multiphase flows. Monaghan (1994) first applied it for simulating free-surface inviscid flows.

In the following section it will be given a brief recall of the theory concerning the SPH method starting with a description of the governing equation (section 5.1). In section 5.2 will be presented the discretized equation of the set of fluid particles while in sections 5.3 and 5.4 will be given a short descriptions of the choice made for the smoothing kernel and state equation respectively. Section 5.5 will be devoted to the description of the enforcement of the boundary conditions in the SPH model.

5.1 SPH GOVERNING EQUATIONS

Let us consider the Navier-Stokes equation for a barotropic weakly compressible fluid

$$\begin{cases} \dfrac{D\rho}{Dt} + \rho\nabla\cdot\mathbf{u} = 0 \\ \rho\dfrac{D\mathbf{u}}{Dt} = -\dfrac{1}{\rho}\nabla p + \nabla\cdot\mathbb{V} \\ p = p(\rho) \end{cases} \tag{5.1}$$

where $p = p(\rho)$ is the pressure state equation to be specified (see section 5.4) and $\mathbb{V}$ is the viscous part of the stress tensor

$$\nabla \cdot \mathbb{V} = (\lambda + \mu)\nabla(\nabla \cdot \mathbf{u}) + \mu\Delta\mathbf{u},$$

where λ and μ are the and the dynamic viscosity respectively.

In meshless method a generic scalar quantity is interpolated using the following convolution integral

$$\langle f \rangle(\mathbf{r}) = \int_\Omega f(\mathbf{r}')W(\mathbf{r} - \mathbf{r}'; h)\,d\mathbf{r}'. \tag{5.2}$$

where Ω is the portion of space occupied by the fluid.

The smoothing function $W(\mathbf{r} - \mathbf{r}'; h)$ must be positive and it must decrease monotonously with $\|\mathbf{r} - \mathbf{r}'\|$ to zero on $\partial\Omega$, practically the function W has a compact support of radius h, also called smoothing length.

The kernel is assumed symmetric and with radial symmetry such that it is a function of the distance $\|\mathbf{r} - \mathbf{r}'\|$ and of the smoothing length h that, for our purposes, will be considered constant.

Moreover the kernel W is considered normalized to unity on the domain Ω

$$\int_\Omega W(|\mathbf{r}|)\,d\mathbf{r} = 1$$

and $W \to \delta$ as $h \to 0$ where δ is the Dirac delta function.

The same interpolation can be applied to the evaluation of the derivatives of the generic scalar field f

$$\begin{aligned} \langle \nabla f \rangle &= \int_\Omega \nabla_{\mathbf{r}'} f(\mathbf{r}')W(\mathbf{r} - \mathbf{r}'; h)\,d\mathbf{r}' = \\ &= \int_\Omega f(\mathbf{r}')\nabla_{\mathbf{r}'} W(\mathbf{r} - \mathbf{r}'; h)\,d\mathbf{r}' + \int_{\partial\Omega} f(\mathbf{r}')W(\mathbf{r} - \mathbf{r}'; h)\mathbf{n}(\mathbf{r}')\,d\mathbf{r}' \end{aligned} \tag{5.3}$$

where $\mathbf{n}(\mathbf{r}')$ is the normal versor on the boundaries $\partial\Omega$ pointing outside Ω.

Note that the boundary integral in (5.3) vanishes if the compact support of the kernel W does not intersect any boundaries, in our case these boundary integrals are not zero only near the body contour and cannot be neglected because it is, in general, of the same order of magnitude of the volume integral.

It is possible now to introduce the smoothed Navier-Stokes equation

$$\begin{cases} \dfrac{D\rho}{Dt} + \rho\langle \nabla \cdot \mathbf{u} \rangle = 0 \\ \rho\dfrac{D\mathbf{u}}{Dt} = -\langle \nabla p \rangle + \langle \nabla \cdot \mathbb{V} \rangle \\ p = p(\rho) \end{cases} \tag{5.4}$$

here the smoothed viscous term is modelled through the one introduced by Monghan and Gingold

$$\langle \nabla \cdot \mathbb{V} \rangle(\mathbf{r}) = \mu K \int_{\Omega} \frac{(\mathbf{r}' - \mathbf{r}) \cdot [\mathbf{u}(\mathbf{r}') - \mathbf{u}(\mathbf{r})]}{|\mathbf{r}' - \mathbf{r}|^2} \nabla W(\mathbf{r}' - \mathbf{r}) d\mathbf{r}' \tag{5.5}$$

where K is a parameter depending on the spatial dimension ($K = 6, 8, 10$ in 1D, 2D and 3D respectively).

It has been proved (see e.g. Colagrossi et al. (2011)) that the viscous term converges to

$$\lim_{h \to 0} \langle \nabla \cdot \mathbb{V} \rangle = 2\mu \nabla(\nabla \cdot \mathbf{u}) + \mu \Delta \mathbf{u} \tag{5.6}$$

meaning that this term converges to the right equation only in the case $\lambda = \mu$ meaning that it does not satisfy the Stokes hypothesis $\lambda = -2\mu/3$.

5.2 SPH MODEL

In the present section a SPH scheme is briefly described. The fluid is assumed to be barotropic and weakly-compressible and the reference equations are the Navier-Stokes equations. As discussed in Molteni et al. (2007) and Colagrossi et al. (2009) different state equations, $p = f(\rho)$, can be used in the SPH scheme to model weakly-compressible fluids. Here, a simple linear state equation is used to match the pressure and density field:

$$p = c_0^2 (\rho - \rho_0) \tag{5.7}$$

where, c_0, ρ_0 and p_0 are the sound speed, the density and the pressure with the fluid at rest respectively. The speed of sound c_0 is set smaller than $0.01\rho_0$ in order to guarantee density variation. This is ensured through the following inequality:

$$c_0 \geqslant 10 \max_t \left[\max_{\Omega} \sqrt{p/\rho}, \max_{\Omega} |\mathbf{u}| \right]. \tag{5.8}$$

Given a set of particles each characterized by its own mass m_i, the particle densities can be expressed through the distribution:

$$\rho_i = \sum_j m_j \, \delta_\varepsilon(\mathbf{r}_i - \mathbf{r}_j) \tag{5.9}$$

where $\delta_\varepsilon = \delta_\varepsilon(\mathbf{r}_i - \mathbf{r}_j)$ is a positive, smooth approximation of the δ function as already introduced for the DVH (see section 3.2.1). In this work a C2 Wendland kernel (see *e.g.* Colagrossi et al. 2013) has been used. δ_ε has a compact support of radius 2ε, where in the SPH literature ε is referred to as the *smoothing length*.

By time differentiation of equation (5.9) we get the continuity equation in the SPH formalism:

$$\dot{\rho}_i = \sum_j m_j \, (\mathbf{u}_i - \mathbf{u}_j) \cdot \nabla_i \delta_\varepsilon(\mathbf{r}_i - \mathbf{r}_j) \tag{5.10}$$

Symbol ∇_i indicates the differentiation with respect to the position of the i-th particle, for the sake of simplicity in what follows $\nabla_i \delta_\varepsilon(\mathbf{r}_i - \mathbf{r}_j)$ will be shortened to $\nabla_i \delta_\varepsilon$. From the numerical point of view, evaluation of the density through time integration of (5.10) is preferable with respect to the direct use of (5.9) and becomes crucial when dealing with free-surface flows (see *e.g.* Colagrossi et al. (2013)).

For an isentropic fluid the sum the time variation of kinetic energy $\mathcal{E}_k$ and internal energy $\mathcal{E}_i$ of the particles system reads as:

$$\dot{\mathcal{E}}_k + \dot{\mathcal{E}}_i = \sum_i m_i \, \mathbf{u}_i \cdot \dot{\mathbf{u}}_i + \sum_i m_i \frac{p_i}{\rho_i^2} \dot{\rho}_i = 0. \tag{5.11}$$

By substituing equation (5.10) in (5.11) and by using the kernel property

$$\nabla_i \delta_\varepsilon = -\nabla_j \delta_\varepsilon$$

the acceleration of the i-th particle is given by:

$$\dot{\mathbf{u}}_i = -\sum_j m_j \left(\frac{p_i}{\rho_i^2} + \frac{p_j}{\rho_j^2} \right) \nabla_i \delta_\varepsilon. \tag{5.12}$$

The acceleration given in equation (5.12) is due to the pressure forces, while the viscous one can be modelled through the viscous formula of Monaghan and Gingold (1983) that preserves both linear and angular momenta.

Using the above equation for $\dot{\rho}_i$ and $\dot{\mathbf{u}}_i$ the SPH scheme reads:

$$\begin{cases} \dot{\rho}_i(t) = -\sum_j m_j \, (\mathbf{u}_j - \mathbf{u}_i) \cdot \nabla_i \delta_\varepsilon \\ \dot{\mathbf{u}}_i(t) = -\sum_j m_j \left(\frac{p_i}{\rho_i^2} + \frac{p_j}{\rho_j^2} \right) \nabla_i \delta_\varepsilon + \frac{\nu}{\rho_0} \sum_j m_j \, \pi_{ij} \, \nabla_i \delta_\varepsilon \\ \dot{\mathbf{x}}_i(t) = \mathbf{u}_i(t) \end{cases} \tag{5.13}$$

where ρ_i, p_i, $\mathbf{u}_i$ and m_i are density, pressure, velocity and mass of the i-th particle respectively, ν denotes the fluid kinematic viscosity while π_{ij} is the Monaghan & Gingold formula to model viscous forces:

$$\pi_{ij} = 2\,(n + 2) \, \frac{(\mathbf{u}_j - \mathbf{u}_i) \cdot (\mathbf{r}_j - \mathbf{r}_i)}{\|\mathbf{r}_j - \mathbf{r}_i\|^2} \tag{5.14}$$

where n is the spatial dimension of the problem at hand.

Thanks to the use of equation (5.11) the exact momentum conservation in (5.13) is guaranteed regardless of the state equation adopted.

The fluid particles are initially placed using the algorithm described in Colagrossi et al. (2012). Thanks to this procedure, at the initial instant all particles have approximately the same volume, namely V_0, which is equal to the fluid domain volume divided by the number of fluid particles. Consistently, the

particle mean spacing is denoted by $\Delta r = V_0^{1/n}$. The average number of particles in the kernel support is set by choosing the ratio $\varepsilon/\Delta r$. In the present work $\varepsilon/\Delta r$ is set equal to 2 which in two dimensions corresponds to about 50 interacting particles. For $\varepsilon \to 0$ and $\Delta x/\varepsilon \to 0$ the system (5.13) converges to the Navier-Stokes equations (see *e.g.* Di Lisio et al. (1998) and Colagrossi et al. (2011)).

Along with the volume distribution, the initial pressure and the velocity fields are prescribed as well. The initial density distribution $\rho_i(t_0)$ is evaluated by means of the state equation and the particle masses are computed through the equation $m_i = V_0\,\rho_i(t_0)$. The mass of the i-th particle remains constant during the time evolution ensuring the total mass conservation of the particles system.

5.3 CHOICE OF THE SMOOTHING KERNEL

To correctly integrate system (5.13) over time it is necessary to select a proper kernel function. In literature it is possible to find various possible choices for the smoothing function, one possibility is to use a Gaussina kernel with compact support

$$W(\mathbf{r}) = \begin{cases} \dfrac{e^{-(|\mathbf{r}|/h)^2} - C_0}{2\pi C_1} & \text{, if } |\mathbf{r}| \leqslant R_h \\ 0 & \text{, otherwise} \end{cases} \tag{5.15}$$

$$C_0 = e^{-(R_h/h)^2}; \qquad C_1 = \int_0^{R_h} r\left[e^{-(r/h)^2} - e^{-(R_h/h)^2}\right] dr$$

Here R_h is the cut-off radius for compact support of the smoothing kernel and it is usually set as $R_h = 3h$ (for further details see Monaghan (1992)).

Another possible kernel to be used in (**??**) is the following Wendland kernel that is positive defined and has continuous second derivatives

$$W(\mathbf{r}) = C \begin{cases} \left(2 - \dfrac{|\mathbf{r}|}{h}\right)^4 \left(1 + 2\dfrac{|\mathbf{r}|}{h}\right) & \text{, if } |\mathbf{r}| \leqslant R_h \\ 0 & \text{, otherwise} \end{cases} \tag{5.16}$$

$$C = \frac{7}{64\pi}$$

In this case a usual choice for the cut-off radius is $R_h = 2h$.

5.4 CHOICE OF THE STATE EQUATION

Although various choice for the state equation are possible, the Tait equation is generally used to model weakly compressible fluids (see Monaghan Monaghan (1994))

$$p = B\left[\left(\frac{\rho}{\rho_0}\right)^{\alpha} - 1\right] + p_0 \tag{5.17}$$

where B is linked to the speed of sound in the fluid, α is a constant set equal to 7 and p_0 is the pressure with the fluid at rest.

Usually the value of p_0 is set to zero however this choice may lead to negative pressures in the downstream flow inducing the generation of un-physical cavitation inside the fluid. It is possible to avoid this problem simply choosing a non-zero positive value for the background pressure p_0 (Morris).

In eq. 5.17 the pressure p only depends on variation of the density ρ and not of the specific entropy S. The speed of sound in the fluid is defined as:

$$c^2 = \left.\frac{\partial p}{\partial \rho}\right|_{S=const.} \tag{5.18}$$

and it follows from the Tait equation (5.17)

$$c^2 = c_0^2\left(\frac{\rho}{\rho_0}\right)^{\alpha-1}; \quad c_0^2 = \frac{B\alpha}{\rho_0} \tag{5.19}$$

thus the speed of sound is subjected to a polytropic law.

In SPH simulations the speed of sound at rest c_0 is fixed at the start of the simulations and it is chosen such that it follow the constrain

$$c_0 \geqslant 10 \max_t(\|\mathbf{u}\|); \quad Ma := \frac{\max_t(\|\mathbf{u}\|)}{c_0} \leqslant 0.1 \tag{5.20}$$

where $\max_t(\|\mathbf{u}\|)$ is the maximum expected velocity in the flui and Ma is the Mach number.

Under this assumptions it is possible to consider that the fluid is weakly compressible since these conditions implies a variation of the density of the fluid $\Delta\rho/\rho_0 \sim 0.01$, where $\Delta\rho$ is the variation of the density with respect of the reference density ρ_0, $\Delta\rho = \rho - \rho_0$.

Under this assumption it is possible to use another state equation obtained by linearization of the Tait equation

$$p = B\left[\left(\frac{\rho_0 + \Delta\rho}{\rho_0}\right)^{\alpha} - 1\right] + p_0 \simeq B\alpha\frac{\Delta\rho}{\rho_0} + p_0 = c_0^2(\rho - \rho_0) + p_0 \tag{5.21}$$

where terms of order $\mathcal{O}[(\Delta\rho/\rho_0)^2]$ have been neglected.

In the same way eq. (5.19) can be linerized

$$c = c_0\left(\frac{\rho_0 + \Delta\rho}{\rho_0}\right)^{\frac{\alpha-1}{2}} \simeq c_0\left(1 + \frac{\alpha-1}{2}\frac{\Delta\rho}{\rho_0}\right) \tag{5.22}$$

where terms of order $\mathcal{O}[(\Delta\rho/\rho_0)^2]$ have been neglected.

From eq. (5.21) and (5.22) it is possible to see that the parameter α does not affect the pressure field while induces small variations in the speed of sound through fluctuations of the density field. This means that under the weakly compressible assumptions the pressure can be described using eq. (5.21) instead of the Tait equation (5.17) and the speed of sound can be considered constant $c = c_0$.

5.5 BOUNDARY CONDITIONS IN SPH MODEL

The definition of the correct boundary conditions on solid surfaces in a SPH framework is a complex matter. The problem arises when the support of the smoothing kernel W is truncated by the presence of solid boundaries leading to a decrease of the accuracy of the interpolation itself.

During the years various methods have been proposed by different researchers to overcome the loss of accuracy due to the reduced support of the kernel and to enforce the correct boundary condition. Two are the most used approach: ghost particle (see e.g. Libersky et al. (1993); Takeda et al. (1994); Morris et al. (1997)) and repulsive-type particles (see e.g. Monaghan (1994); Monaghan and Kajtar (2009)).

Both the methods have significant drawbacks that do not allow a general and accurate modelling of solid boundaries. Indeed, in the standard ghost method, ad hoc tuning for curves and angles are needed to avoid local excess (or lack) of ghost mass (see e.g. Oger et al. (2006); Yildiz et al. (2009)). On the other hand, the use of repulsive particles produces an unphysical numerical noise into the pressure field.

In the present work it has been adopted the *fixed ghost particle* technique described in Bouscasse et al. (2013) and Marrone et al. (2013).

The ghost particle are generated starting from the body discretization points spaced with distance Δs (see Marrone et al. (2011)). To every body points is associated a normal unit vector pointing inside the body (outside the fluid), every body point is displaced along the normal direction of a quantity $\Delta s/2$ and the new points generated this way are used to approximate a new profile thet will be discretized into equispaced particles with spacing Δs. These new particles represents an extension of the body profile, repeating this procedure until a whole radius R_h of the support of the smoothing kernel is covered lead to the fixed ghost particles. The same procedure is repeated using a normal unit vector pointing towards the fluid to create the interpolation point associated to the ghost particles

The ghost particles are fixed in the frame of reference of the body and the values attributed to those particles are calculated in their mirror point inside the fluid. Then, the interpolated quantities are evaluated through a Moving-

Least Square (MLS) interpolation (see e.g. Fries and Matthies (2004)) of the fluid particle values.

To enforce the no-slip boundary condition the velocity field has to be mirrored on the ghost particles (see Marrone et al. (2013)). Denoting by $\mathbf{u}_k^{(g)}$ the mirrored field at the position of the k-th ghost particle

$$\begin{cases} \mathbf{u}_k^{(g)} \cdot \tau &= \left[\left(\mathbf{u}^{(b)} - \mathbf{u}_i \right) \dfrac{d_k^{(b)}}{d_i^{(b)} + \eta \Delta r} + \mathbf{u}^{(b)} \right] \cdot \tau \\ \\ \mathbf{u}_k^{(g)} \cdot \mathbf{n} &= \mathbf{u}_i \cdot \mathbf{n} \end{cases} \tag{5.23}$$

where τ and $\mathbf{n}$ are the tangent and normal unit vectors on the body contour respectively, $\mathbf{u}_i$ is the velocity of the i-th fluid particle and $\mathbf{u}^{(b)}$ is the velocity of the body. $d_k^{(b)}$ and $d_i^{(b)}$ denotes the distance of the k-th ghost particle and of the i-th fluid particle from the body contour respectively, while η is a non dimensional parameter used to avoid singularities in the mirroring technique when the fluid particle moves too close to the body surface.

6 RPD GENERATION USING A PACKING ALGORITHM

In SPH scheme the way to initialize the particle positions plays an important role. If particles are not initially set in "equilibrium" positions they may resettle generating non-physical currents and/or vorticity. Thus an equilibrium configuration must be thought as the set of particle positions that do not lead to particle resettlement.

As proved in Colagrossi et al. (2012), the spurious particle motion is caused by inaccuracies in the SPH representation of the pressure gradient, in particular it is due to the lack of the zero-th order consistency of the momentum equation, that is the ability in maintaining an exactly constant pressure field, when particles are arbitrarily distributed.

Thus a solution to this problem is to initialize the particles positions in an equilibrium configuration.

In section 6.1 the algorithm proposed, called packing algorithm, in Colagrossi et al. (2012) to attain a regular particle distribution is briefly discussed.

This algorithm is of great interest not only for the SPH method but also for the DVH. In fact the ability of the packing algorithm to arrange equispaced points around bodies of arbitrary geometry can be used to create RPDs. The generation of these RPD will be discussed in section 6.2.

6.1 PACKING ALGORITHM

The normalization of the smoothing kernel W (defined in section 5.3) in discretized form can be written as

$$Z_i = \sum_j W_{ij} V_j. \tag{6.1}$$

where the summation is extended over the points inside the compact support of W, V_j is the volume associated to the j-th particle and

$$W_{ij} = W(\mathbf{r}_i - \mathbf{r}_j). \tag{6.2}$$

Due to possible univeness of the particle distribution the normalization may not be exactly satisfied inside the fluid domain. To measure the univeness of the particle distribution, together with eq. (6.1), it is useful to introduce the following quantity

$$\nabla Z_i = \sum_j \nabla_i W_{ij} V_j. \tag{6.3}$$

In fact in case of a uniform particle distribution the normalization of the smoothing kernel would be exactly satisfied giving $Z_i = 1$ and $\nabla Z_i = 0$, otherwise $Z_i < 1$ and $\nabla Z_i \neq 0$. This means that it is possible to initialize the particle distribution on a regular set of points minimizing the functional $\|\nabla Z$. This may be realized noting that the quantity

$$w = -\nabla Z \tag{6.4}$$

has always the direction of the maximum lack of mass (points towards the "holes" in the particle distributions). For this reason it is possible to use the quantity w as a repulsive force between particles to adjust their initial position in order to have a uniform initial distribution.

If there is a body in the fluid domain (see e.g. fig. 6.1(a)) a repulsive force between the body and the particles must be added, in order to adjust the particles initial position to the body contour. In this case the force that the body exerts on the i-th particle can be written as

$$\mathbf{F}_i = \sum_{j=1}^{N_b} W_{ij} \mathbf{n}_j \Delta s \tag{6.5}$$

where N_b is the total number of points on the body contour with uniform spacing Δs, $\mathbf{n}_j = \mathbf{n}(\mathbf{r}_j)$ is the normal unit vector on the point $\mathbf{r}_j$ of the body contour.

Thus the evolution equation are given by

$$\begin{cases} \dfrac{D\mathbf{u}_i}{Dt} &= -\beta \left(\nabla Z_i + \mathbf{F}_i\right) + \mathbf{T}_i \\ \dfrac{D\mathbf{r}_i}{Dt} &= \mathbf{u}_i \end{cases} \tag{6.6}$$

Here $\mathbf{T}_i$ is a damping force that can be chosen independently from the adopted SPH scheme since it is just used to ensure the convergence of the Particle Packing Algorithmm and $\beta = 2p_0/\rho_0$. A typical value used for β is $\beta = 2$.

It is possible to prove that this dynamical system converges to a static and stable solution for which $\mathbf{u}_i = 0$ and $\nabla Z_i = 0$. Where the evolution of the particles is sufficiently near to this state, the evolution itself is stopped and the distribution obtained is used as the initial position for the fluid particle distribution (more details are given in Colagrossi et al. (2012)). The volume used for the initialization of the SPH is then given by $V = V_0$, the initial particle pressure p_i is assigned using the analytical expression for the hydrostatic pressure and the particle positions. Then, inverting the state equation, the initial density ρ is computed and, finally, the particle mass is obtained through $m_i = \rho_i V$. During the SPH simulations the particle masses are kept constant while the densities and the volumes are updated using the continuity equation and the relation $V_i = m_i/\rho_i$.

To ensure a uniform particle spacing, the number of points inside the compact support of the kernel W in eq. (6.1) must be kept as small as possible. A typical values for this number of points is about 6.

6.2 RPD GENERATION AROUND BODY OF ARBITRARY GEOMETRY

The "Regular Point Distributions"(RPDs) around the body are generated using a packing algorithm described in section 6.1 (for more details on the packing algorithm see Colagrossi et al. (2012)). This algorithm permits to arrange points around complex contours almost preserving the volume around each point. The computational cost of the packing algorithm is negligible with respect to the cost of the flow simulation. Furthermore, this algorithm is based on a simple particle-interactions model, and, therefore, it can be embedded easily in the DVH code.

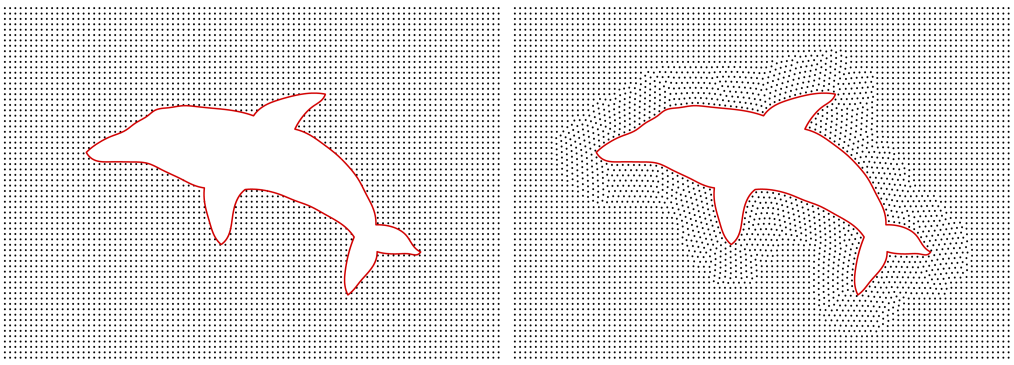

(a) (b)

Figure 6.1: RPD generation around a body of general shape: (a) before packing, (b) after packing

The body contour points are read by the code as an external file, then a spline representation is used in order to change the discretization with a desired spacing Δs. As a second step, points are placed around the body on a regular lattice with spacing Δr (see figure 6.1(a)) then the packing algorithm starts producing the new RPD (see figure 6.1(b)) which will be used for the viscous diffusion process in the DVH scheme. From figure 6.1(b) it is possible to see that at a certain distance the points are left on the Cartesian lattice.

The symmetries of the body geometry needs to be explicitly enforced around it during the packing algorithm. Otherwise, small asymmetries in the packed distribution will rise. These asymmetries reduce for decreasing Δr. These small asymmetries induce wake perturbations and vortex shedding takes place

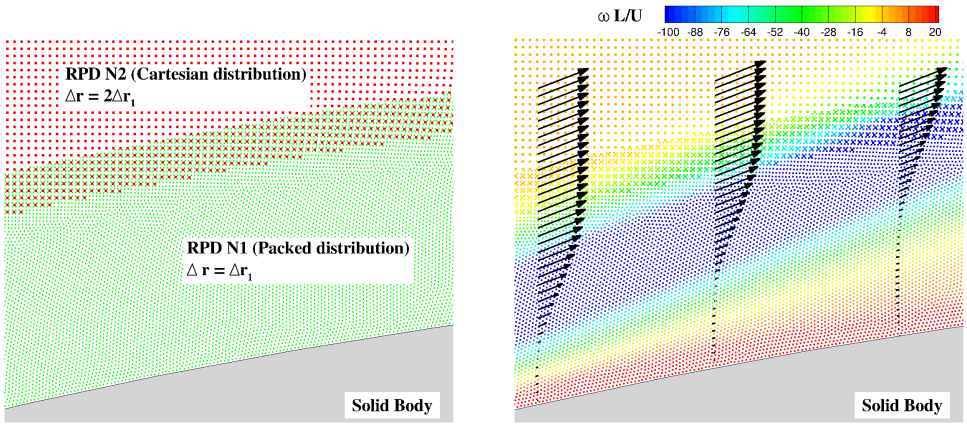

(a) (b)

Figure 6.2: Multiple RPDs around a solid surface (enlarged view): (a) Points distribution close and far from the body, (b) vorticity contour and velocity profiles in a region close to a flow separation.

without the necessity of using other perturbation techniques (see sections 8 and 9).

Once the RPD is generated around the solid body, it is possible to use simple Cartesian distributions far from it. An example is given in figure 6.2(a). There, close to the solid surface a packed configuration is used as a first RPD; far enough from the body a second RPD is used with points set on a Cartesian lattice and using a coarser spatial resolution. Figure 6.2(b) shows the vorticity field in the boundary layer region evaluated through eq. (4.4) and three velocity profiles are computed through a second convolution summation (see eq. (4.46)). From the results depicted in this figure it can be noticed that the overlapping of the two RPDs does not create problems when convolution summations are used to evaluate vorticity and velocity fields. Considering a body moving with an arbitrary motion, only the closest RPD needs to be moved while the other RDPs, being a simple Cartesian lattice, can be easily updated. The latter situation is not treated in the present work.

Part III

VALIDATIONS AND PHYSICAL INVESTIGATIONS

7 EVOLUTION OF VORTICITY FIELD IN FREE SPACE

In this section both the DVH and the SPH methods are tested by studying free vorticity dynamic in two dimension to heuristically measure the convergence of both methods.

In section 7.1 both methods are used to simulate the evolution of a vorticity distribution with the following initial conditions expressed in radial coordinates:

$$\omega(r,0) = \omega_0 e^{-(r/L)^2}; \quad u_0(r) = \omega_0 \frac{L^2}{2r}\left[1 - e^{-(r/L)^2}\right].$$

Although this test case present a very simple evolution, it is of great interest because there exist an exact solution for both the vorticity ω_{exact} and the velocity $\mathbf{u}_{exact}$. The errors and the convergence rate of the two numerical methods are then computed against this exact solution.

In section 7.2 behaviour of a merger of a pair of co-rotating vorticity patches is considered. In this case a large Reynolds number is used so that the dynamic of the merging process is not significantly influenced by the vorticity diffusion, the phenomenon is almost driven by the advection term while the diffusion process has a secondary role and could be relevant only for very low Reynolds numbers.

The results described in this section are also presented in Rossi et al. (2013) and Rossi et al. (2014a).

7.1 LAMB–OSEEN VORTEX TEST CASE

In this section an infinite fluid subjected to a radial force field: $f_r = -\beta^2 r \hat{r}$ is studied. β is a constant parameter, r is the radial coordinate and $\hat{r}$ is the radial unit vector. A velocity field merely tangential to circumferences centered in $r = 0$ is considered. An incompressible isotropic solution is searched and under these hypotheses the Navier-Stokes equations reduces to:

$$\begin{cases} -\dfrac{u^2}{r} = -\dfrac{1}{\rho_0}\dfrac{\partial p}{\partial r} - \beta^2 r, \\ \dfrac{\partial u}{\partial t} = \nu\left[\dfrac{1}{r}\dfrac{\partial}{\partial r}\left(r\dfrac{\partial u}{\partial r}\right) - \dfrac{u}{r^2}\right]. \end{cases} \tag{7.1}$$

where u is the tangential velocity while the radial one is identically null. In this framework the two equations are decoupled and it is possible to integrate

u by the second equation and evaluate the pressure field by the first one. Furthermore, we underline that the solution of u is not affected at all by the radial force field which only enters in the solution of the pressure field. Therefore, the DVH solutions are not affected by the parameter β, while this is not the case for the SPH method, we come back on this point at the end of this section.

The Lamb-Oseen vortex is characterized by an initial velocity field equal to:

$$u_0(r) = \omega_0 \frac{L^2}{2r}\left[1 - e^{-(r/L)^2}\right], \tag{7.2}$$

where L is the length scale of the problem. The corresponding vorticity contribution is a gaussian distribution:

$$\omega(r,0) = \omega_0\, e^{-(r/L)^2}, \tag{7.3}$$

therefore ω_0 is the vorticity in $r = 0$ at $t = 0$.

The exact solution of eq. (7.1) with initial datum given by eq.s (7.2) and (7.3) is:

$$u_{exact}(r,t) = \omega_0 \frac{L^2}{2r}\left[1 - \exp\left(-\frac{Re}{4\pi t\omega_0 + Re}\frac{r^2}{L^2}\right)\right], \tag{7.4}$$

(see figure 7.1(b)) where the Reynolds number is defined as $Re = \pi\,\omega_0\,L^2/\nu$.

The vorticity is then:

$$\omega_{exact}(r,t) = \omega_0 \frac{Re}{4\pi t\omega_0 + Re}\exp\left(-\frac{Re}{4\pi t\omega_0 + Re}\frac{r^2}{L^2}\right), \tag{7.5}$$

a gaussian vorticity shape is therefore maintained for all the time evolution (see figure 7.1(a)).

Such a simple problem is used to measure heuristically the convergence of DVH and SPH varying the Reynolds number. Indeed, the exact solution can be used to evaluate the relative errors over vorticity and velocity during simulations. In particular the relative error E_f for the function $f(\mathbf{r},t)$ is defined using a combination of L_1 norm in space and L_∞ in time:

$$E_f = \max_{t\in(0,t_{end}]} \frac{\int_\Omega |f_{exact}(\mathbf{r},t) - f(\mathbf{r},t)|d\mathbf{r}}{\int_\Omega |f_{exact}(\mathbf{r},t)|d\mathbf{r}}, \tag{7.6}$$

where Ω is the computational fluid domain. The latter is defined as a circular domain with radius $R = 20L$, in this way Ω is large enough to ensure that the vorticity field is almost negligible on $\partial\Omega$. The final time, t_{end}, is set equal to Re/ω_0, in this time range the maximum vorticity in Ω is reduced to about the 7% of the initial value ω_0.

In the analytical solution Re simply changes the time scale, however, in the next sections it is shown that increasing the Reynolds number the advection step becomes more and more important introducing errors both in the DVH

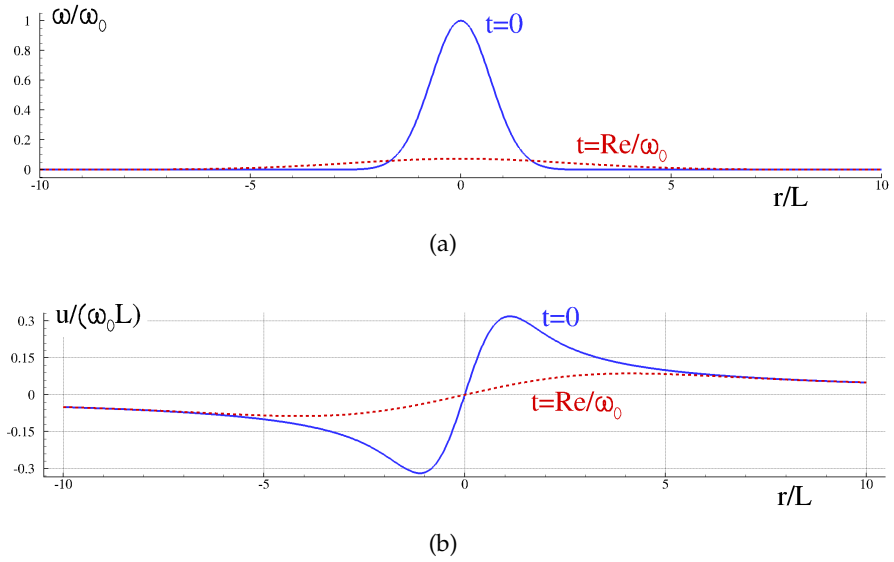

Figure 7.1: Vorticity (top) and Velocity (bottom) profiles for the Lamb Oseen Vortex at $t = 0$ and $t = Re/\omega_0$.

as well as in the SPH numerical scheme. Therefore, different error levels are expected upon changing the fluid viscosity.

Since in the DVH the boundary condition at infinity is automatically satisfied there is not any need to confine the fluid domain Ω. The vorticity field is discretized only for $r \leqslant 20L$ while beyond this distance the vorticity is neglected because of its small values.

Conversely, this is not the case for the SPH method which requires a closed domain. This is realized considering an annular region $r \in (20L, 20L + 2\varepsilon)$ where fictitious equispaced particles are positioned and where analytical values for u and p are imposed. The pressure is evaluated with the first equation of (7.1) where β^2 is set equal to $0.1\,\omega_0^2$ and a constant pressure value is set in order to get positive pressure inside Ω. This is done to avoid the excitation of the so called tensile instability (Swegle et al. (1995)) in the SPH method.

Numerical Results for the DVH

In this section the DVH model is tested on the Lamb-Oseen vortex problem. The test has been made in two steps: a set of simulations without advection has been performed to better control the error coming from the diffusive step. This test corresponds to the limit $Re \to 0$, then a new set of simulations has been made taking advection into account and considering increasing Re numbers.

As discussed in section 4.6, the diffusion of each point vortex is evaluated by discretizing eq. (4.82) on a regular distribution of points. Thus to reduce the errors made in this process we can either increase the number of points con-

tained in the support of radius R_d (*i.e.* increase the ratio $R_d/\Delta r$) or decrease the fixed relative error ξ (see eq. (4.83)) for the diffusion of each vortex. This second choice implies a reduction of the diffusive time step (see eq. (4.95)), which means that the diffusion equation is resolved with higher accuracy in time, while increasing the ratio $R_d/\Delta r$ implies higher accuracy in space. We call E_ω and E_u the relative error over vorticity and velocity, respectively, measured according to formula (7.6).

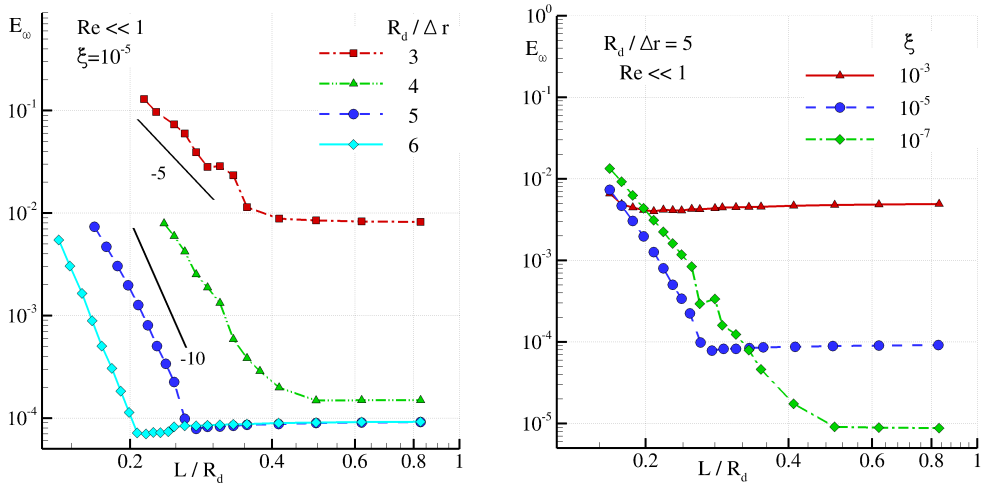

Figure 7.2: Left: Relative maximum error over vorticity as function of L/R_d for various ratio $R_d/\Delta r$ and $\xi = 10^{-5}$. Right: Relative maximum error over vorticity as function of L/R_d for various ξ and fixed ratio $R_d/\Delta r$.

Figure 7.2(a) shows the relative errors E_ω obtained for the Lamb-Oseen problem for the case $Re \to 0$, changing the spatial resolution L/R_d. Four different ratios $R_d/\Delta r$ are considered: 3, 4, 5 and 6 and ξ is set equal to 10^{-5}.

From this plot it is possible to see that there are essentially two regimes varying the spatial resolution L/R_d: (i) a first regime, for low spatial resolutions, where the errors reduce (*i.e.* the numerical solver is convergent) and (ii) a second regime where E_ω saturates. The convergence steepness in the first regime depends on the ratio $R_d/\Delta r$ in particular a convergence rate equal to 5 for $R_d/\Delta r = 3$ up to 10 for $R_d/\Delta r = 6$ are measured. On the second regime the solution is no more affected by the number of vortices used to discretize the fluid domain; the only way to reduce the errors is to increase the ratio $R_d/\Delta r$ or to reduce ξ,. This kind of convergence behaviour is typical of the meshless methods where the convergence requires the reduction of some parameters, in this case $\Delta r/L$, the ratio $\Delta r/R_d$ and ξ (see *e.g.* Mas-Gallic and Raviart (1987)). In the next section we show that also the convergence of the SPH method depends on an analogous requirement. For the highest ratios $R_d/\Delta r = 6$ the

saturation level of about 10^{-4} is reached very soon and the error E_ω is mainly dominated by the factor ξ. Figures 7.2(b) shows E_ω for three different values

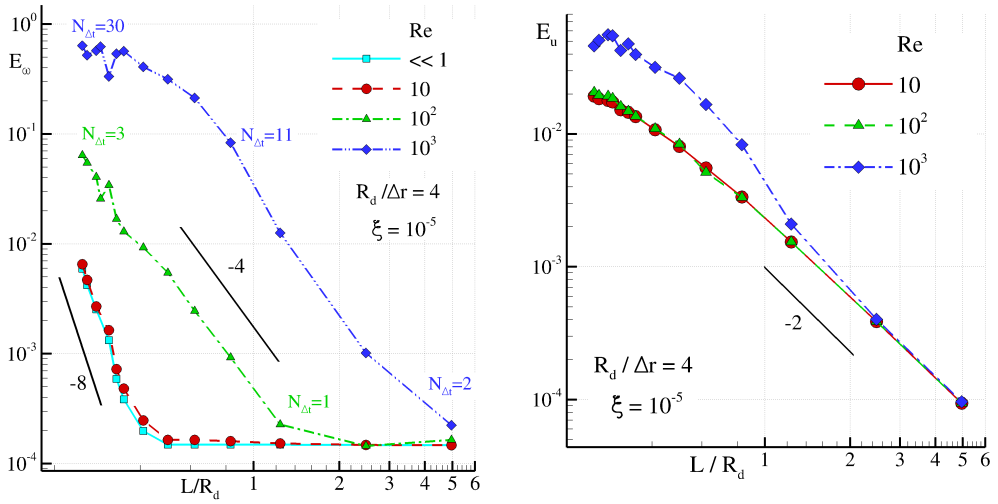

(a) (b)

Figure 7.3: Maximum relative error over vorticity (7.3(a)) and over velocity (7.3(b)) as functions of L/R_d for various Reynolds numbers and fixed ratio $R_d/\Delta r$.

of ξ: 10^{-3}, 10^{-5} and 10^{-7} with fixed $R_d/\Delta r = 5$. It is straightforward to note that the saturation level decrease with ξ so that we can expect a convergence to the exact solution if we simultaneously decrease $\Delta r/R_d$ and ξ.

Figure 7.3(a) and 7.3(b) shows the relative errors E_ω and E_u for Re numbers: 10, 100, 1000 with fixed $R_d/\Delta r = 4$ and $\xi = 10^{-5}$. For E_ω the case without advection ($Re \ll 1$) is also shown for comparison. As expected E_ω increases with Re, due to the errors linked to the advection steps, in particular for Re equal 10 the errors are practically the same of the case $Re \ll 1$ (convergence rate equal about to 8) while for Re equal to 1000, the saturation of E_ω is no more visible in the adopted spatial resolution range and the convergence rate reduces to about 4. Furthermore, for Re=1000, the $L/\Delta r$ range covered by the first regime become quite wider with respect to the low Reynolds number cases, this means that a large number of vortices is now needed (about 10^5) to reach an error level $E_\omega < 10^{-3}$. Regarding the errors on the velocity field, E_u, these are higher than E_ω, however E_u shows an almost constant convergence ratio of about 1.8 for all the three Re numbers, without any reduction due to saturation error level.

Using equations (4.95), (4.97) and (4.98) a link between the ratio $N_{\Delta t}$ and Reynolds number can be derived:

$$N_{\Delta t} = \left[\frac{(R_d/\Delta r)^2}{4Co \ln(1/\xi)} \frac{1}{L/\Delta r} \right] Re\,, \tag{7.7}$$

therefore, fixing $R_d/\Delta r$ and the resolution $L/\Delta r$, we must perform, for every diffusive step, $N_{\Delta t}$ advection steps cumulating errors as $N_{\Delta t}$ increases. Indeed, if $N_{\Delta t}$ is large enough, as in the case $Re = 1000$, where $N_{\Delta t}$ is equal to 30 for the lowest resolution, irregularities in the vortex particles distribution become quite visible.

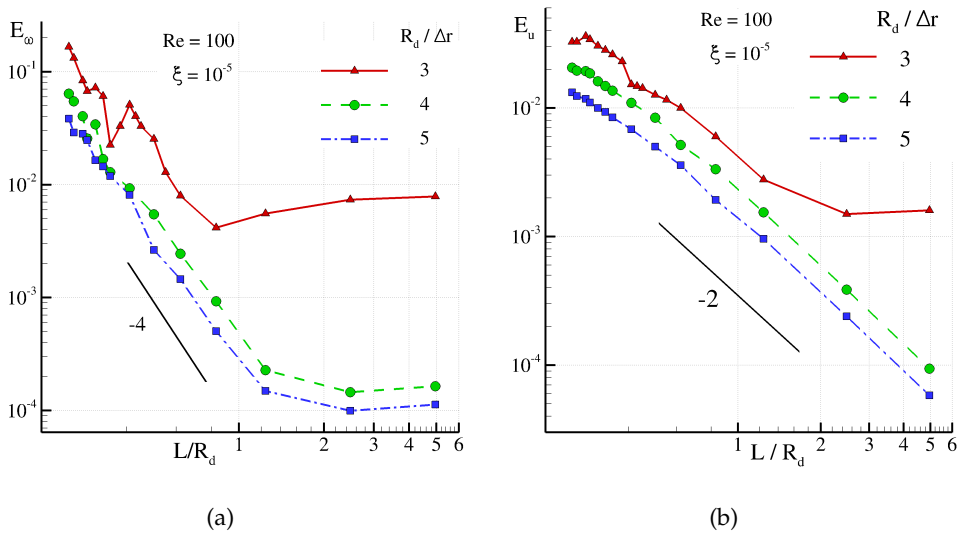

(a) (b)

Figure 7.4: Maximum relative error over vorticity (7.4(a)) and over velocity (7.4(b)) as functions of L/R_d for various ratio $R_d/\Delta r$ and fixed Reynolds numbers

Figure 7.4(a) and 7.4(b) show E_ω and E_u for three different values of $R_d/\Delta r$: 3, 4 and 5, fixed $Re = 100$ and $\xi = 10^{-5}$. As previously shown for the case $Re \ll 1$, convergence with $R_d/\Delta r$ is obtained also here in the presence of advection steps. For the lowest ratio $R_d/\Delta r = 3$ saturation is visible for both E_ω and E_u.

Summarizing, given the Reynolds number, accurate results require the right combination between spatial resolution $L/\Delta r$ and $R_d/\Delta r$ (linked to the number of nodes inside the diffusive support). A good combination can be obtained through equation (7.7) by reducing $N_{\Delta t}$ as much as possible.

Numerical Results for SPH

In this section the SPH model is tested on the Lamb-Oseen vortex problem. This problem can be demanding for this particle method since it is mainly dominated by the viscous forces. Since SPH is based on low order integral interpolation formula (see *e.g.* Quinlan et al. (2006)) the error on second order operators is quite sensitive to the particle disorder. To limit this error, the number of particles inside the support of δ_ε, needs to be large enough (see Quinlan et al. (2006), Colagrossi et al. (2013), Fatehi and Manzari (2011)). We underline that, in the SPH model, the smoothed length 2ε is equivalent to the

radius R_d used in the DVH. Therefore to check the accuracy of the numerical solution as well as the convergence of the SPH scheme different tests changing the spatial resolution $L/(2\varepsilon)$ and the ratio $2\varepsilon/\Delta r$ are performed.

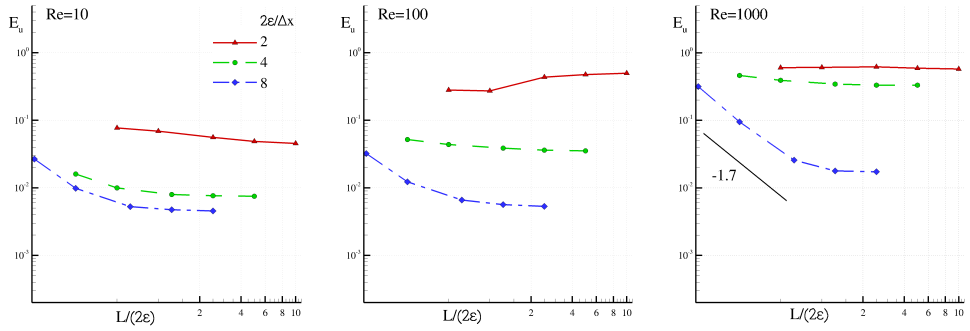

Figure 7.5: SPH simulations: Error on the velocity field E_u for the Lamb-Oseen problem for three different Reynolds numbers and using three different ratios $2\varepsilon/\Delta r$.

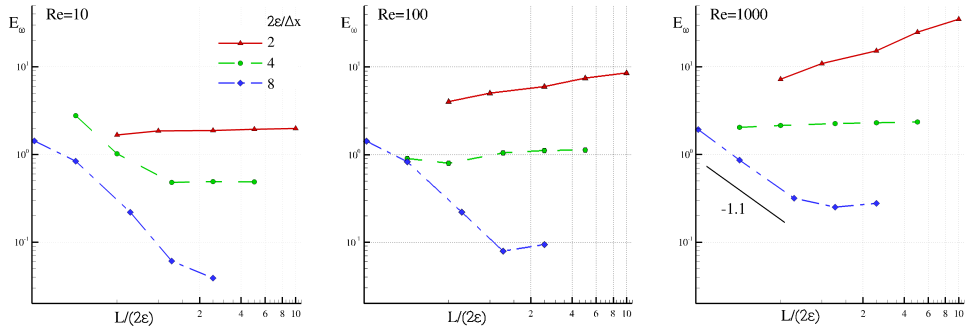

Figure 7.6: SPH simulations: Error on the vorticity field E_ω for the Lamb-Oseen problem for three different Reynolds numbers and using three different ratios $2\varepsilon/\Delta r$.

Figure 7.5(a) shows the relative errors E_u (see eq. (7.6)) on the velocity field for the smallest Reynolds number (Re=10). For this case a relative error of order 10^{-2} is measured using $2\varepsilon/\Delta r = 4$ and 8 while, using only 9 interacting particle neighbours (*i.e.* $2\varepsilon/\Delta r = 2$), the error is 10^{-1}. Further, a small convergence rate is always obtained and a saturation level is quite visible for the two highest ratio $2\varepsilon/\Delta r$. The results are in line with the analysis performed in Quinlan et al. (2006) indeed, as it is well known in the SPH literature, the method converges when both Δr as well as $\Delta r/\varepsilon$ simultaneously go to zero (see *e.g.* Di Lisio et al. (1998)). However, the results show also that a reduction

of both Δr and $\Delta r/\varepsilon$ is not enough to get convergence to the analytical solution. This can be related to the shape of the kernel δ_ε, as showed for the DVH; however this aspect has not been investigated in this work. With respect to DVH, considering the same spatial resolution $L/\Delta r$ and the same N_{node} (i.e. $R_d = 2\varepsilon$), the SPH errors on E_u are almost two order of magnitude greater.

Increasing the Reynolds number, E_u increases, and for Re=1000 (see figure 7.5(c)), this error is always greater than 10^{-2} for all the simulations performed, while with DVH this error still remains of order 10^{-4} for the highest resolution.

In the SPH method vorticity is not a primary variable and to evaluate this field a further integral interpolation is needed through the formula:

$$\rho\omega(r_i) = \sum_j (u_j - u_i) \times \nabla W_j(r_i)\, m_j \tag{7.8}$$

Therefore, larger errors on ω are expected with respect to that on velocity. This is confirmed by the results depicted in figures 7.6(a), 7.6(b) and 7.6(c) where E_ω is one order of magnitude larger that E_u (see figures 7.5(a), 7.5(b) and 7.5(c)). In particular for Re=100 and 1000 the error E_ω is even always divergent when using the smallest ratio $2\varepsilon/\Delta r$.

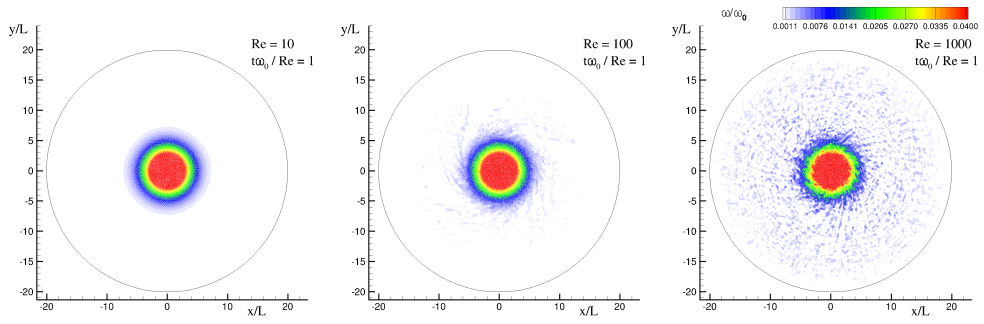

(a) (b) (c)

Figure 7.7: SPH simulations: Vorticity field at time $t = \omega_0/Re$ for the Lamb-Oseen problem for three different Reynolds numbers.

Figure 7.7 shows the vorticity field at the end of the simulations for the highest spatial resolution $L/(2\varepsilon)$ and the highest $2\varepsilon/\Delta r$ ratio, for the three Reynolds numbers analysed: 10, 100, 1000. From those plots it is quite visible that increasing Re spurious numerical vorticity starts to form inducing errors in the numerical solution. The development of this "numerical turbulence" and its connection to extra-dissipation mechanism has been already commented in Colagrossi et al. (2013) in the context of viscous gravity waves. In figure 7.8(a) the time history of the SPH kinetic energy for Re=1000 is compared with the analytical one; at the end of the simulation SPH has dissipated about 10%

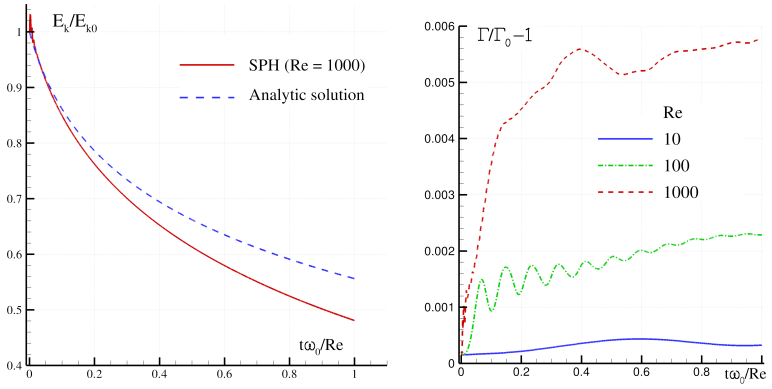

(a) (b)

Figure 7.8: SPH simulations: Time histories of the kinetic energy E_k and the total circulation Γ for the Lamb-Oseen problem for three different Reynolds numbers.

more energy than one expected. Figure 7.8(b) displays the time history of total circulation, Γ, for Re=1000 the errors on the conservation of Γ starts to become non-negligible going beyond 0.5% (regarding the conservation of circulation in SPH method see also Antuono et al. (2013)).

Despite this drawback on the evaluation of the vorticity field, the SPH method has the advantage of a direct evaluation of the fluid deformation due its pure lagrangian nature. Figure 7.9 shows the fluid deformation at the end of the simulation $t\omega_0 = Re$ for the three Reynolds number considered. In all the three cases the same amount of vorticity is damped, however, from these snapshots, it is quite visible the increasing relevance of the advection transport with the Reynolds number. The direct control of the fluid deformation can be quite useful for many applications. For example, on the two particle sets highlighted in figure 7.9 it is easy to give different fluid properties (few changes are needed) with SPH; while this operation it is generally not straightforward using vortex methods.

For example, the results showed in figure 7.10 refers to a case where two different fluids are used. The Reynolds number of the first fluid is $Re_1 = \pi\omega_0 L^2/\nu_1 = 10^4$ while the second fluid has a Reynolds number which change in time, starting with the same $Re_2(t = 0) = Re_1$ and decreasing linearly in time reaching a value one thousand time lower at a fixed time t_0, $Re_2(t_0) = \pi\omega_0 L^2/\nu_2 = 10$:

$$Re(t) = \begin{cases} Re_1 + (Re_2 - Re_1)\dfrac{t}{t_0} & t < t_0 \\ Re_2 & t \geqslant t_0 \\ t_0 = 2\,Re_2\,/\,\omega_0; & Re_1 = 10^4, \qquad Re_2 = 10 \end{cases} \tag{7.9}$$

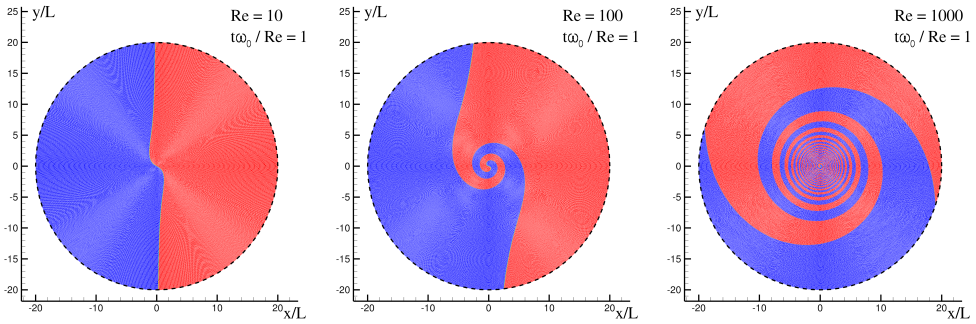

(a) (b) (c)

Figure 7.9: SPH simulations: Fluid deformation for the Lamb-Oseen problem for three different Reynolds numbers. Particles coloured in blue were initially positioned on $x < 0$ semi-plane while red particle belonged to $x > 0$ at $t = 0$.

Because of this change in the viscosity of the second fluid the vorticity field becomes more complicated than the one presented for the Lamb-Oseen problem. Indeed, vorticity is generated by the interaction between the fluids and also negative values develop (see right plot of figure 7.10). This is just an example to show the flexibility of the SPH respect to a Vortex Method. Even if the DVH allows to get more accurate results with lower CPU costs it is important to underline the advantages of the SPH method like in this simple example just discussed, for which the DVH scheme requires complex changes in the model while for the SPH the modifications are practically trivial (for SPH simulations of multi-fluids dynamics see also Tofighi and Yildiz (2013)).

7.2 MERGER OF A PAIR OF CO-ROTATING VORTICES

After the simple dynamics of an isolated vorticity patch discussed in the previous section, the more complex behaviour of a merger of a pair of co-rotating vorticity patches in considered here. At large Reynolds numbers, the dynamics of the merging process is not significantly influenced by the vorticity diffusion, the phenomenon is almost driven by the advection term while the diffusion process has a secondary role and could be relevant only for very low Reynolds numbers.

In the first snapshot of figure 7.11 the initial conditions of the problem are shown. The vorticity is equal to ω_0 inside two circular regions of radius R and zero elsewhere. The total circulation of each patch at $t = 0$ is equal to $\Gamma_0 = \pi R^2 \omega_0$, the Reynolds number for this problem is defined as $Re = \Gamma_0/\nu$ and it is set equal to 18850, in order to get a low-viscosity evolution (for more details see Graziani et al. (1995)). The results presented in figure 7.11 show the vorticity

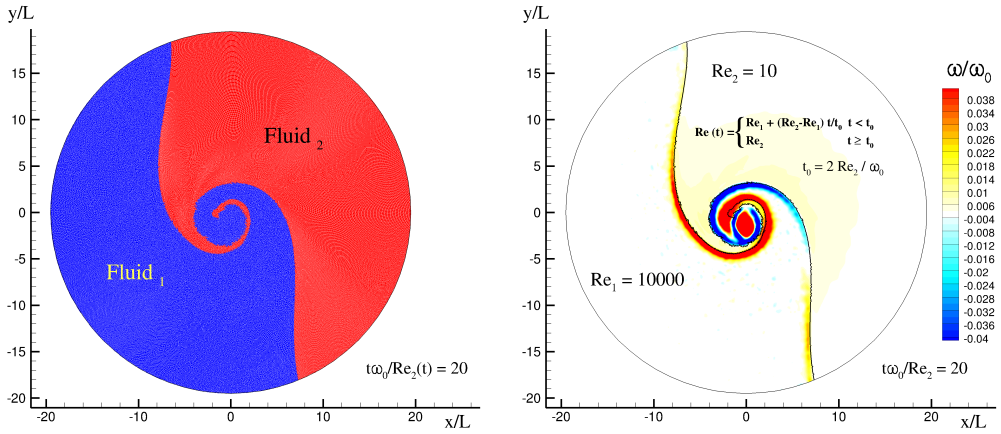

Figure 7.10: SPH simulations: Mixing of two fluids with different viscosity initialized with the Lamb-Oseen velocity-pressure fields. Left: Fluid Deformations: in blue Fluid-1 initially positioned on $x < 0$ semi-plane. In red Fluid-2 particles initially positioned on to $x > 0$ semi-plane. Right: Vorticity field at time $t\omega_0 / Re_2 = 20$.

evolution obtained by DVH model using a spatial discretization $R/R_d = 50$ ($R_d/\Delta r = 4$, $\xi = 10^{-5}$) which corresponds to a number of vortex particles equal to about 251.000. At the end of the simulation, because of the diffusion process, the number of the vortex particles is about 2 millions. The two initial vortical regions are highly stretched while rotating around the origin of the

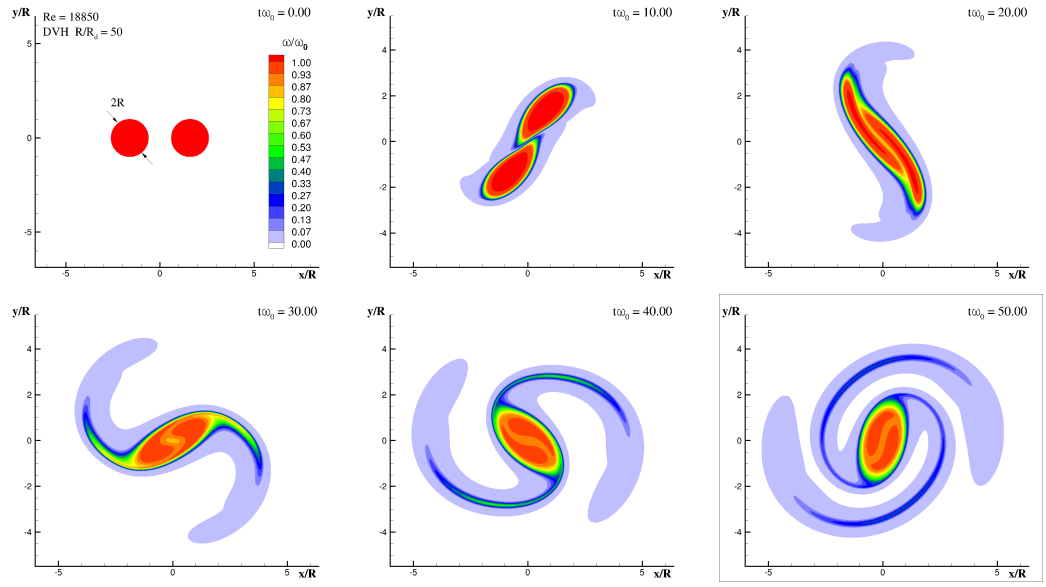

Figure 7.11: Merging of a pair of co-rotating vorticity patches: Vorticity field evolution using DVH solver

axis. At time $t\omega_0 = 30$ the two patches are almost merged while two thin vortical structures are shed. To capture the latter the spatial resolution needs to be properly selected. For such complex evolution an analytical solution is not possible to be obtained, however, in order to assess the validity of the DVH model and to monitor the accuracy of the solutions, some first integrals of motion involving global quantities can be computed:

- total circulation: $\Gamma = \int_\Omega \omega \, dx$,
- second vorticity moment: $\mathcal{I} = \int_\Omega r^2 \, \omega \, dx$,
- enstrophy: $\mathcal{S} = 1/2 \int_\Omega \omega^2 \, dx$,
- excess energy $\mathcal{E} = 1/2 \int_\Omega \omega \, \psi \, dx$,

being ψ the stream function. For the present DVH the conservation of the total circulation Γ is in practice always preserved (relative errors less than 10^{-6} since we use a non null Γ_{cutoff}, see section 4.6). For the problem studied here (2D unbounded without free-stream velocity), the following relations between Γ, $\mathcal{I}$, $\mathcal{S}$ and $\mathcal{E}$ hold (see *e.g.* Riccardi and Durante (2006)):

$$\frac{d\mathcal{I}}{dt} = \frac{4\Gamma_0}{Re}\Gamma(t)\,, \qquad \frac{d\mathcal{E}}{dt} = -\frac{2\Gamma_0}{Re}\mathcal{S}(t) \tag{7.10}$$

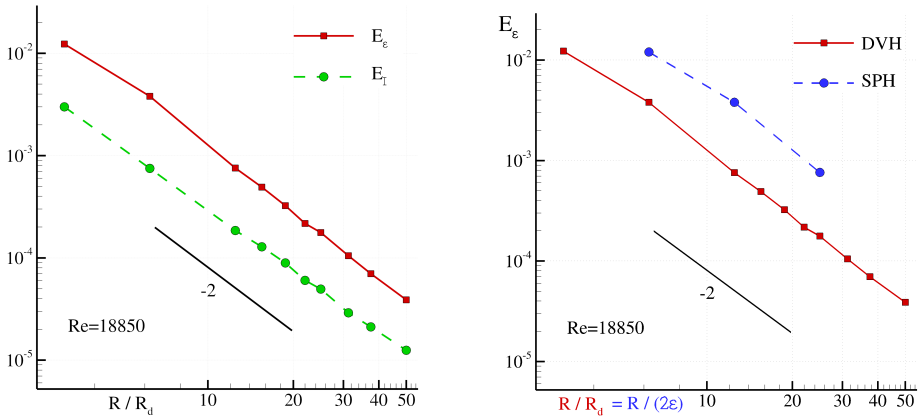

Figure 7.12: Merging of a pair of co-rotating vorticity patches. Left: errors $E_\mathcal{I}$ and $E_\mathcal{E}$ (see eq. (7.11)) as a function of the spatial discretization $R/\Delta r$. Right: errors $E_\mathcal{E}$ comparison between DVH and SPH results

Therefore, the accuracy of the numerical models (DVH and SPH) can be inferred by computing the relative errors:

$$\begin{cases} E_{\mathcal{I}} = \max\limits_{t\in(0,t_{end}]} \dfrac{\mathcal{I}(t) - \mathcal{I}_0 - \frac{4\Gamma_0}{Re}\int_0^t \Gamma(\tau)d\tau}{\mathcal{I}_0} \\ E_{\mathcal{E}} = \max\limits_{t\in(0,t_{end}]} \dfrac{\mathcal{E}(t) - \mathcal{E}_0 + \frac{2\Gamma_0}{Re}\int_0^t \mathcal{S}(\tau)d\tau}{\mathcal{E}_0}. \end{cases} \tag{7.11}$$

Left plot of figure 7.12 shows the convergence trend of the errors $E_{\mathcal{I}}$ and $E_{\mathcal{E}}$ obtained by DVH model. An almost second order convergence is achieved for both the errors as a function of the spatial discretization R/R_d. On the right plot of the same figure the SPH results for $E_{\mathcal{E}}$ are shown as a function of the spatial discretization $R/(2\varepsilon)$. Since the two ratios $R_d/\Delta r$ and $2\varepsilon/\Delta r$ are both equal to 4, the two different resolutions, R/R_d for the DVH model, and $R/(2\varepsilon)$ for the SPH, can be considered equivalent (same $R/\Delta r$). As expected the SPH error level is higher than the DVH one, however the second order convergence is achieved also by this solver.

Regarding $E_{\mathcal{I}}$, the SPH presents a larger error without any reduction for increasing resolution $R/(2\varepsilon)$, as reported in the left plot of figure 7.13. This is mainly due to development of spurious vorticity in the whole domain (see right plot of figure 7.13). Even if this vorticity amount is very limited the r^2 factor inside the definition of $\mathcal{I}$ amplifies its effect. The development of this numerical vorticity by the SPH method is widely documented in the literature (see *e.g.* Colagrossi et al. (2013) and Ellero et al. (2010)) and can be controlled by increasing the ratio $\varepsilon/\Delta r$.

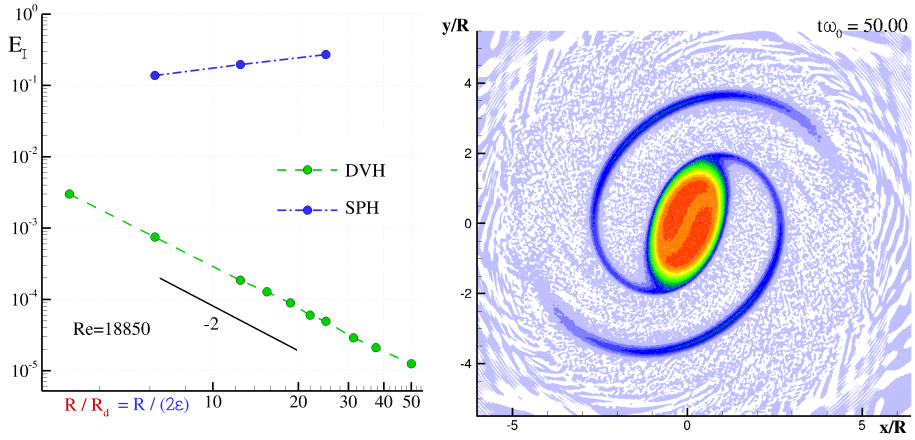

Figure 7.13: Merging of a pair of co-rotating vorticity patches Left: errors $E_{\mathcal{I}}$ comparison between DVH and SPH results. Right: vorticity field at $t\omega_0 = 50$ using the SPH solver.

We underline that in order to solve this problem with the SPH, a couple of Poisson problems have been solved using a semi-analytical approach, to get,

from the initial conditions on the vorticity field, the velocity-pressure fields at $t = 0$ needed by the SPH solver. A circular domain of radius 10R has been discretized for the SPH method using the same technique discussed in section 7.1 for handling the outer boundary. The highest adopted spatial resolution was $R/(2\varepsilon) = 25$ corresponding to a number of particles of about 3 millions. When using DVH model simulations up to a spatial resolution $R/(2\varepsilon) = 50$ were possible, thanks to the discretization of the rotational portion of the fluid domain only, allowing also to simulate a last case with Reynolds number equal to 100000 (see last plot in figure 7.14).

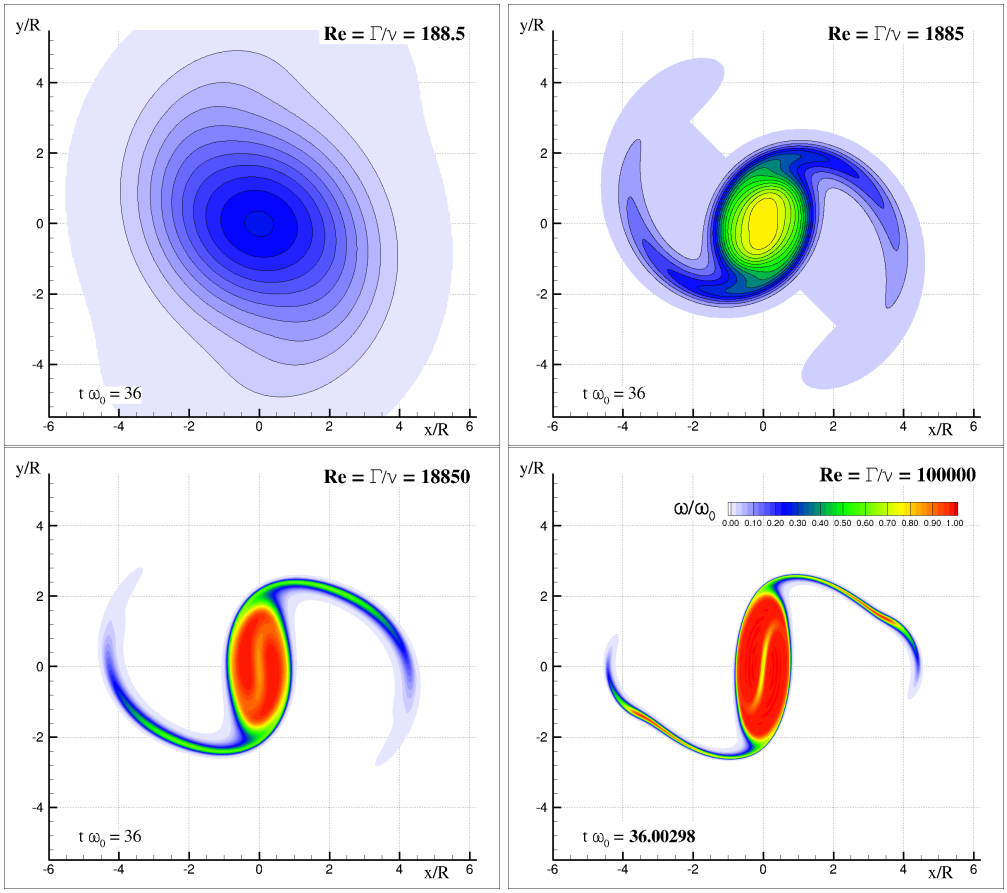

Figure 7.14: Merging of a pair of co-rotating vorticity patches. Effect of the Reynolds number on the vorticity field at $t\omega_0 = 36$ using the DVH solver.

Finally, figure 7.14 shows the vorticity field at time $t\omega_0 = 36$ obtained with the DVH method, using four different Reynolds number starting from Re=188.5 up to Re=100000. It is just an example to show the ability of the DVH in simulating problems for a wide range of the viscosity scales. For the most viscous case the vorticity has been diffused over a big portion of the computational domain already at $t\omega_0 = 36$ while for the highest Reynolds number the enstrophy is still close to 90% of its initial value. The two branch

filaments originated during the merging process become thinner and thinner as the Reynolds increase and the vorticity maintains values very close to the initial one inside these regions which become more persistent during the time evolution.

A plot of the enstrophy for the Reynolds number starting from Re=188.5 up to Re=100000 is showed in figure 7.15. As expected the enstrophy decays faster for the lowest Reynolds number.

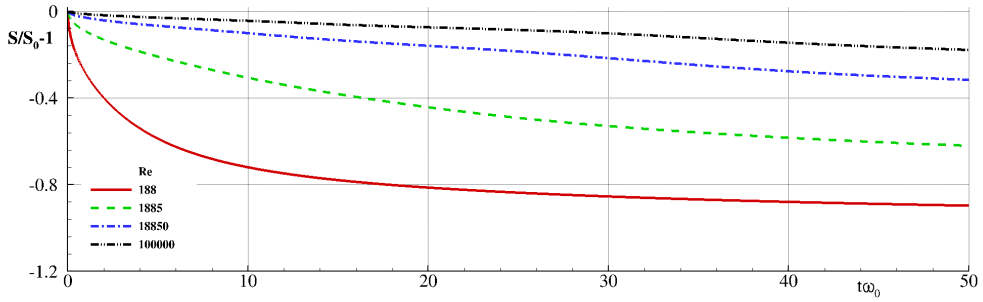

Figure 7.15: Merging of a pair of co-rotating vorticity patches. Effect of the Reynolds number on the enstrophy.

8 VORTICITY FLOW IN PRESENCE OF BLUFF BODIES

In this section the DVH model is tested by studying flows past solid bodies of various shapes at different Reynolds numbers.

The simulations are performed using a multi resolution approach: the spatial resolution is decreased for increasing distance from the body in the flow direction, in particular this is done using several RPDs with decreasing values of $L/\Delta r$ as shown in Fig. 8.1. The first RPD (*i.e.* the one nearest to the body) is

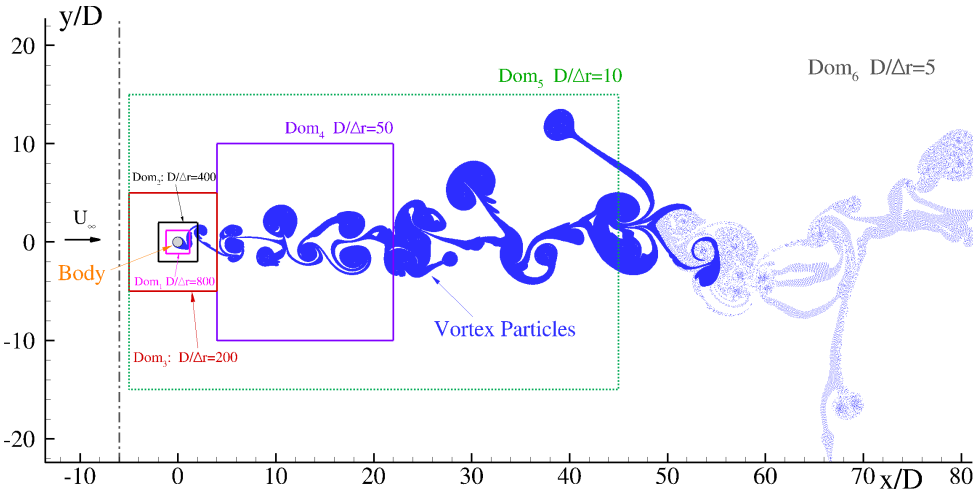

Figure 8.1: Example of a multi-domain simulation using 6 different RPDs.

generated using the procedure described in section 6.

A first series of simulation is made (section 8.1) to study the flow past a thick elliptical cylinder at $Re = 500$, in this case a convergence test is shown. The DVH solution is then compared with another particle method, the Smoothed Particle Hydrodynamics (SPH), using the numerical model described in Marrone et al. 2013 and in Macià et al. 2011.

In section 8.2 the flow past a thin (axis ratio 0.1) elliptical cylinder with angle of attack $\alpha = 30°$ is studied using Reynolds numbers ranging from 100 to 1000.

In section 8.3 and 8.4 the flow past two different elliptical cylinders with angle of attack $\alpha = 30°$ at $Re = 3000$ and $Re = 10000$ respectively is simulated. The results are compared with those presented in the literature (see Nair and Sengupta (1997), Huang and Huang (2013)).

Because the present DVH method is able to perform simulations using bodies of general shape, the flow past a body having a C-shape form is simulated at $Re = 2000$ for various angles of attack, the results are shown in section 8.5.

In section 8.6 the flow past a circular cylinder is simulated for $Re = 9500$, the obtained results are compared with the available data (see Koumoutsakos and Leonard (1995)).

In section 8.7 the flow past a circular cylinder is simulated for Reynolds numbers equal to 5×10^4 and 10^5. This last simulation requires a very high spatial resolution in the boundary layer region, for this purpose eight RPDs are used. Even if this is a 2D simulation, for our knowledge is, at the time of writing, the flow around a circular cylinder with highest Reynolds number simulated in the literature without using any subgrid-scale turbulence model.

The results described in this section are also presented in Rossi et al. (2014b)

8.1 INCLINED ELLIPTICAL CYLINDER $Re = 500$

A series of simulations of an elliptical cylinder with axis ratio 0.4 and angle of attack $\alpha = 20°$ is performed at $Re = 500$. An example of the evolution of the vorticity profile is shown in Fig 8.2(a) for $c/\Delta r = 200$ (being c the major axis). At this Reynolds and for the adopted thickness a regular harmonic shedding is reached after the transitory stage.

$c/\Delta r$	$Re_{\Delta r}$	Co	$\Delta t_a\, U/c$	$\Delta t_d\, U/c$ (Dom 1)
50	10	0.88	1.76×10^{-2}	7.05×10^{-2}
100	5	0.88	8.81×10^{-3}	1.76×10^{-2}
200	2.5	0.44	2.20×10^{-3}	4.41×10^{-2}

Table 8.1: Inclined elliptical cylinder $Re = 500$: main discretization parameters

Figure 8.2(b) shows the time histories for the drag coefficient c_d using three different spatial resolutions $c/\Delta r = 50, 100, 200$. Table 8.1 reports for each value of $c/\Delta r$: (i) the cell-Reynolds number $Re_{\Delta r} = U\Delta r/\nu$, (ii) the Courant number Co used for the advection time step. The low $Re_{\Delta r}$ values reached with the adopted resolution justify the good accuracy of the simulations performed in this first test-case.

The convergence ratio calculated, using a L_1 norm in time, is of about 2.0 in agreement with the analysis performed in section 7.

The same case is simulated with a Smoothed Particle Hydrodynamics method (Marrone et al. (2013)). Figures 8.3(a) and 8.3(b) depict respectively the drag and lift coefficient obtained with both methods with a spatial resolution $c/\Delta r = 200$. A good agreement between the two methods is obtained in the periodic regime. The differences on the transitory stage are mainly due to the weakly compressible approach of the SPH model where an impulsive start of the body originates a series of acoustic waves travelling and reflecting in the domain. The plot 8.3(b) shows that the lift coefficient oscillates around a positive value,

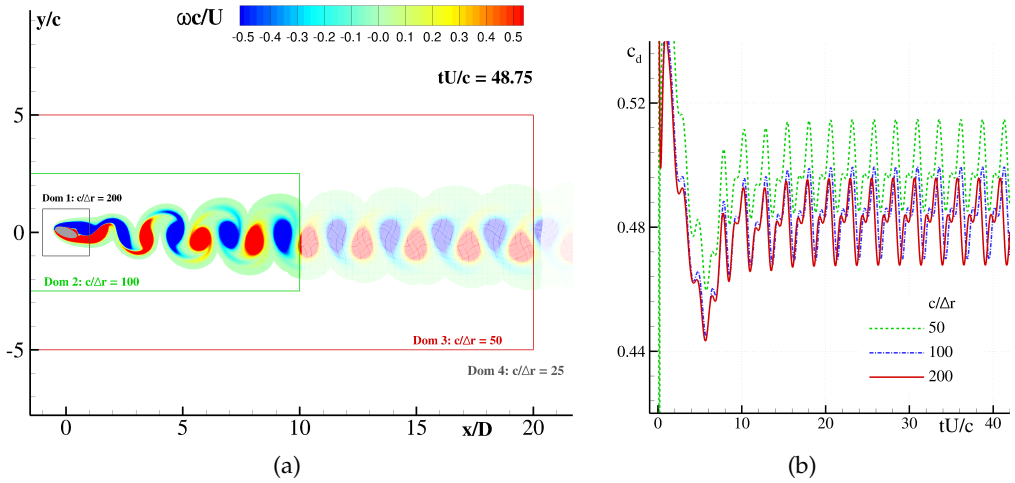

Figure 8.2: (a) Evolution of the vorticity field for $c/\Delta r = 200$ for an elliptical cylinder (axis ratio 0.4, $\alpha = 20°$) at $Re = 500$, (b) Drag coefficient for three different spatial resolutions $c/\Delta r$

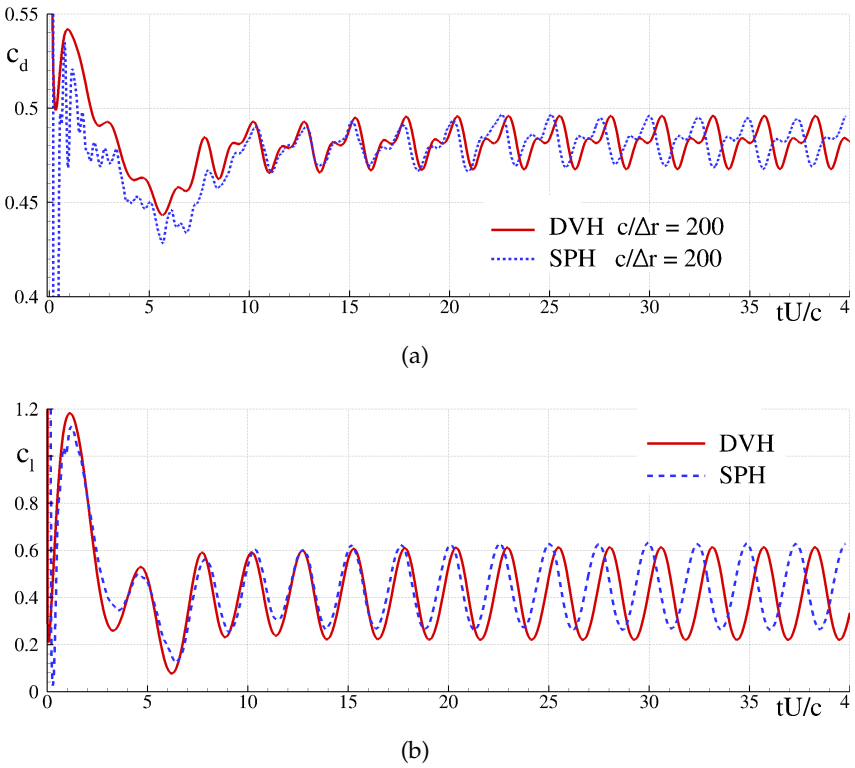

Figure 8.3: Time behaviour of drag (a) and lift (b) coefficient respectively for an elliptical cylinder (axis ratio 0.4, $\alpha = 20°$) at $Re = 500$: comparison between SPH and DVH.

as expected because of the small positive angle of incidence. The Strouhal number evaluated by the two different solvers is slightly different, this can be related to the confined domain used in the SPH simulation.

8.2 FLOW PAST THIN ELLIPTIC CYLINDER AT VARIOUS Re

The DVH algorithm is used to study the flow past a thin elliptic cylinder at various Reynolds numbers. The main discretization values are reported in table 8.2 while in figure 8.4 an example of the vorticity field generated at the various Re is showed.

Increasing the Reynolds number it is possible to see the transition from vortex structures resembling a von Karman vortex street for $Re = 100$ and $Re = 250$ to more complex vorticity distribution at the higher Reynolds. At $Re = 500$ a more complex behaviour of the vorticity structures appears in the wake with the formation of couples of vortices trying to travel upstream towards the body. At $Re = 1000$ the behaviour of the shed vortices changes again with the presence of couples of vortices travelling upwards, towards the limit of the computational domain, until their trajectories lead them back to interact with the rest of the wake.

Re	$c/\Delta r$	$Re_{\Delta r}$	Co	$\Delta t_a\, U/c$	$\Delta t_d\, U/c$ (Dom 1)
100	200	0.50	0.18	8.81×10^{-4}	8.81×10^{-4}
250	200	1.25	0.44	2.20×10^{-3}	2.20×10^{-3}
500	200	2.50	0.88	4.40×10^{-3}	4.40×10^{-3}
1000	200	5.00	1.76	8.81×10^{-3}	8.81×10^{-3}

Table 8.2: Flow around an elliptic cylinder with Reynolds number ranging from 10^2 to 10^3: main discretization parameters

The lift and drag coefficients for the various Reynolds numbers and the power spectrum of the lift coeffcient are showed in figure 8.5 and 8.6 respectively. As it is possible to see, varying Reynolds number, the force coefficients go from having an almost sinusoidal behaviour (Re=100) to a more complex one (Re=1000) although maintaining a very regular and periodic behaviour.

Figure 8.6 depict the lift coefficient power spectrum, the main frequency is related to the shedding of vortices from the body, incresing Reynolds number results in a variation of the main frequency and in the introduction of side frequencies related to the increased complexity of the vortex shedding.

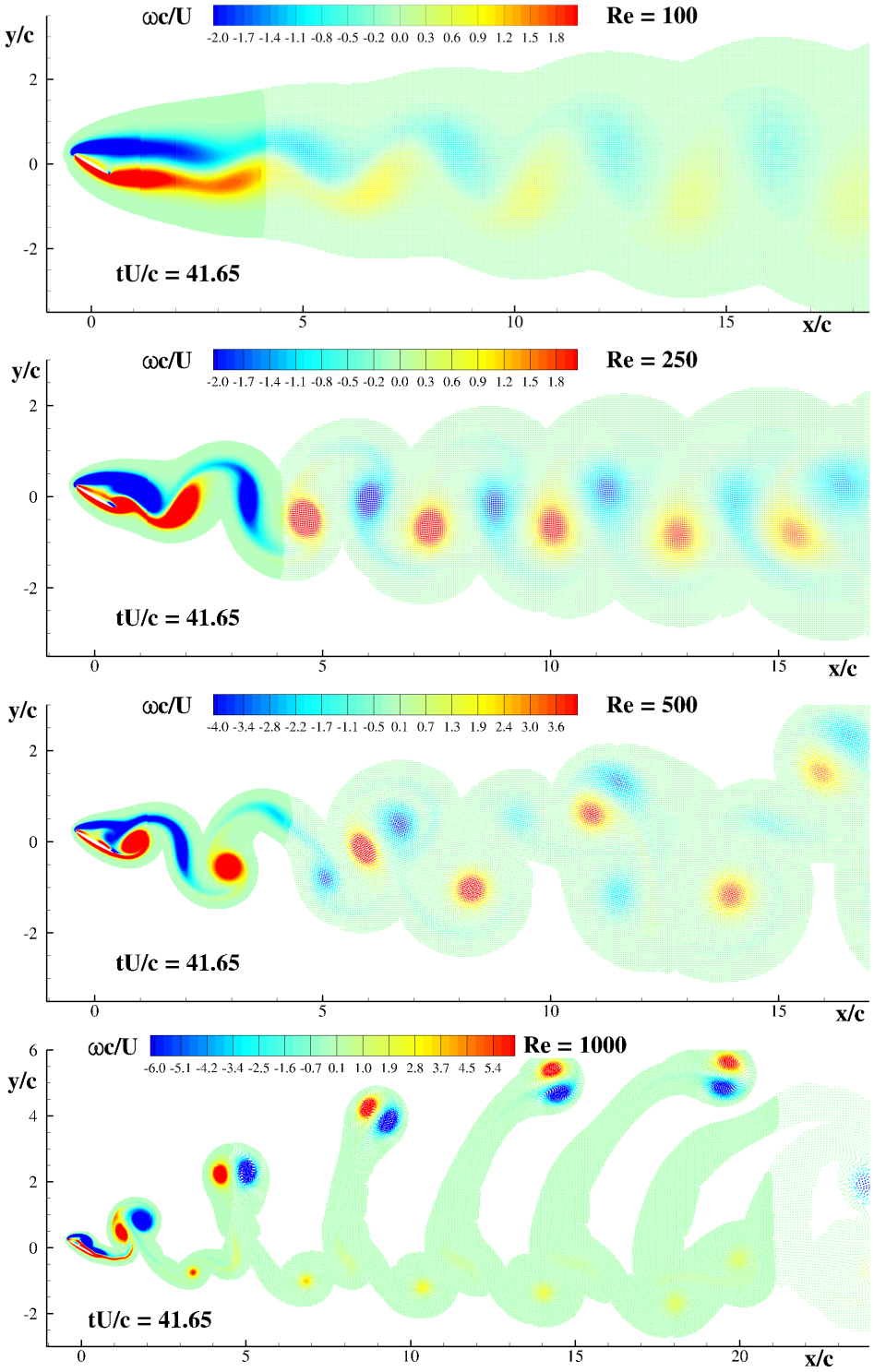

Figure 8.4: Example of the vorticity field generated at the various Reynolds numbers.

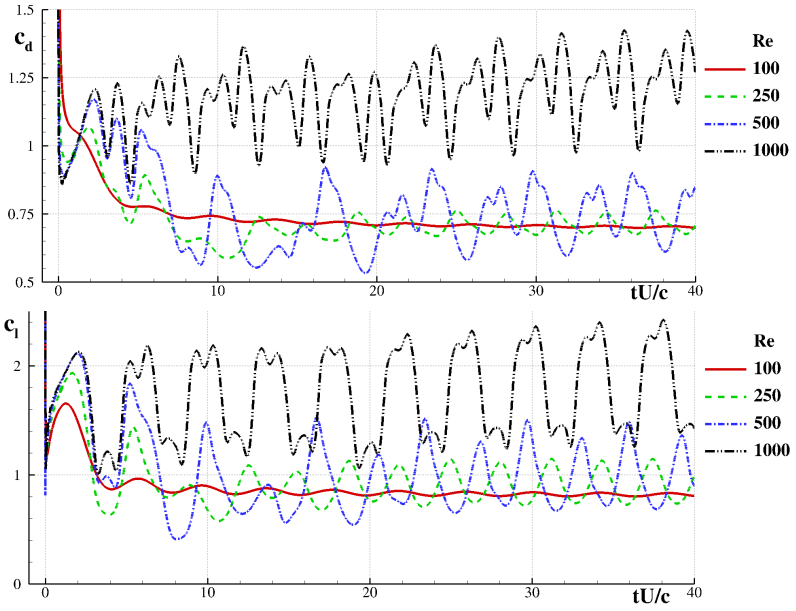

Figure 8.5: Elliptic cylinder (angle of attack $\alpha = 30°$ for various Re. Left: Drag coefficient. Right: Lift coefficient

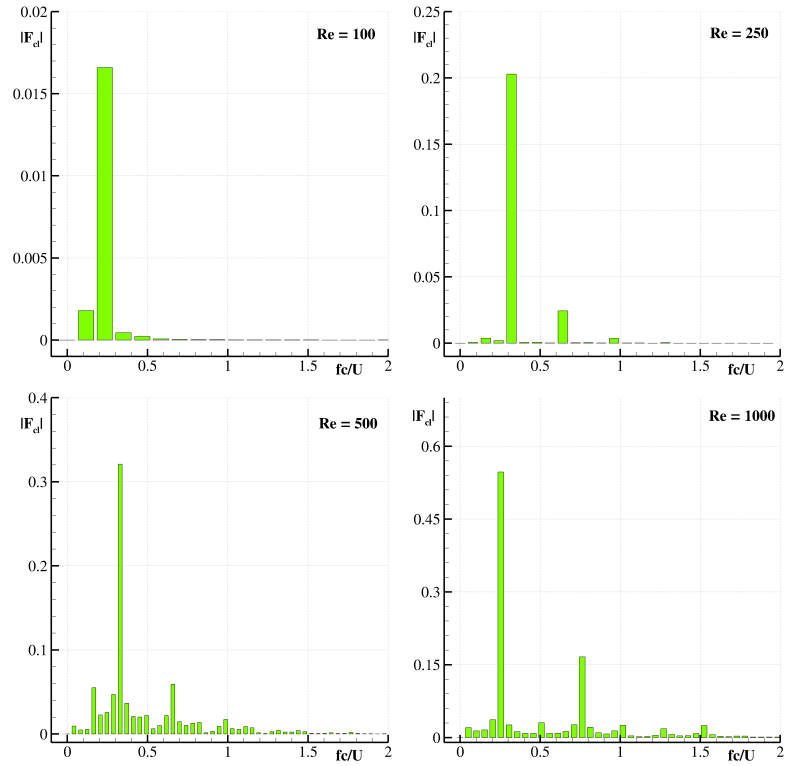

Figure 8.6: Lift coefficient powers spectrum for the four Reynolds numbers studied

8.3 FLOW PAST AN ELLIPTIC CYLINDER AT $Re = 3000$

Following the work of Nair and Sengupta (1997) a DVH simulation of the flow around a thin elliptical cylinder (thickness to chord ratio 0.1) with angle of attack $\alpha = 30°$ is here discussed. The same test case has been performed more recently by Huang and Huang (2013) and therefore also the related data are used to cross validate the DVH model.

In table 8.3 the main parameters of the spatial/time resolution adopted are shown. The ratio $c/\Delta r$ (being c the major axis) used close to the body is 800 allowing for an accurate solution of the boundary layer region. Figure 8.7

$c/\Delta r$	$Re_{\Delta r}$	Co	$\Delta t_a\, U/c$	$\Delta t_d\, U/c$ (Dom 1)
800	3.75	1.32	1.65×10^{-3}	1.65×10^{-3}

Table 8.3: Flow around an elliptic cylinder at Re = 3000: main discretization parameters

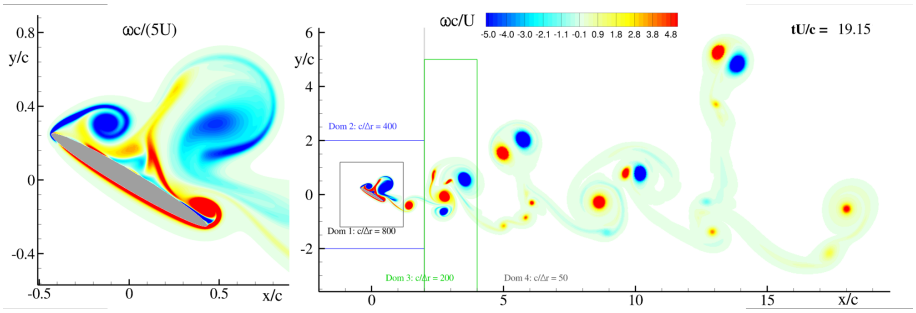

Figure 8.7: Evolution of the vorticity field for $c/\Delta r = 800$ for an elliptical cylinder (axis ratio 0.1, $\alpha = 30°$) at $Re = 3000$. Left: enlarged view close to the body. Right: wake field with the different domains used.

depicts the vorticity field in the near (left) and far (right) regions. The angle of attack used and the small thickness of the body induce a stall regime leading to a very complex wake dynamics.

Figure 8.8 reports the pressure coefficient around the ellipse for three different time instants. The pressure profiles have been compared with those evaluated in Nair and Sengupta (1997) showing a good agreement with the data produced by the DVH model.

A comparison for the drag and lift coefficients with the results reported in Nair and Sengupta (1997) and in Huang and Huang (2013) is depicted in figure 8.9. Both c_d and c_l coefficient oscillate around the same range of values for all the three sets of data, however the complexity of the vorticity field this time makes impossible to get a fair agreement between the different solutions.

The complexity of the evolution of the vorticity field can be better understood by looking at the power spectrum of the lift coefficient, where, together

with principal frequency, are present higher frequencies with lower intensities (up to a frequency of 0.3 Hz) possibly due to the complex detachment of the vorticity field from the ellipse. An example of the complex dynamic of the vorticity field near the body surface is given by the fast detachment of small vorticity structures (see figure 8.10), affecting both the lift and drag coefficient with fast oscillations.

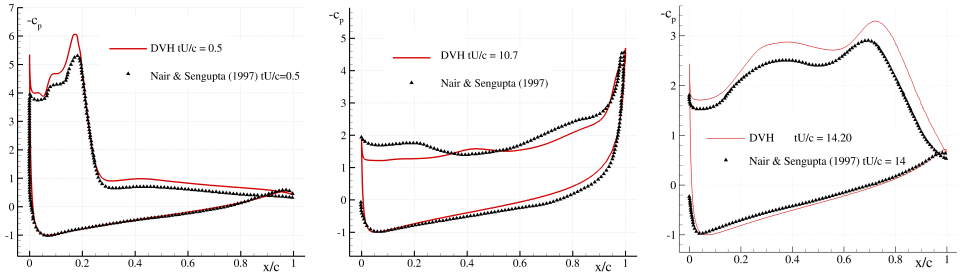

Figure 8.8: Pressure coefficients for a thin ellipse at Re = 3000 at different times: comparison between Nair and Sengupta (1997) and present study.

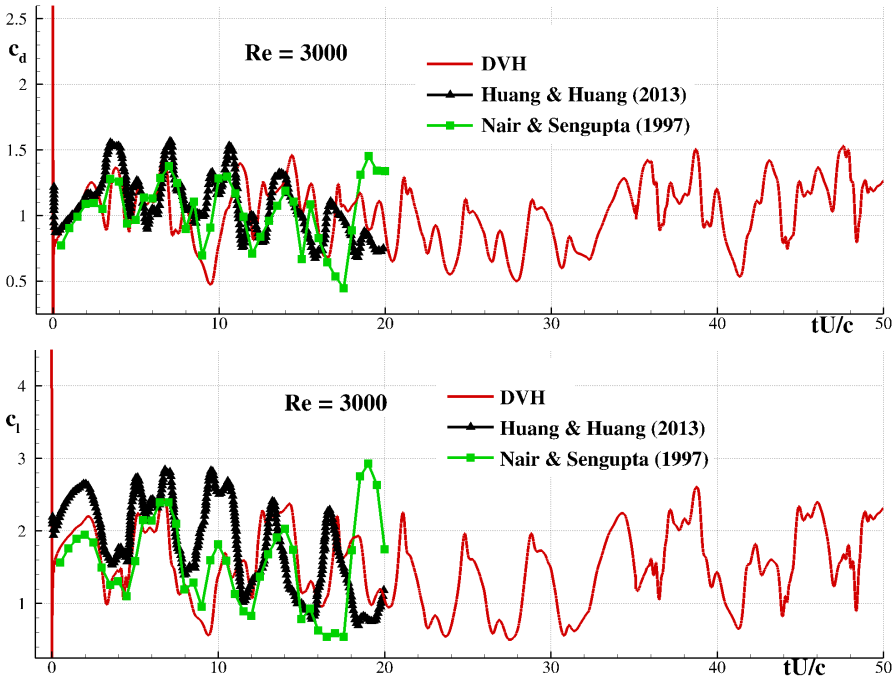

Figure 8.9: Drag (top) and lift (bottom) coefficients respectively for a thin ellipse at Re = 3000: comparison between Nair and Sengupta (1997), Huang and Huang (2013) and the present study

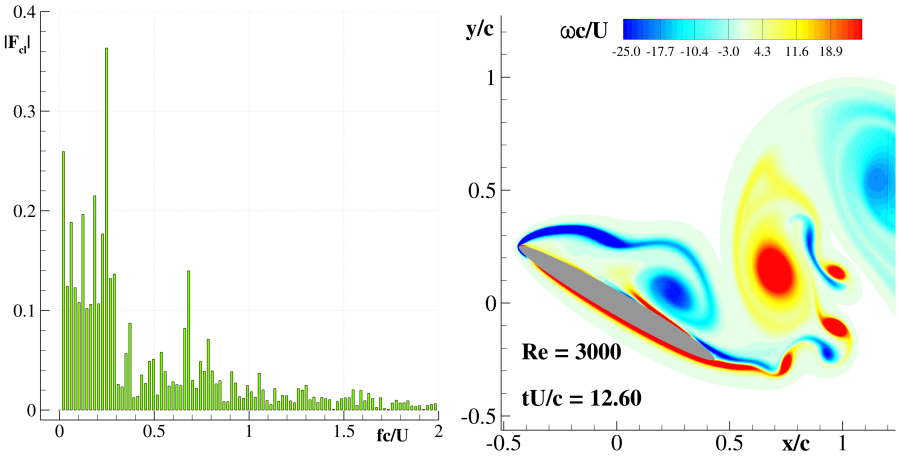

Figure 8.10: Left: Power spectrum of the lift coefficient. Right: Detachment of small vorticity structures from an elliptic cylinder at Re = 3000

8.4 FLOW PAST AN ELLIPTIC CYLINDER AT Re = 10000

Following the work of Nair and Sengupta (1997) a DVH simulation of the flow around an elliptic cylinder (thickness to chord ratio 0.25) with angle of attack $\alpha = 30°$ is here discussed.

In table 8.4 the main parameters of the spatial/time resolution adopted are shown. The ratio $c/\Delta r$ (being c the major axis) used close to the body is 1000 allowing for an accurate solution of the boundary layer region.

$c/\Delta r$	$Re_{\Delta r}$	Co	$\Delta t_a\, U/c$	$\Delta t_d\, U/c$ (Dom 1)
1000	10.0	1.76	1.76×10^{-3}	3.52×10^{-3}

Table 8.4: Flow around an elliptic cylinder at Re = 10000: main discretization parameters

Figure 8.11 depicts the vorticity field in the near (left) and far (right) regions. The angle of attack used induce also in this case a stall regime leading to a very complex wake dynamics.

A comparison for the drag and lift coefficients with the results reported in Nair and Sengupta (1997) is depicted in figure 8.12. Both c_d and c_l coefficient oscillate around the same range of values for both sets of data, however the complexity of the vorticity field this time makes impossible to get a fair agreement between the different solutions.

Small scale oscillations are clearly visible in the time evolutions of both the drag and lift coefficient, these oscillations are linked to the fast detachment of small vorticity structures from the body. This behaviour leads to a power spectrum for the lift coefficient in which the higher frequencies, although of small intensity, can not be neglected.

Figure 8.13 shows the power spectrum (left) of the lift coefficient for an impulsively started inclined ellipse at Re = 10000 and an example of the detachment (right) of small vorticity structures from the body surface.

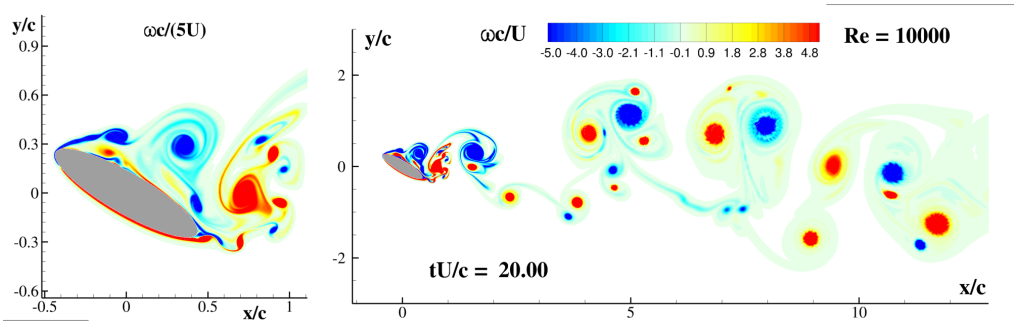

Figure 8.11: Evolution of the vorticity field for $c/\Delta r = 1000$ for an elliptical cylinder (axis ratio 0.25, $\alpha = 30°$) at Re = 10000. Left: enlarged view close to the body. Right: wake field.

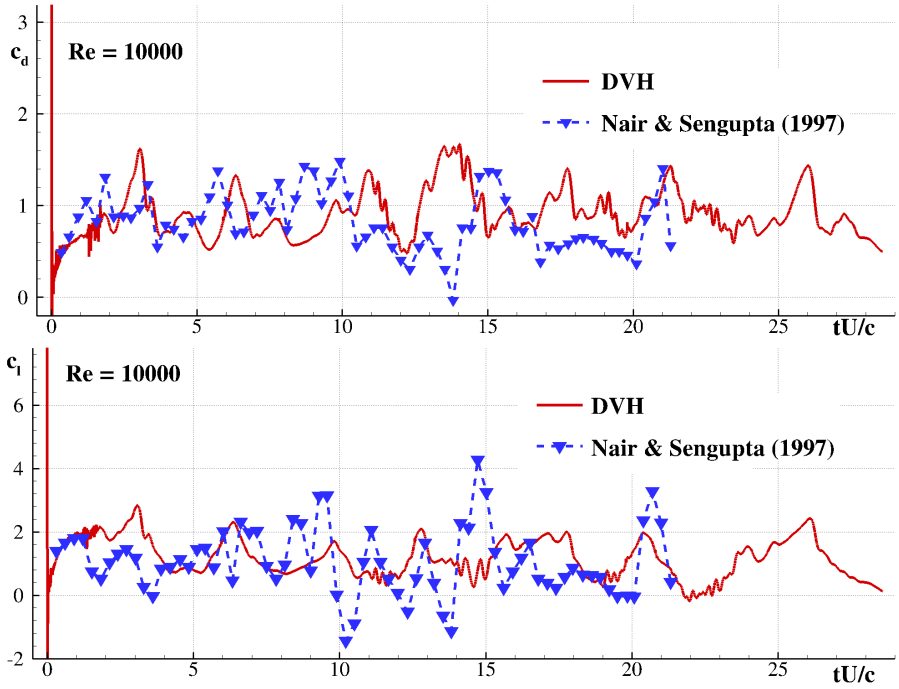

Figure 8.12: Drag (left) and lift (right) coefficients respectively for an ellipse at Re = 10000: comparison between Nair and Sengupta (1997) and the present study.

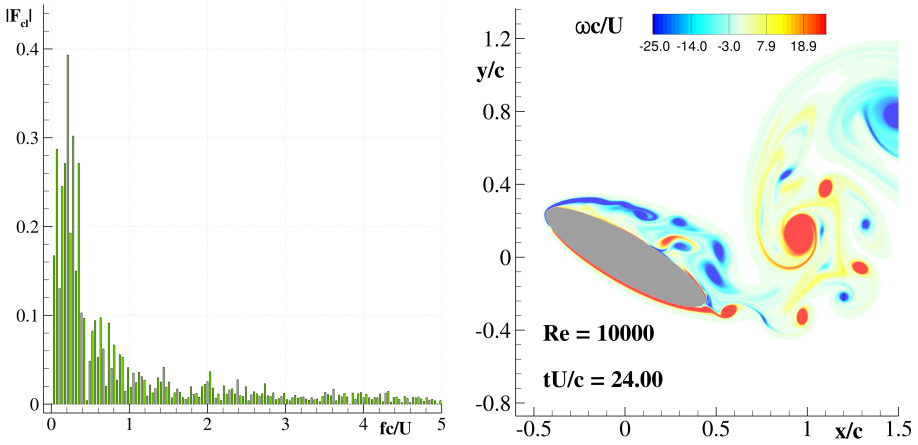

Figure 8.13: Left: Power spectrum of the lift coefficient. Right: Detachment of small vorticity structures from an elliptic cylinder at Re = 10000

8.5 FLOW AROUND A C-SHAPE BODY AT RE = 2000

The DVH method, thanks to the packing algorithm used to generate the RPDs described in section 6, allows for the simulation of viscous flows around body of general shapes. As an example, the flow around a smooth body composed by four semicircles with different radius (Fig. 8.14(a)) is here analysed. Different orientation changing the angles of attack α (Fig. 8.14(b)) are also considered.

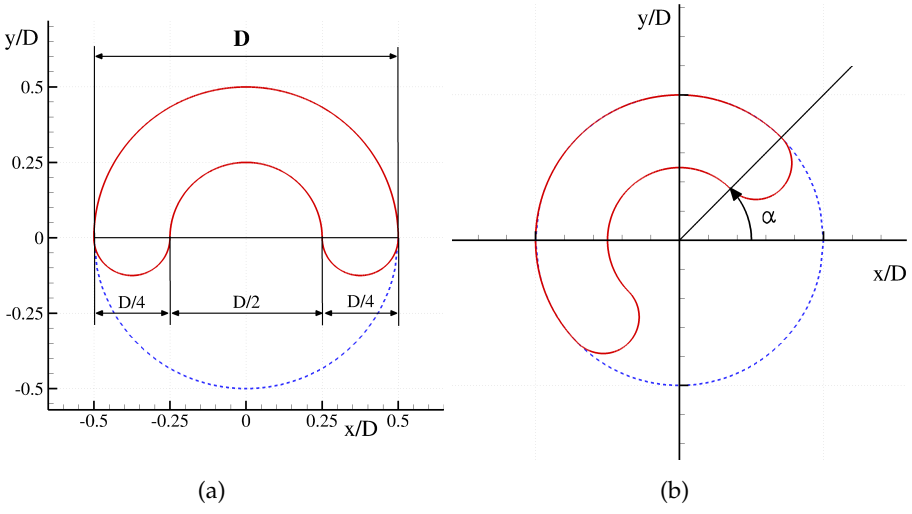

Figure 8.14: (a) Sketch of the C-shape body (b) Notation for the different rotations considered.

The Reynolds number assumed for this test-case is Re = 2000, while the angles of attack used are $\alpha = -90°, -45°, 0°, 45°, 90°$. Figures 8.15(a) and 8.15(b) show the time records for the drag and lift coefficients respectively for the first three angles $\alpha = -90°, -45°, 0$. For $\alpha = 0°$ the force reaches a periodic behaviour after the transition stage. Decreasing α the periodicity is lost and a quite irregular time behaviour develops, furthermore the level of the mean drag largely increases. The lift coefficient has a negative mean for $\alpha = 0°$, a positive mean value for $\alpha = -45°$ and a zero mean value for $\alpha = -90°$ as expected. The amplitude of the fluctuation on the lift force at $\alpha = -90°$ is comparable to that recorded for a circular cylinder at the same Re.

For positive angles of attack (figures 8.16(a), 8.16(b)) the mean drag increases with α, however, for $\alpha = 90°$ an almost periodic regime is reached again with a mean drag which is the highest recorded for all the five angles.

$D/\Delta r$	$Re_{\Delta r}$	Co	$\Delta t_a\, U/D$	$\Delta t_d\, U/D$ (Dom 1)
200	10.0	1.76	8.81×10^{-3}	1.76×10^{-2}

Table 8.5: Flow around a C-Shape body at Re = 2000: main discretization parameters

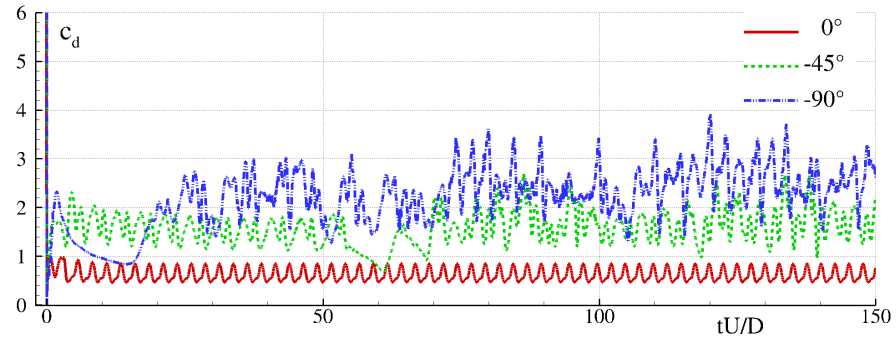

(a)

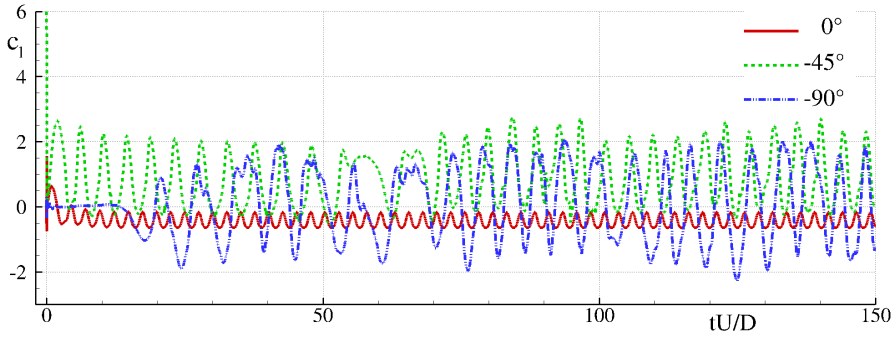

(b)

Figure 8.15: Drag (a) and lift (b) coefficients for a C-shape body at Re = 2000. Influence of the orientation: $\alpha = 0°, -45°, -90°$

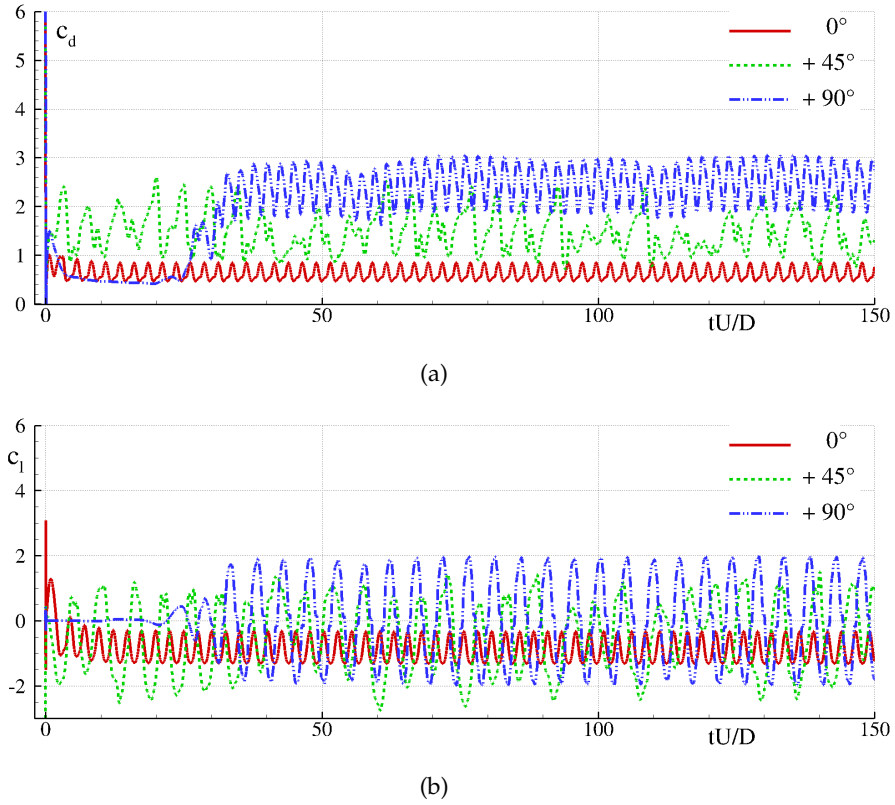

Figure 8.16: Drag (a) and lift (b) coefficients for a C-shape body at Re = 2000. Influence of the orientation: $\alpha = 0°, 45°, 90°$

What is really non intuitive from the results presented is the negative mean value of the lift coefficient for $\alpha = 0°$ and the high mean value of the drag coefficient for $\alpha = 90°$. Analysing more deeply the case $\alpha = 0°$, from the pressure profile along the body contour it is possible to see that (Fig. 8.17(a)) there is an higher pressure on the upper part of the body than in the lower part which is everywhere negative. This happens because a driven-cavity like flow establishes in the lower part of the body in which an almost steady vortex is entrapped by the flow itself (Fig. 8.17(b)). Conversely the flow in the upper part of the body behaves like the one generated by a circular cylinder inducing a quite regular vortex shedding (see figure 8.18).

For the case $\alpha = 90°$, in the initial stage of the wake development the vorticity field past the body is similar to that of a circular cylinder at the same Reynolds (see Fig. 8.19(a), 8.19(b) and 8.19(c)). Once the vortex shedding starts, at each cycle a vortex is entrapped inside the cavity in the body (see Fig. 8.19(d), 8.19(e) and 8.19(f)). This process induces a large flow dissipation which is responsible of the high drag developed in this condition.

Note that the total perimeter of the body is πD so that a comparison of the drag and lift coefficients with those for a circular cylinder with diameter D

is possible for the case $\alpha = 0°, 90°$ (the only one where an almost periodic behaviour is attained), the comparison is depicted in figure 8.20. It is straightforward to note that the drag coefficient for the cylinder at $Re = 2000$ lays between that of the C-shape at the two different angles, while the lift coefficient for the cylinder behaves similarly to the one of the C-shape with $\alpha = 90°$.

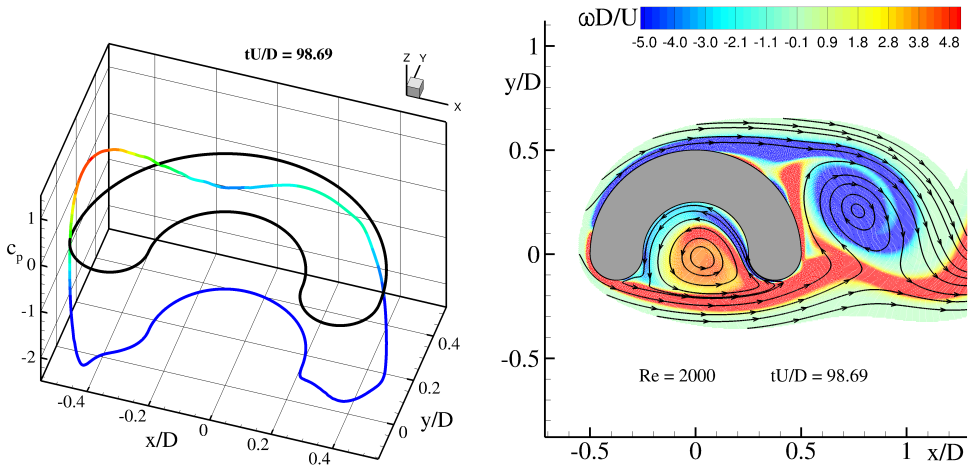

(a) (b)

Figure 8.17: C-shape at $Re = 2000$, $\alpha = 0°$ and $tU/D = 98.69471$: (a) Pressure coefficient, the black line shows the c_p zero value. (b) Vorticity field and streamlines near body. Note the vortex trapped inside the cavity by the flux itself.

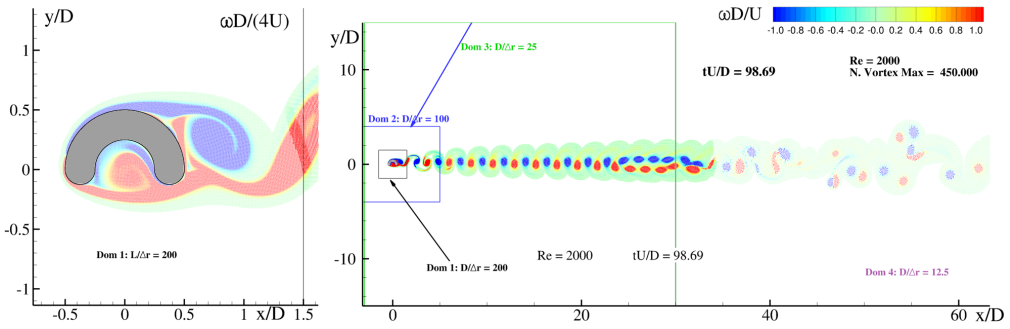

Figure 8.18: Flow around a C-Shape body at $Re = 2000$ with $\alpha = 0°$: evolution of the vorticity field past the body

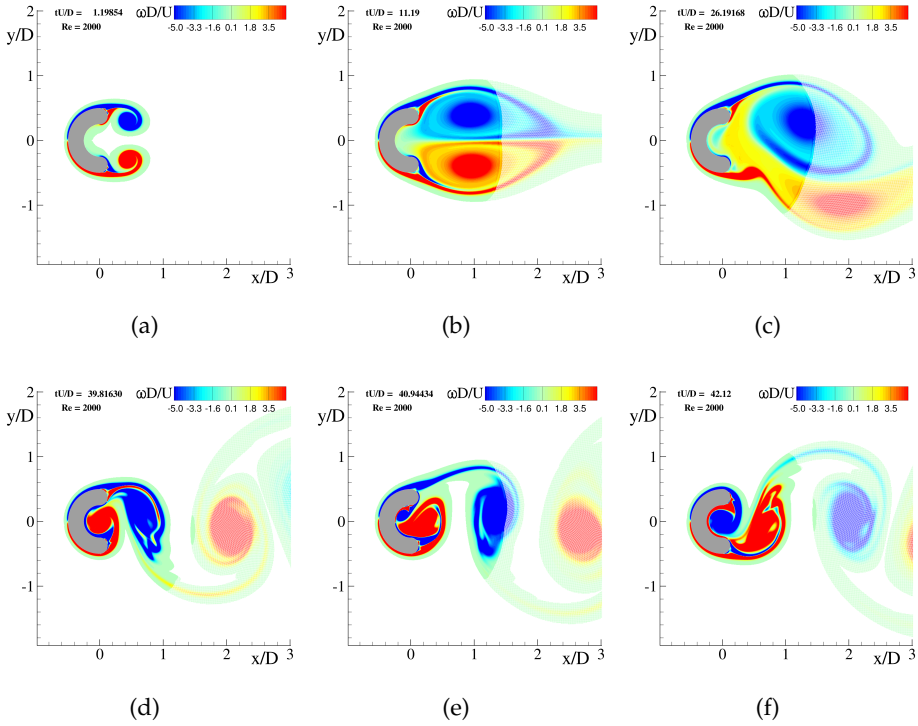

Figure 8.19: Flow around a C-Shape body at Re = 2000 with $\alpha = 90°$: evolution of the vorticity field past the body

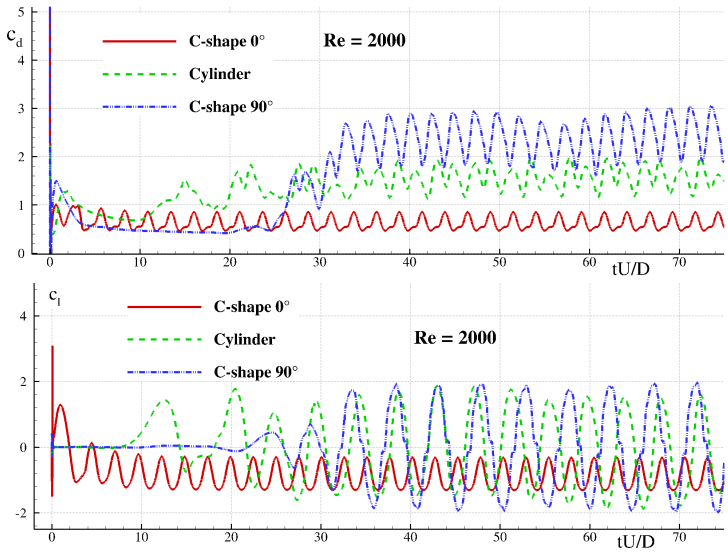

Figure 8.20: Flow around a C-Shape body at Re = 2000 with $\alpha = 0, 90°$. Drag (top) and lift (bottom) coefficients are compared to that obtained with a circular cylinder at the same Re.

8.6 FLOW AROUND AN IMPULSIVELY STARTED CIRCULAR CYLINDER AT $Re = 9500$

As a further test-case, the simulation of the flow past a circular cylinder at $Re = 9500$ is computed in order to compare the DVH method with results presented in Koumoutsakos and Leonard (1995). The latter were published twenty years ago and at that time, due to the CPU resources available, the authors simulated only the semi-plane $y > 0$ and stopped the simulation at time $tU/D = 4.0$ (being D the cylinder diameter). This test case has been also used more recently in Rossinelli et al. (2010) and Rasmussen et al. (2011) for validating two other Vortex Methods.

Figure 8.21(a) shows the comparison with the DVH results for the drag coefficient.

Figure 8.21(b) displays a longer time history for the drag coefficient. Indeed, nowadays, with a Vortex Particle method, using a Desktop PC with OpenMP parallel programming, it is possible to simulate long time evolution, $t_{end}\, U/D = 100$, at this Reynolds recording different wake oscillations and using a high spatial resolution close to the cylinder surface, $D/\Delta r = 800$. This simulation remains quite critical to perform with a standard mesh-based solver, since the wake shape changes in time and it is not possible to build a-priori an optimum mesh for capturing all the vortical structures. Furthermore, the number of mesh-points involved would be very high because the irrotational region needs also to be solved. For this reason is quite unusual, even in a

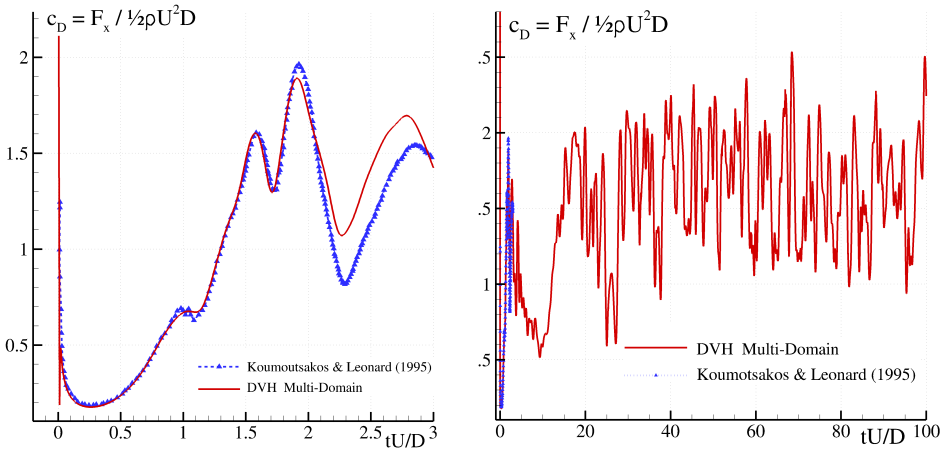

(a) (b)

Figure 8.21: (a) Comparison of the drag coefficient between Koumoutsakos & Leonard (1995) Koumoutsakos and Leonard (1995) and DVH. (b) time history of the drag coefficient for a longer time range.

2D framework, to find in the literature numerical results like the one here discussed.

Table 8.6 reports for the ratio $D/\Delta r$ used: (i) the cell-Reynolds number, (ii) the Courant number used for the advection steps, (iii) the ratio between the wall distance $y+ = 1$, measured at distance equal to the cylinder radius, R, from the stagnation point and Δr. This last parameter shows that the adopted resolution is able to well reproduce the boundary layer for the present Reynolds number.

$D/\Delta r$	$Re_{\Delta r}$	Co	$(y+=1)_R/\Delta r$	$\Delta t_a\, U/D$	$\Delta t_d\, U/D$ (Dom 1)
800	11.88	2.09	1.2	2.62×10^{-3}	5.23×10^{-3}

Table 8.6: Flow around a Circular cylinder at Re = 9500: main discretization parameters

Left plot of figure 8.22 shows the vorticity field close to the cylinder while the right plot displays the vorticity in the wake region also. One of the main features of the present model is the ability to simulate complex dynamics in the wake region. For example, in Fig. 8.23(a), after the build up of vorticity in the recirculation zone, the detachment of a first dipole composed of two large vortices of opposite signs can be appreciated. After a time interval of $tU/D = 4$ another dipole, less intense with respect to the previous one, is detached from the cylinder (Fig. 8.23(b)). These first two dipoles interact in such a way that the second dipole "steals" the counter-clockwise rotating vortex from the first dipole (Fig. 8.23(c) and 8.23(d)) creating a new vortical structures which starts to orbit around the first clockwise shed vortex. After this interaction a third and a fourth dipole are detached from the cylinder; the first one travelling downwards towards the limit of the computational domain (Fig. 8.23(e)).

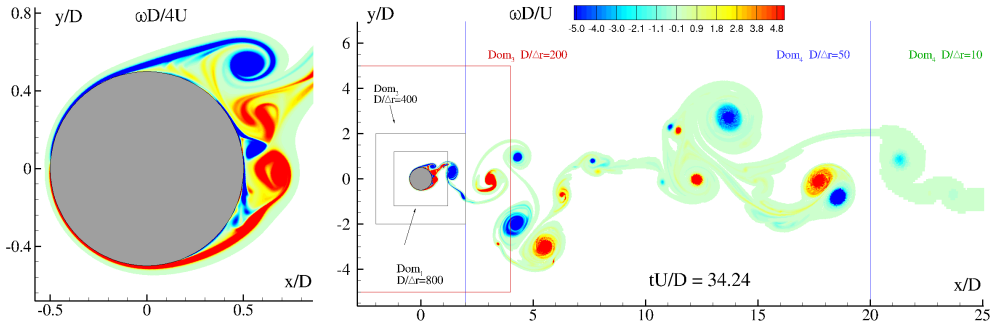

Figure 8.22: DVH vorticity field for the flow past an impulsively started circular cylinder at Re = 9500

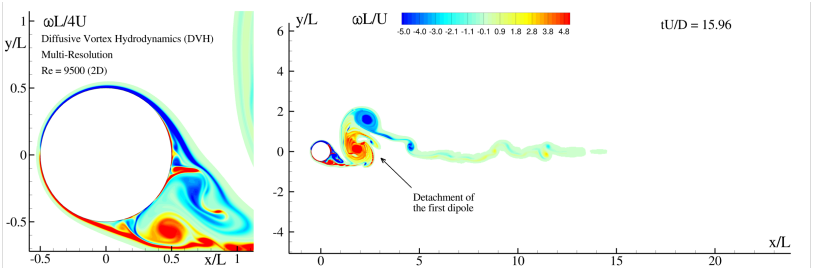

(a)

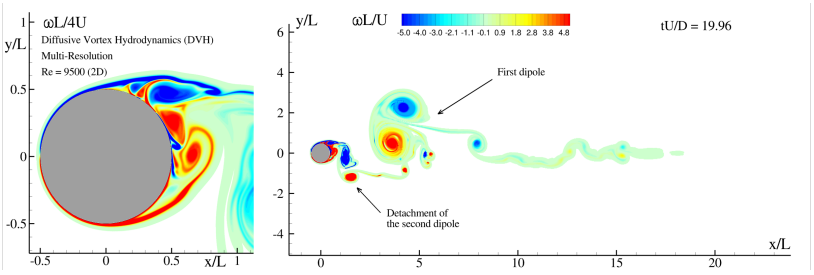

(b)

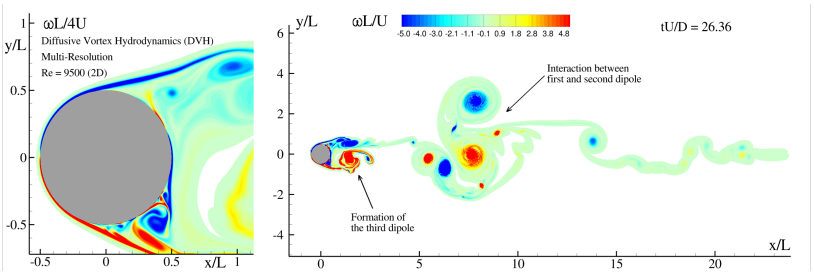

(c)

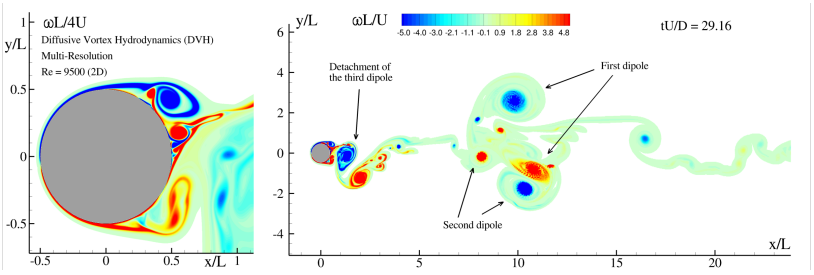

(d)

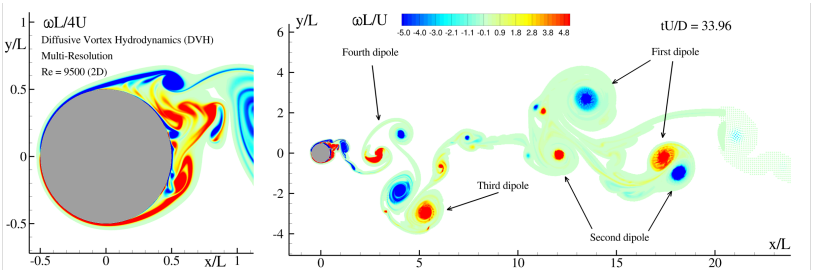

(e)

Figure 8.23: Wake past an impulsively started cylinder at Re 9500

8.7 FLOW PAST CIRCULAR CYLINDER UP TO $Re = 100\,000$

The flow past an impulsively started cylinder at Re=50 000 and Re=100 000 is considered as a final test case. For these cases a very high spatial resolution is required in the boundary layer region. For this purpose eight RPDs are used, and close to the body the resolution $D/\Delta r$ is set equal to 3200. Table 8.7 reports the main discretization parameters used for four different Reynolds numbers 1000, 9500, 50 000, 100 000. For all the Reynolds numbers the ratio between the wall distance $y+ = 1$ (measured at distance equal to the cylinder radius, R from the stagnation point) and Δr, is maintained of order of one to guarantee to have enough vortex particles even in the viscous sublayer region ($y+ < 5$).

Re	$D/\Delta r$	$Re_{\Delta r}$	Co	$(y+ = 1)_R/\Delta r$	$\Delta t_a\, U/D$	$\Delta t_d\, U/D$ (Dom 1)
1000	200	5	1.74	1.6	8.69×10^{-3}	8.69×10^{-3}
9500	800	3.75	1.32	2.8	2.62×10^{-3}	5.23×10^{-3}
5×10^4	3200	15.63	1.84	1.4	5.74×10^{-4}	1.72×10^{-3}
10^5	3200	31.25	1.84	0.8	5.74×10^{-4}	3.44×10^{-3}

Table 8.7: Flow around a circular cylinder at different Reynolds numbers: main discretization parameters

Figure 8.24 depicts the vorticity field past an impulsively started circular cylinder at Re=100.000 for four time instants. Around time $tU/D = 0.50$ the boundary layer in the rear part of the cylinder starts to destabilize and vortical dipole structures are released in the wake region. This kind of phenomenon clearly shows the complexity of the flow field at this Reynolds number.

In order to highlight the complexity of the wake for such high Reynolds numbers, the vorticity fields have been reported in figure 8.25 at four different Reynolds numbers. For the two highest Reynolds numbers the symmetry of the numerical solution is already lost at $tU/D = 4.0$.

We were not able to find in the literature numerical solutions at the two highest Reynolds numbers presented here (without using any turbulence models). Therefore we think that the presented results can be useful also for other readers who need to test numerical solvers at these viscosity levels.

In figure 8.26 the drag coefficients for the four Reynolds numbers, 1000, 9500, 50 000, 100 000, are reported. It is possible to note that the drag coefficients for the Reynolds numbers 1000, 9500 and 50000 all fluctuates around similar mean values, Different is the situation for $Re = 100000$ in which the drag coefficient has already experienced a drag crisis phenomenon. Although it is a complete 3D phenomenon, it is possible to experience this effect also in 2D simulations as reported in Singh and Mittal (2005).

Figure 8.27 depicts time averaged drag coefficient as a function of the Reynolds number. The 2D simulations of Henderson (1995) and Singh and Mittal (2005)

are also reported showing good agreement with the mean drag coefficient evaluated with the DVH algorithm. For completeness the experimental datas from Wieselsberger (1921) are also shown. The data of Henderson (1995) and Wieselsberger (1921) are taken from Singh and Mittal (2005).

As expected the 2D simulations can well reproduce the forces on the body up tu $Re \simeq 200$ and also if they show a drag crisis phenomenon it is registered about an order of magnitude earlier with respect to the experiments of

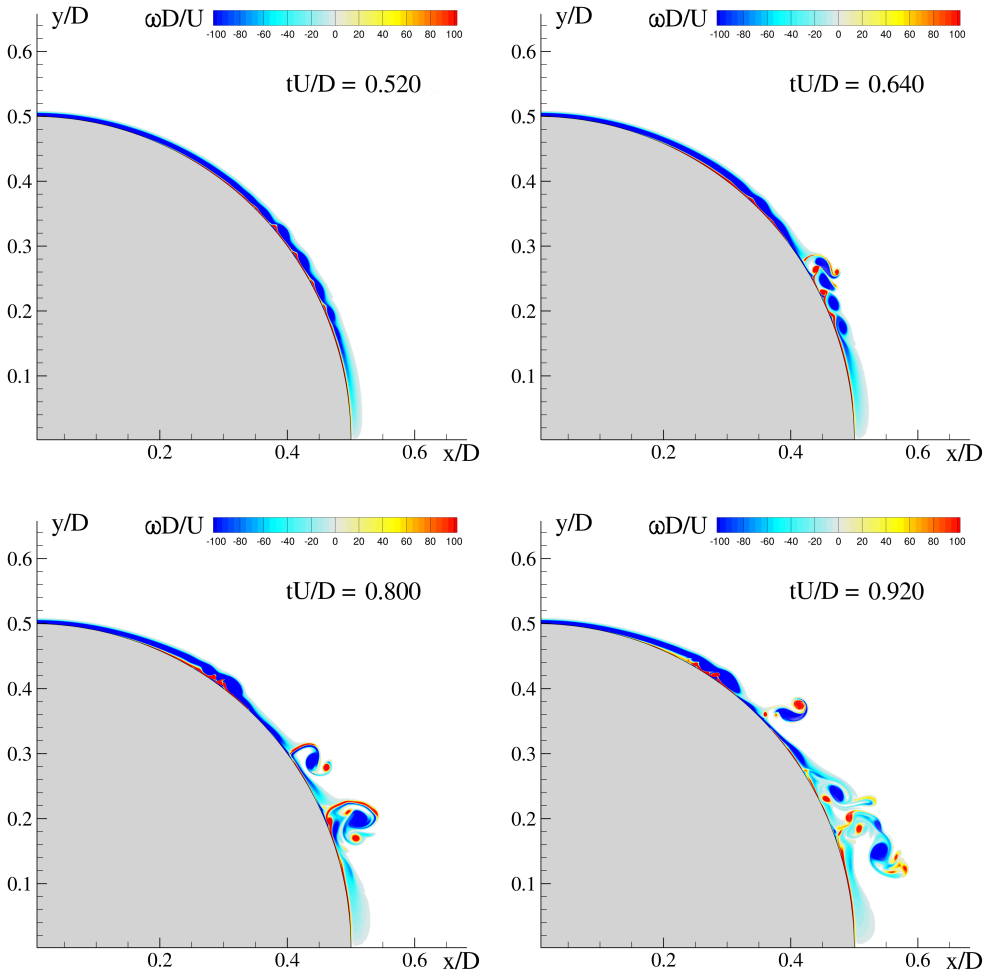

Figure 8.24: Flow around an impulsively started circular cylinder at Re=100 000. Vorticity field for four times tU/D=0.52, 0.64, 0.80, 0.92.

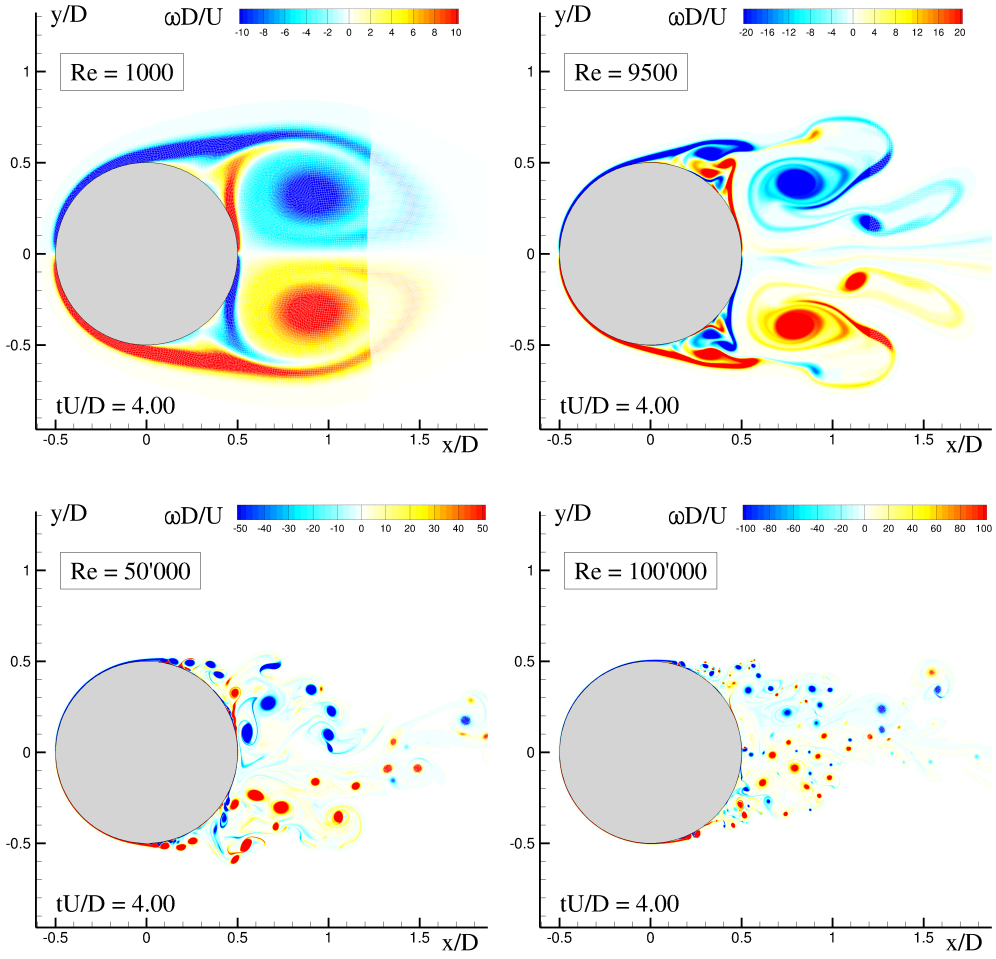

Figure 8.25: Flow around an impulsively started circular cylinder at four different Reynolds numbers. Vorticity field at time $tU/D = 4$.

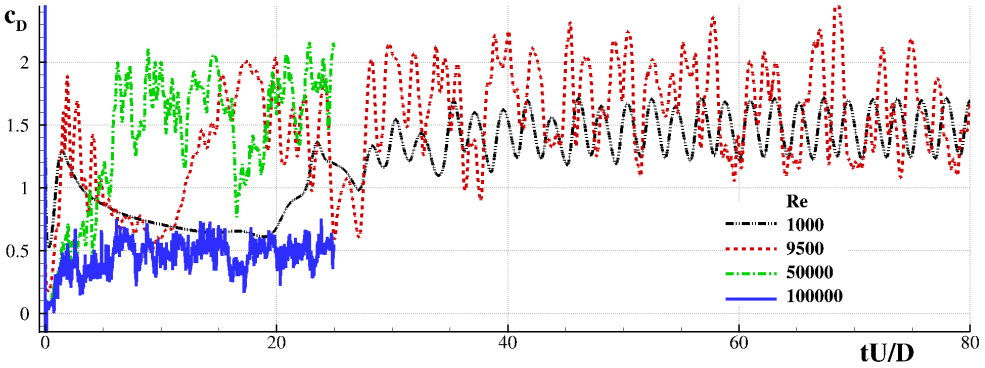

Figure 8.26: Flow around an impulsively started circular cylinder at four different Reynolds numbers. Evolution of the drag coefficient

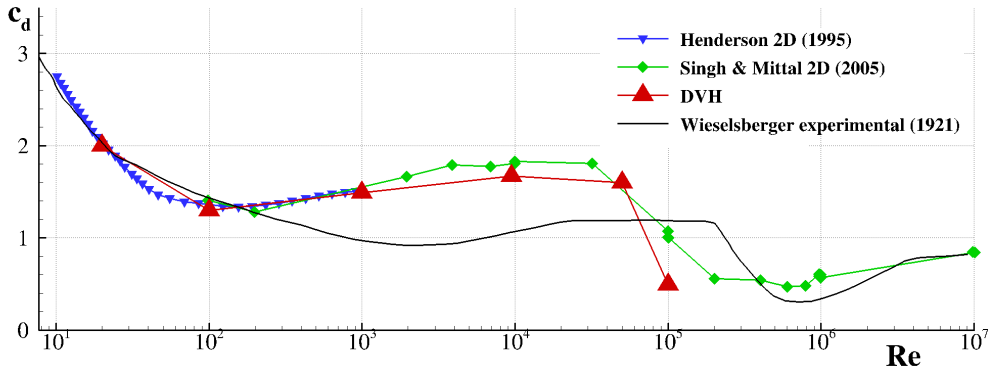

Figure 8.27: Mean drag coefficient as function of the Reynolds number. The 2D simulations of Henderson (1995) and Singh and Mittal (2005) and the experimental data of Wieselsberger (1921) are also shown.

9 FLOW IN PRESENCE OF BODIES WITH EDGES

In this section the DVH model is tested by studying flows past solid bodies with edges, such as squared cylinders or airfoils, to validate the visibility mask and the diffusion process described in section 4.6.2.

As for the simulations of section 8, a multi resolution approach is used: the spatial resolution is decreased for increasing distance from the body in the flow direction, in particular this is done using several RPDs with decreasing values of $L/\Delta r$. The nearest RPD to the body is generated using the procedure described in section 6.

A first series of simulations using squared and rectangular cylinders at $Re = 200$ is performed using various angles of attack, the results obtained (lift, drag and pressure coefficients) are compared with those presented in Steggel (1998).

In section 9.2 the DVH model is tested studying the flow past a NACA0008 airfoil with angle of attack $\alpha = 4°$ for the Reynolds numbers 2000 and 6000, the results are compared with those presented in Mittal et al. (2008).

To show the ability of the DVH model to simulate flows around sharp bodies at high Reynolds numbers, the flow past the waterline of a DDG51 hull at $Re = 100000$ is simulated.

9.1 FLOW PAST SQUARED AND RECTANGULAR CYLINDER

Following the work of Steggel (1998) a series of DVH simulations of the flow around squared and rectangular cylinders with various angle of attack is here discussed.

In this section the Reynolds number and the lift and drag coefficient are made non dimensional using the maximum cross-stream section of the body d

$$Re = \frac{Ud}{\nu},\ c_d = \frac{2F_x}{\rho U^2 d},\ c_l = \frac{2F_y}{\rho U^2 d}. \tag{9.1}$$

Figure 9.1 depicts the definition of the maximum cross-stream section of the body d together with the angle of attack α and the side (A and B) of the rectangle while in table 9.1 the main parameters of the spatial/time resolution adopted are shown, adopting the same Reynolds number $Re = 200$ and the same spatial resolution for all the simulations showed in this section.

A first series of simulations using a squared cylinder (A=B) with angles of attack $\alpha = 0°$ and $\alpha = 45°$ have been performed.

$c/\Delta r$	$Re_{\Delta r}$	Co	$\Delta t_a\, U/d$	$\Delta t_d\, U/cd$ (Dom 1)
100	2.00	0.70	7.05×10^{-3}	7.05×10^{-3}

Table 9.1: Flow around squared and rectangular cylinders at Re = 200: main discretization parameters

Figure 9.2 depicts the vorticity field in the far regions from the bodies for the two angles of attack used.

A comparison of the lift and drag coefficient with the results reported in Steggel (1998) for the cases studied is depicted in figure 9.3 and 9.4 for the angles of attack $\alpha = 0°$ and $\alpha = 45°$ respectively and a good agreement is obtained in the periodic regime.

A second series of simulations using a rectangular cylinder with $B = 2A$ and angles of attack $\alpha = 90°$ have been performed. Figure 9.5 depicts the vorticity field in the far regions from the bodies.

A comparison of the lift and drag coefficient with the results reported in Steggel (1998) for the case of figure 9.5 is depicted in figure 9.6 and a good agreement is obtained in the periodic regime.

It is possible to note for both the squares and the rectangle simulations a slight difference in the Strouhal number obtained with the DVH with respect to the one of Steggel (1998). This is possibly due to the low resolution used in Steggel (1998).

For the rectangular cylinder with angle of attack of 90°, a comparison of the pressure coefficient along the body contour has also been made. Figure 9.7 depict the pressure coefficient c_p for the rectangular cylinder with angle of attack $\alpha = 90°$, achieving a good comparison with the results of Steggel (1998).

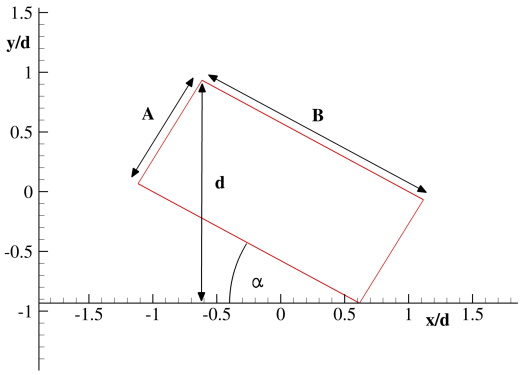

Figure 9.1: Geometrical parameters for a flow simulation around a rectangular cylinder

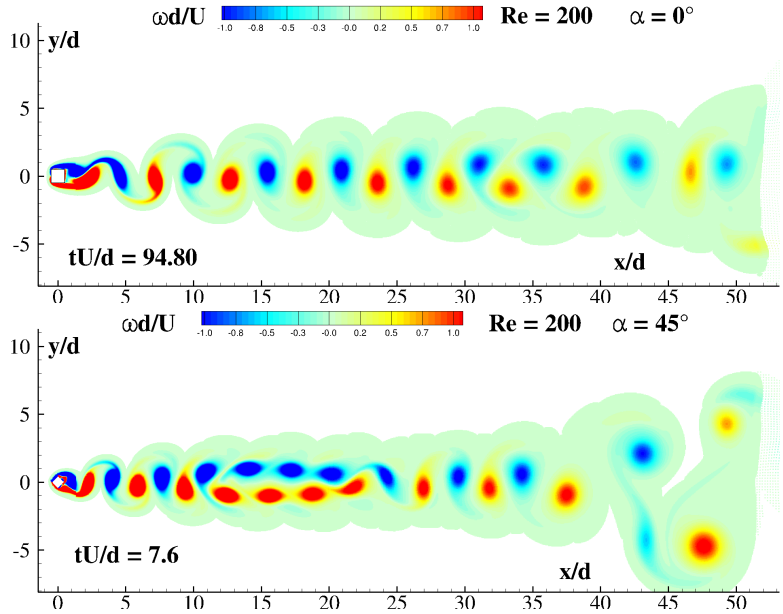

Figure 9.2: Vorticity field for $d/\Delta r = 100$ for a squared cylinder at $Re = 200$ and various angles of attack α. From top to bottom $\alpha = 0°$, and $\alpha = 45°$.

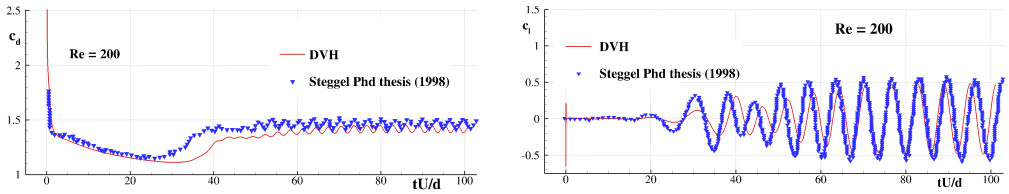

Figure 9.3: Drag (left plot) and lift (right plot) coefficients for a squared cylinder at $Re = 200$ and angle of attack $\alpha = 0°$. Comparison with Steggel (1998) is shown

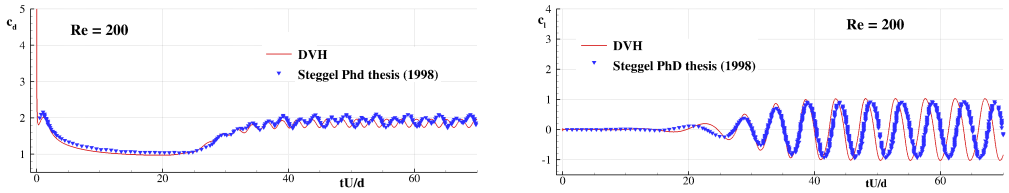

Figure 9.4: Drag (left plot) and lift (right plot) coefficients for a squared cylinder at $Re = 200$ and angle of attack $\alpha = 45°$. Comparison with Steggel (1998) is shown

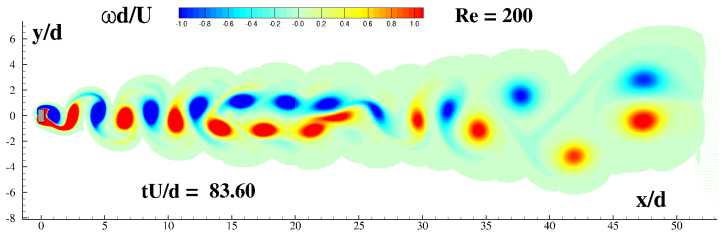

Figure 9.5: Evolution of the vorticity field for $d/\Delta r = 100$ for a rectangular cylinder at $Re = 200$ and two angles of attack α.

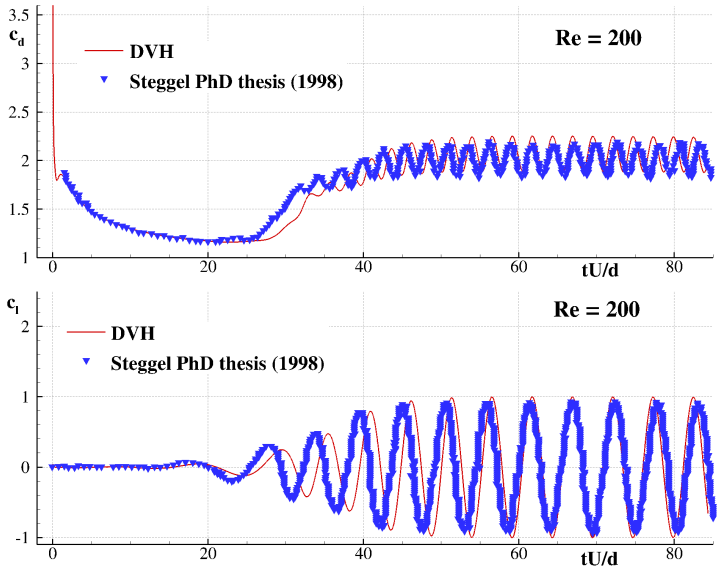

Figure 9.6: Drag and lift coefficient for an impulsively started rectangular cylinder at $Re = 200$ and $\alpha = 90°$. Comparison with Steggel (1998) is shown

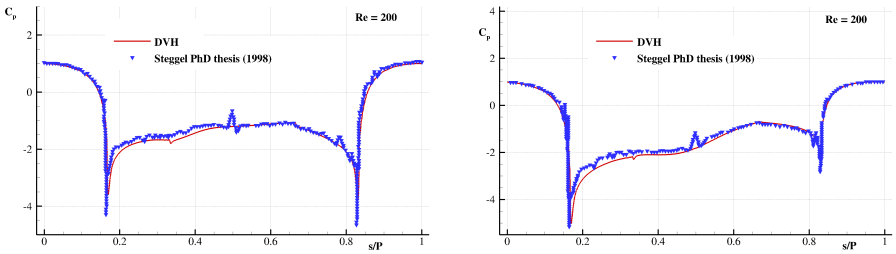

Figure 9.7: Pressure coefficient for an impulsively started rectangular cylinder at $Re = 200$ and $\alpha = 90°$. Left: c_p taken at zero value of c_l. Right: c_p taken at maximum value of c_l. Comparison with Steggel (1998) is shown.

9.2 FLOW PAST AN AIRFOIL NACA0008

Following the work of Mittal et al. (2008) the flow around an airfoil NACA0008 with angle of attack $\alpha = 4°$ at two different Reynolds numbers 2000 and 6000 is simulated. Table 9.2 shows the main parameters of the spatial/time resolution adopted.

Re	$c/\Delta r$	$Re_{\Delta r}$	Co	$\Delta t_a\, U/d$	$\Delta t_d\, U/cd$ (Dom 1)
2000	800	2.50	0.88	1.10×10^{-3}	1.10×10^{-3}
6000	1000	6.00	2.11	2.11×10^{-3}	2.11×10^{-3}

Table 9.2: Flow around an airfoil NACA0008 at with angle of attack $\alpha = 4°$: main discretization parameters

Figure 9.8 depicts the vorticity field for both Reynolds numbers. In the simulation with $Re = 2000$ the vorticity field remains stable throughout the whole simulation while at $Re = 6000$ the vorticity field become unstable giving birth to von Karman vortex street. This instability is possibly due to the presence of an RPD in the region near the body generated through the algorithm described in section 6. In fact while the packing algorithm preserve the volume occupied by each point of the distribution, it may introduce small asymmetries in the points distribution the may lead, especially at high Reynolds numbers, to these behaviours.

Figure 9.9 depicts the lift and drag coefficients for the two Reynolds numbers studied, together with the data from Mittal et al. (2008).

9.3 FLOW PAST A DDG51 HULL WATERLINE

A two dimensional simulation of the water line of a hull DDG51 has been performed at $Re = 100000$. The ship is supposed to advance with a steady drift angle, the main discretization parameter of the simulation are given in table 9.3

Re	Fr	$c/\Delta r$	$Re_{\Delta r}$	Co	$\Delta t_a\, U/d$	$\Delta t_d\, U/cd$ (Dom 1)
100000	0.01	3200	31.25	1.84	5.74×10^{-4}	3.44×10^{-3}

Table 9.3: Flow around the waterline of a DDG51 shiphull advancing with a steady drift angle: main discretization parameters

A low Froude number $Fr = 0.01$ is used in order to guarantee that the free surface remains unperturbed (no ship waves generation) as may happen for a ship maneuvering in a harbour. In this case it is possible to study the generation of vorticity along the waterline of the ship.

At such high Reynolds number the vorticity field generated by a narrow object become more complicated. An example of the complex shed and evolution of the vorticity field is depicted in figure 9.11 where a series of small vortices are detached from the ship bow. These vortices interact with a bigger one starting to orbit around it creating a complex "flower shaped" vorticity structure.

Another example of the complex evolution of the vorticity field can be found analysing the behaviour of the vorticity field on the right side of the hull. In this case, together with the formation of the vorticity structures, also described in the case of an impulsively starte cylinder at $Re = 100000$, typical of an high Reynolds flow, it is possible to note a zone close to the hull in which the vortices travels upstream, moving from the stern to the bow of the ship.

Figure 9.12 depicts the evolution of an isolated vortex (highlighted by a black arrow) that, once reached the hull, detaches a portion of the boundary layer, rebounding on the side of the ship. After this it travels fast towards the bow where it merges with the other vortices.

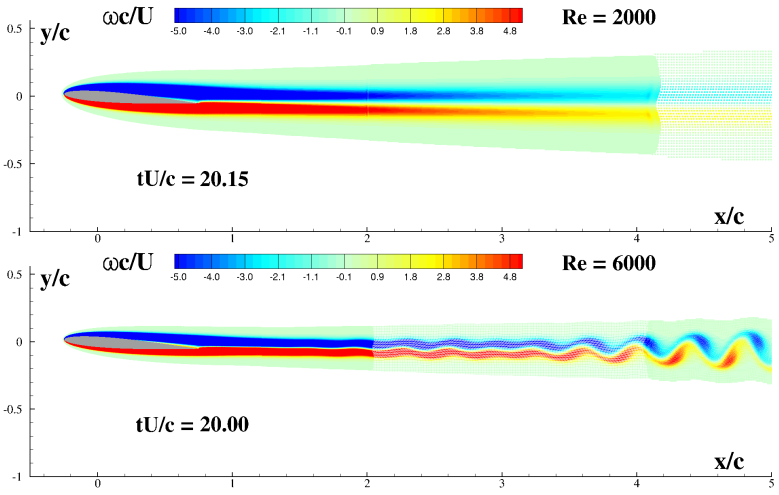

Figure 9.8: Vorticity profile for an airfoil NACAooo8 with angle of attack $\alpha = 4°$ at two different Reynolds numbers.

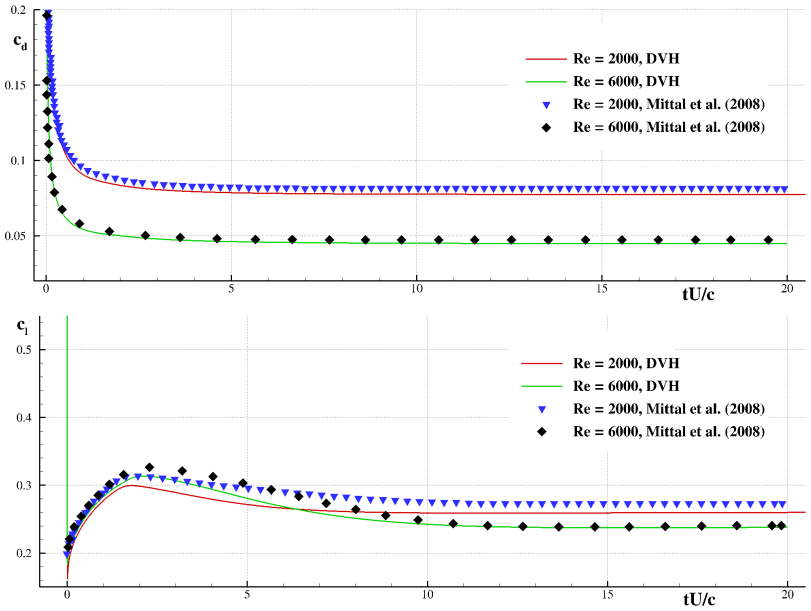

Figure 9.9: Lift and drag coefficients for a flow past a NACAooo8 airfoil with angle of attack $\alpha = 4°$ and two different Reynolds numbers. Data from Mittal et al. (2008) are also shown.

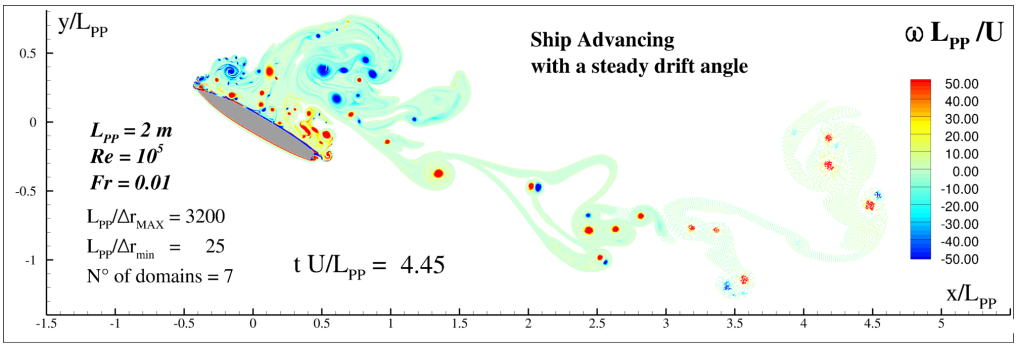

Figure 9.10: Vorticity field generated by the waterline of a DDG51 shiphull advancing with a steady drift angle $\alpha = 30°$ at a low Froude number $fr = 0.01$

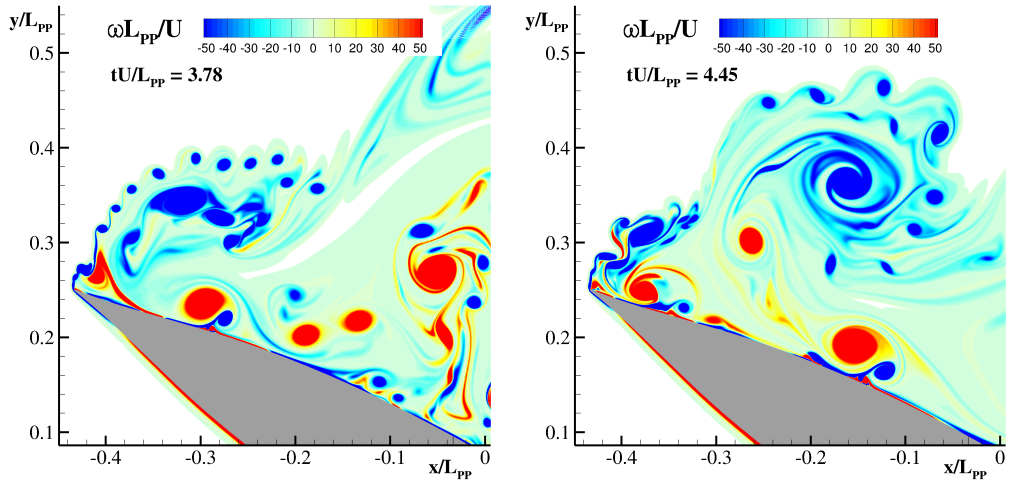

Figure 9.11: Detachment and evolution of vortices from the ship bow. Left: detachment of small vortices from the ship bow. Right: interaction of the small vortices with a bigger one to create a "flower shaped" structure.

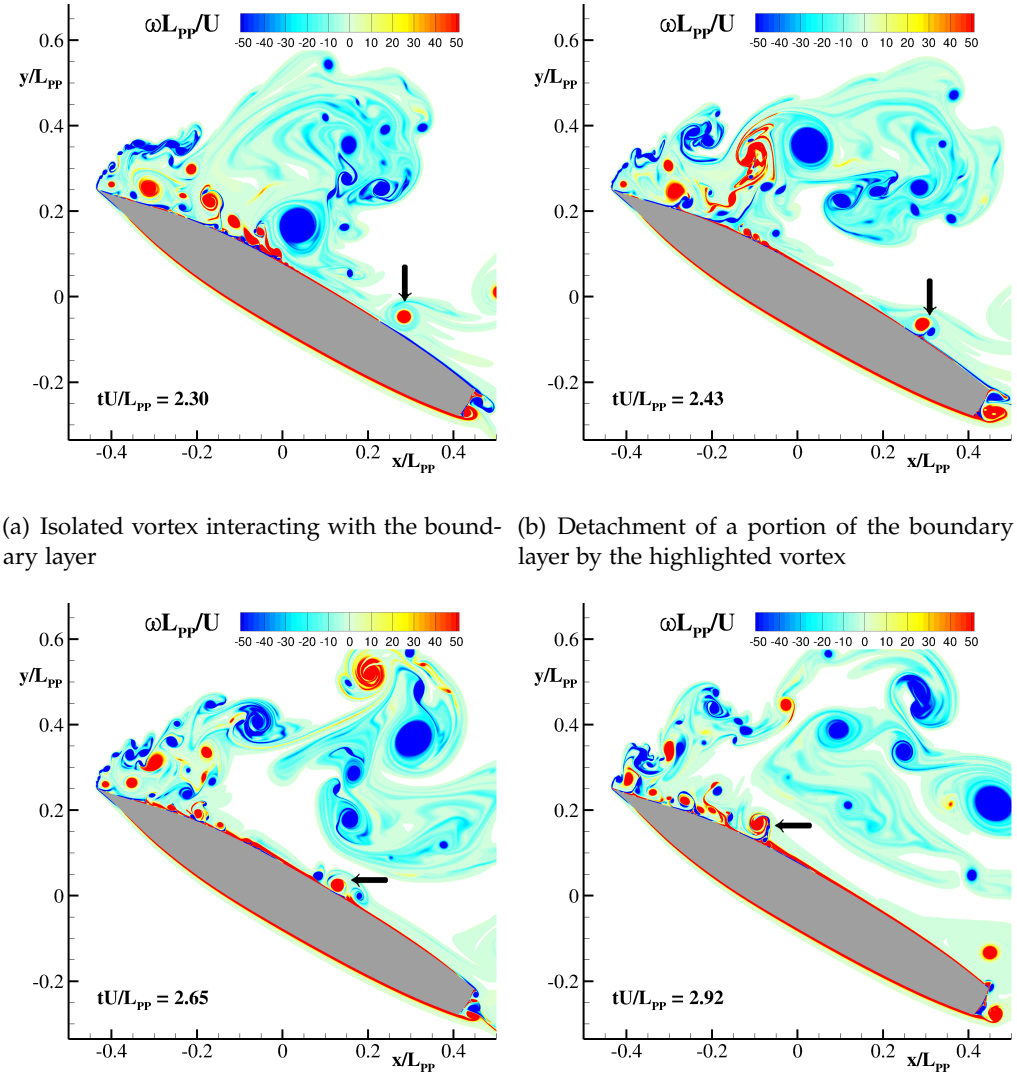

(a) Isolated vortex interacting with the boundary layer

(b) Detachment of a portion of the boundary layer by the highlighted vortex

(c) The highlighted vortex travels upstream towards the bow of the ship

(d) The isolated vortex merges with the vorticity in bow region

Figure 9.12: Evolution of the vorticity field near the right side of the hull. Evolution of a vortex travelling upstream in this zone.

10 CONCLUSIONS AND PERSPECTIVES

This work presented a new vortex method called Diffused Vortex Hydrodynamic (DVH). The DVH is a two dimensional particle vortex method in which is not necessary the use of any remeshing method tanks to the introduction of "Regular Point Distribution" (RPD) in the diffusion process. The velocity of the vortex particles is evaluated using a Fast Multipole Method.

The DVH can be applied to perform high Reynolds simulations of flows around bodies with arbitrary shapes thanks to the use of RPDs and to the introduction of a so called visibility mask to perform diffusion in presence of bodies with edges such as squared cylinders or airfoils.

A RPD is a set of equispaced points without any topological connection. During the diffusion process each vortex gives its diffusive contribution to RPDs nodes using the fundamental solution of the heat equation, after the diffusion of all vortices a new set of regularly spaced particles is generated at the RPDs nodes location, substituting the former one. This procedure avoids the formation of holes and accumulations in the vorticity distribution without the use of any remeshing method.

The DVH method has been tested on a series of different problems ranging from the evolution of vorticity distribution in free space to flows in presence of bluff bodies with different shapes.

The evolution of vorticity distribution in free space has been simulated to better control the errors made in the diffusive and in the advective step respectively. Two classical problems have been considered: the Lamb-Oseen problem and the merger of a pair of co-rotating vortices. The Lamb-Oseen test case showed a typical behaviour of the particles methods: the errors on the vorticity distributions, evaluated against the exact solution, presents two distinct regimes: a first one, for low spatial resolutions, where the error reduces and a second one, for higher resolutions, where the error remains constant. On the other hand the errors on the velocity field presents an almost constant rate of convergence of about 2. A similar rate of convergence have also been found for the simulation of the merger of a pair of co-rotating vortices, where the errors have been evaluated on the evolution of the excess energy and the second momentum of the vorticity field.

The ability of the DVH to simulate flows in presence of bluff bodies with different shapes has been tested using various test case found in the literature, as the circular cylinder at $Re = 9500$ presented in Koumoutsakos and Leonard (1995), the inclined elliptic cylinders at $Re = 3000$ and $Re = 10000$ presented

in Nair and Sengupta (1997) or the NACA0008 airfoils with Reynolds number up to 6000 presented in Mittal et al. (2008). All the simulations made showed a good agreement with the reference data used.

The ability of the DVH method to simulate flows at high Reynolds numbers is tested simulating the flow past a circular cylinders with a Reynolds number up to 100000. We were not able to find in the literature numerical solutions at a such high Reynolds number (without using any turbulence models). Therefore we think that the presented results can be useful also for other readers who need to test numerical solvers at these viscosity levels. Covering a such wide range of Reynolds numbers a plot of the time averaged drag coefficient at various Re has been possible showing good agreement with the results in Singh and Mittal (2005).

As a last test case a two dimensional simulation of the water line of a DDG51 hull has been performed at $Re = 100000$. The ship is supposed to advance with a steady drift angle at a low Froude number $Fr = 0.01$ in order to guarantee that the free surface remains unperturbed. In this case it has been possible to study the generation and the detachment of vorticity from a sharp narrow object at an high Reynolds number.

For future developments the DVH method can be extended in order to solve problems with multiple moving and/or deformable bodies, or with a free surface.

Moving or deformable bodies are not difficult, in principle, to deal with because only the RPD attached to the body itself must be changed using the packing algorithm, while the other RPDs, being simple Cartesian lattices, can be easily updated.

It is possible to deal with free surface flows using, for example, a BEM solver as in Graziani et al. (1998). The possibility to couple the DVH method with an SPH solver for handling breaking waves is also under study.

Finally, the extension to 3D is under construction. In this case the use of more sophisticated parallel algorithm for solving the velocity field through Treecode/Fast Multipole Method (FMM) is needed in order to achieve an high scalability of the code.

BIBLIOGRAPHY

Agishtein, Michael E and Alexander A Migdal (1989). "Dynamics of vortex surfaces in three dimensions: Theory and simulations". In: *Physica D: Nonlinear Phenomena* 40.1, pp. 91–118.

Antuono, M. et al. (2013). "Conservation of circulation in SPH for 2D free-surface flows". In: *International Journal for Numerical Methods in Fluids* 72.5, pp. 583–606. ISSN: 1097-0363. DOI: 10.1002/fld.3757. URL: http://dx.doi.org/10.1002/fld.3757.

Appel, Andrew W (1985). "An efficient program for many-body simulation". In: *SIAM Journal on Scientific and Statistical Computing* 6.1, pp. 85–103.

Ashurst, Wm T and Eckart Meiburg (1988). "Three-dimensional shear layers via vortex dynamics". In: *Journal of fluid mechanics* 189, pp. 87–116.

Barba, LA et al. (2003). "Numerical investigations on the accuracy of the vortex method with and without remeshing. AIAA# 2003-3426". In: *16th CFD Conference, Orlando FL*.

Barnes, Josh and Piet Hut (1986). "A hierarchical O (N log N) force-calculation algorithm". In:

Bassanini, P et al. (1991). "A boundary integral formulation for the kinetic field in aerodynamics. I: Mathematical analysis". In: *European journal of mechanics. B, Fluids* 10.6, pp. 605–627.

Beale, J Thomas and Andrew Majda (1985). "High order accurate vortex methods with explicit velocity kernels". In: *Journal of Computational Physics* 58.2, pp. 188–208.

Benson, MG et al. (1989). "A viscous splitting algorithm applied to low Reynolds number flows round a circular cylinder". In: *Journal of Fluids and Structures* 3.5, pp. 439–479.

Bernard, Peter S (1995). "A deterministic vortex sheet method for boundary layer flow". In: *Journal of Computational Physics* 117.1, pp. 132–145.

— (1996). "A vortex method for wall bounded turbulent flows". In: *Esaim: Proceedings*. Vol. 1. EDP Sciences, pp. 15–31.

Birdsall, Charles K and Dieter Fuss (1997). "Clouds-in-clouds, clouds-in-cells physics for many-body plasma simulation". In: *Journal of Computational Physics* 135.2, pp. 141–148.

Bouscasse, B. et al. (2013). "Nonlinear water wave interaction with floating bodies in SPH". In: *Journal of Fluids and Structures* 42, pp. 112–129.

Chorin, Alexandre Joel (1973). "Numerical study of slightly viscous flow". In: *Journal of Fluid Mechanics* 57.04, pp. 785–796.

Chorin, Alexandre Joel (1978). "Vortex sheet approximation of boundary layers". In: *Journal of Computational Physics* 27.3, pp. 428–442.

— (1981). "Estimates of intermittency, spectra, and blow-up in developed turbulence". In: *Communications on Pure and Applied Mathematics* 34.6, pp. 853–866.

Colagrossi, A. et al. (2011). "Theoretical analysis and numerical verification of the consistency of viscous smoothed-particle-hydrodynamics formulations in simulating free-surface flows". In: *Physical Review E* 84, pp. 26705+.

Colagrossi, A. et al. (2012). "Particle packing algorithm for SPH schemes". In: *Computer Physics Communications* 183.2, pp. 1641–1683.

Colagrossi, Andrea et al. (2009). "Theoretical considerations on the free-surface role in the smoothed-particle-hydrodynamics model". In: *Physical Review E* 79.5, p. 056701.

Colagrossi, Andrea et al. (2013). "Smoothed-particle-hydrodynamics modeling of dissipation mechanisms in gravity waves". In: *Phys. Rev. E* 87 (2), p. 023302.

Cottet, Georges-Henri and Petros D Koumoutsakos (2000). *Vortex methods: theory and practice*. Cambridge university press.

Cottet, Georges-Henri et al. (2000). "Vortex methods with spatially varying cores". In: *Journal of Computational Physics* 162.1, pp. 164–185.

Degond, P and S Mas-Gallic (1989a). "The weighted particle method for convection-diffusion equations. II. The anisotropic case". In: *Mathematics of Computation* 53.188, pp. 509–525.

Degond, Pierre and S Mas-Gallic (1989b). "The weighted particle method for convection-diffusion equations. I. The case of an isotropic viscosity". In: *Mathematics of Computation* 53.188, pp. 485–507.

Di Lisio, R. et al. (1998). "The convergence of the SPH method". In: *Computers and Mathematics with Applications* 35.1–2, pp. 95–102.

Di Salvo, P. (1996). "Studio del rilascio di vorticità e dele forze generate su un corpo in movimento". PhD thesis. Sapienza, Università di Roma.

Eldredge, Jeff D (2005). "Efficient tools for the simulation of flapping wing flows". In: *AIAA* 85.2005, pp. 1–11.

Ellero, Marco et al. (2010). "Implicit atomistic viscosities in smoothed particle hydrodynamics". In: *Phys. Rev. E* 82.4, p. 046702. DOI: 10.1103/PhysRevE.82.046702.

Evans, Martha W et al. (1957). *The particle-in-cell method for hydrodynamic calculations*. Tech. rep. DTIC Document.

Fatehi, R and MT Manzari (2011). "Error estimation in smoothed particle hydrodynamics and a new scheme for second derivatives". In: *Computers & Mathematics with Applications* 61.2, pp. 482–498.

Fries, T.P. and H.G. Matthies (2004). "Classification and Overview of Meshfree Methods". In: *Scientific Computing, Informatikbericht*. Ed. by Germany Technical University Braunschweig Brunswick.

Gharakhani, Adrin and Ahmed F Ghoniem (1996). "Massively parallel implementation of a 3D vortex-boundary element method". In: *ESAIM: Proceedings*. Vol. 1. EDP Sciences, pp. 213–223.

— (1997). "Three-dimensional vortex simulation of time dependent incompressible internal viscous flows". In: *Journal of Computational Physics* 134.1, pp. 75–95.

Graziani, G et al. (1995). "From a boundary integral formulation to a vortex method for viscous flows". In: *Computational mechanics* 15.4, pp. 301–314.

Graziani, G. et al. (1998). "Numerical Solution of the Flow Past a Freely Oscillating Body in Waves and Currents". In: *2nd International Conference on Hydroelasticity in Marine Technology, Fukuoka, Japan*.

Greengard, Claude (1985). "The core spreading vortex method approximates the wrong equation". In: *Journal of Computational Physics* 61.2, pp. 345–348.

Hald, Ole H (1986). "Convergence of a random method with creation of vorticity". In: *SIAM journal on scientific and statistical computing* 7.4, pp. 1373–1386.

Henderson, Ronald D (1995). "Details of the drag curve near the onset of vortex shedding". In: *Physics of Fluids (1994-present)* 7.9, pp. 2102–2104.

Hockney, R.W. and Eastwood J.W. (1988). *Computer simulation using particles*. Adam Hilger, Bristol.

Huang, Chien-Jung and Mei-Jiau Huang (2013). "A vortex method suitable for long time simulations of flow over body of arbitrary geometry". In: *Computers & Fluids* 74, pp. 1–12.

Koumoutsakos, Petros and A Leonard (1995). "High-resolution simulations of the flow around an impulsively started cylinder using vortex methods". In: *Journal of Fluid Mechanics* 296, pp. 1–38.

Kuwahara, Kunio and Hideo Takami (1973). "Numerical studies of two-dimensional vortex motion by a system of point vortices". In: *Journal of the Physical Society of Japan* 34.1, pp. 247–253.

Landrini, Maurizio (1993). "Fenomeni non lineari nella propagazione di onde di superficie libera". PhD thesis. Sapienza, Università di Roma.

Leonard, Anthony (1980). "Vortex methods for flow simulation". In: *Journal of Computational Physics* 37.3, pp. 289–335.

Libersky, L.D. et al. (1993). "High strain Lagrangian hydrodynamics a three-dimensional SPH code for dynamic material response". In: *J. Comp. Phys.* 109.1, pp. 67–75.

Liu, Chung Ho and Denis J Doorly (2000). "Vortex particle-in-cell method for three-dimensional viscous unbounded flow computations". In: *International journal for numerical methods in fluids* 32.1, pp. 23–42.

Lucy, L.B. (1977). "A numerical approach to the testing of the fission hypothesis". In: *Astronomical Journal* 82, pp. 1013–1024.

Macià, Fabricio et al. (2011). "Theoretical Analysis of the No-Slip Boundary Condition Enforcement in SPH Methods". In: *Progress of Theoretical Physics*

125.6, pp. 1091–1121. DOI: 10.1143/PTP.125.1091. URL: http://ptp.ipap.jp/link?PTP/125/1091/.

Majda, Andrew and J Thomas Beale (1982). "Vortex methods II: Higher order accuracy in two and threedimensions". In: *Math. Comp* 39, pp. 29–52.

Marrone, S. et al. (2011). "Delta-SPH model for simulating violent impact flows". In: *Computer Methods in Applied Mechanics and Engineering* 200.13-16, pp. 1526 –1542. ISSN: 0045-7825. DOI: 10.1016/j.cma.2010.12.016. URL: http://www.sciencedirect.com/science/article/pii/S0045782510003725.

Marrone, S. et al. (2013). "An accurate SPH modeling of viscous flows around bodies at low and moderate Reynolds numbers". In: *Journal of Computational Physics* 245.0, pp. 456 –475. ISSN: 0021-9991. DOI: 10.1016/j.jcp.2013.03.011. URL: http://www.sciencedirect.com/science/article/pii/S0021999113001885.

Marshall, JS and JR Grant (1996). "Penetration of a blade into a vortex core: vorticity response and unsteady blade forces". In: *Journal of Fluid Mechanics* 306, pp. 83–109.

Martin, James E and E Meiburg (1991). "Numerical investigation of three-dimensionally evolving jets subject to axisymmetric and azimuthal perturbations". In: *Journal of Fluid Mechanics* 230, pp. 271–318.

Mas-Gallic, S and PA Raviart (1987). "A particle method for first-order symmetric systems". In: *Numerische Mathematik* 51.3, pp. 323–352.

Mas-Gallic, Sylvie (1987). "Contribution à l'analyse numérique des méthodes particulaires". PhD thesis. Paris 6.

Milinazzo, F and PG Saffman (1977). "The calculation of large Reynolds number two-dimensional flow using discrete vortices with random walk". In: *Journal of Computational Physics* 23.4, pp. 380–392.

Mittal, Rajat et al. (2008). "A versatile sharp interface immersed boundary method for incompressible flows with complex boundaries". In: *Journal of computational physics* 227.10, pp. 4825–4852.

Molteni, DIEGO et al. (2007). "On the use of an alternative water state equation in SPH". In: *Proc. SPHERIC, 2nd International Workshop, Universidad Politécnica de Madrid, Spain*. Citeseer.

Monaghan, J. J. and R. A. Gingold (1983). "Shock Simulation by the particle method SPH". In: *Journal of Computational Physics* 52.2, pp. 374–389.

Monaghan, J.J. (1992). "Smoothed Particle Hydrodynamics". In: *Annual Review of Astronomy and astrophysics* 30, pp. 543–574.

— (1994). "Simulating Free Surface Flows with SPH". In: *J. Comp. Phys.* 110.2, pp. 39–406.

Monaghan, J.J. and J.B. Kajtar (2009). "SPH particle boundary forces for arbitrary boundaries". In: *Computer Physics Communications* 180.10, pp. 1811 –1820. ISSN: 0010-4655. DOI: 10.1016/j.cpc.2009.05.008.

Morris, Joseph P. et al. (1997). "Modeling Low Reynolds Number Incompressible Flows Using SPH". In: *Journal of Computational Physics* 136, pp. 214–226. DOI: http://dx.doi.org/10.1006/jcph.1997.5776.

Mortazavi, I et al. (1996). "Numerical convergence of the random vortex method for complex flows". In: *ESAIM: Proceedings*. Vol. 1. EDP Sciences, pp. 521–538.

Nair, MT and TK Sengupta (1997). "Unsteady flow past elliptic cylinders". In: *Journal of fluids and structures* 11.6, pp. 555–595.

Nordmark, Henrik O (1991). "Rezoning for higher order vortex methods". In: *Journal of Computational Physics* 97.2, pp. 366–397.

Oger, G. et al. (2006). "Two-dimensional SPH simulations of wedge water entries". In: *J. Comp. Phys.* 213 (2), pp. 803–822.

Ploumhans, P and GS Winckelmans (2000). "Vortex methods for high-resolution simulations of viscous flow past bluff bodies of general geometry". In: *Journal of Computational Physics* 165.2, pp. 354–406.

Ploumhans, P et al. (2004). "Simulation of three-dimensional bluff-body flows using the vortex particle and boundary element methods". In: *Flow, turbulence and combustion* 73.2, pp. 117–131.

Ploumhans, Paul et al. (2002). "Vortex Methods for Direct Numerical Simulation of Three-Dimensional Bluff Body Flows: Application to the Sphere at¡ i¿ Re¡/i¿= 300, 500, and 1000". In: *Journal of Computational Physics* 178.2, pp. 427–463.

Press, William H (2007). *Numerical recipes 3rd edition: The art of scientific computing*. Cambridge university press.

Puckett, Elbridge Gerry (1989). "A study of the vortex sheet method and its rate of convergence". In: *SIAM journal on scientific and statistical computing* 10.2, pp. 298–327.

Quinlan, Nathan J. et al. (2006). "Truncation error in mesh-free particle methods". In: *International Journal for Numerical Methods in Engineering* 66.13, pp. 2064–2085. URL: http://dx.doi.org/10.1002/nme.1617.

Ranucci, M. (1995). "Effetti del rilascio di vorticità nell'interazione corpo fluido". PhD thesis. Sapienza, Università di Roma.

Rasmussen, J.T. et al. (2011). "A multiresolution remeshed Vortex-In-Cell algorithm using patches". In: *Journal of Computational Physics* 230.17, pp. 6742–6755.

Riccardi, G and D Durante (2006). *Elementi di fluidodinamica*. Springer.

Rosenhead, L (1931). "The formation of vortices from a surface of discontinuity". In: *Proceedings of the Royal Society of London. Series A, Containing Papers of a Mathematical and Physical Character*, pp. 170–192.

Rosenhead, Louis and L Rosenhead (1963). *Laminar Boundary Layers: An Account of the Development, Structure, and Stability of Laminar Boundary Layers in Incompressible Fluids, Together with a Description of the Associated Experimental Techniques*. Clarendon Press.

Rossi, E. et al. (2013). "Two dimensional Vorticity dynamic studied with two different Particle methods". In: *XXI congresso AIMETA*.

Rossi, E. et al. (2014a). "Numerical Simulation of 2D-Vorticity Dynamics using Particle Methods". In: *Computers & Mathematics with Applications* (submitted to).

Rossi, E. et al. (2014b). "Simulating vortex shedding around bodies of arbitrary geometries through the Diffused Vortex Hydrodynamics method". In: *Communications in Computational Physics* (submitted to).

Rossi, Louis F. (1996). "Resurrecting core spreading vortex methods: A new scheme that is both deterministic and convergent". In: *SIAM Journal on Scientific Computing* 17.2, pp. 370–397.

Rossinelli, D. et al. (2010). "{GPU} accelerated simulations of bluff body flows using vortex particle methods". In: *Journal of Computational Physics* 229.9, pp. 3316 –3333.

Sakajo, Takashi (2001). "Numerical computation of a three-dimensional vortex sheet in a swirl flow". In: *Fluid Dynamics Research* 28.6, pp. 423–448.

Sethian, James Albert et al. (1992). "Two-dimensional, viscous, incompressible flow in complex geometries on a massively parallel processor". In: *Journal of Computational Physics* 101.1, pp. 185–206.

Shankar, S. and L. van Dommelen (1996). "A new diffusion procedure for vortex methods". In: *Journal of Computational Physics* 127.1, pp. 88–109.

Singh, S.P. and S. Mittal (2005). "Flow past a cylinder: shear layer instability and drag crisis". In: *International journal for numerical methods in fluids* 47.1, pp. 75–98.

Steggel, Nathan (1998). "A numerical investigation of the flow around rectangular cylinders". PhD thesis. University of Surrey.

Stock, M. (2007). *Summary of Vortex Methods Literature*. URL: http://markjstock.org/research/.

Strain, John (1996). "2D vortex methods and singular quadrature rules". In: *Journal of Computational Physics* 124.1, pp. 131–145.

Swegle, J. W. et al. (1995). "Smoothed Particle Hydrodynamics Stability Analysis". In: *Journal of Computational Physics* 116, pp. 123–134.

Takeda, H. et al. (1994). "Numerical Simulation of Viscous Flow by Smoothed Particle Hydrodynamics". In: *Progress of Theoretical Physics* 92.5, pp. 939–960.

Tofighi, Nima and Mehmet Yildiz (2013). "Numerical simulation of single droplet dynamics in three-phase flows using ISPH". In: *Computers & Mathematics with Applications* 66.4, pp. 525–536.

Wieselsberger, C von (1921). "Neuere Feststellungen über die Gesetze des Flüssigkeits-und Luftwiderstandes". In: *Phys. Z* 22.11, pp. 321–328.

Winckelmans, G.S. and A. Leonard (1993). "Contributions to vortex particle methods for the computation of three-dimensional incompressible unsteady flows". In: *Journal of Computational Physics* 109.2, pp. 247–273.

Yildiz, M. et al. (2009). "SPH with the multiple boundary tangent method". In: *Int. J. Numer. Meth. Engng.* 77.10, pp. 1416–1438. DOI: 10.1002/nme.2458. URL: http://dx.doi.org/10.1002/nme.2458.